POLITECNICO DI TORINO

Corso di Laurea Magistrale

in Ingegneria Energetica e Nucleare

Tesi di Laurea Magistrale

Test and 3D CFD modeling of tubular receivers equipped with turbulence promoters for solar tower applications

Relatori:
Roberto Zanino
Laura Savoldi

Candidato:
Marco Cantone

Anno Accademico 2018/2019

Abstract

The tubular receiver technology is the most used in the central tower systems and the most promising, as it allows reaching very high temperatures of the air coolant, increasing the efficiency of the thermodynamic cycle downstream the solar receiver. However, these receivers suffer the high mechanical stresses caused by the temperature gradient typically established along the tube circumference due to the one-sided heating. The aim of the present work is to investigate the thermal behaviour of four absorber tubes, different for material and for turbulence promoters configuration, both experimentally and numerically. Specific attention will be given to the the role of turbulence promoters installed on the inner surface of the tubes in reducing the peak wall temperature and consequently the thermal gradients between the irradiated and the non-irradiated (back) side of the tube.
The four tubes were manufactured by means of additive manufacturing and were tested at the solar furnace SF60 of the Plataforma Solar de Almería (PSA) in 2017 within a SFERA project, financed by the EU. The use of turbulence promoters has been experimentally demonstrated to reduce the wall temperature with respect to the case of a smooth tube, as expected. Then, Computational Fluid Dynamic (CFD) 3D models have been developed for three of the four samples to compare them with the experimental results: it has been demonstrated the validity of the numerical models and to justify the choice to equip such samples with different kinds of turbulence promoters.
Once the 3D CFD models have been validated, they will become powerful tools for the investigation of the thermal gradients on the tube wall: it will be possible to perform a thermal optimization design to increase the life time of the component against thermal fatigue.

Acknowledgments

Dire grazie non è mai un gesto scontato, non è mai inutile.
Dunque, ci tengo a ringraziare i miei relatori, i professori Laura Savoldi e Roberto Zanino, per avermi dato la possibilità di lavorare ad un progetto di tale spessore e per avermi affidato la responsabilità della campagna sperimentale del progetto SFERA III. Lavorare per due settimane nel centro di ricerca in cui sono nate le tecnologie CSP, non ha prezzo.
Ringrazio di cuore i miei genitori. Grazie per avermi sempre sostenuto e per avermi permesso di portare a termine gli studi universitari. Grazie a Sara e Vincenzo, questo piccolo traguardo è merito di tutta la Famiglia.
Grazie alle persone con cui ho condiviso davvero tutto in questi anni: le sessioni e le vacanze, i bruciori di stomaco e le cene ad oltranza, gli infortuni e le partite di calcetto, le spese per sopravvivere e le mozzarelle, le lacrime per i "10 anni" e il pavimento di Piazza Castello, le partenze e i motorini di Mykonos. In fondo questi anni non sono stati così pesanti e li ricorderemo per il tempo speso insieme.

Index

List of Tables

List of Figures

1. Introduction

The evidence of climate changes, the air pollution and the depletion of fossil fuels are the key elements which have led to great investments in the energy sector to develop high efficient and sustainable technologies.
In the Paris Conference on climate changes (COP21,2015), 195 countries discussed on the strategies to apply to reduce the CO_2 emissions. It was the first universal deal on the climate, legally binding, which defined an action plan to contain the temperature growth to $2°\mathrm{C}$ with respect to the pre-industrial level [1]. What made the COP21 so important was also the inclusion of all the countries of the international community, both the industrialized ones (the most responsible for the emissions) and the developing countries, each with its own perspectives. The deal entered into force on the 4^{th} November 2016, but still no sufficient results have been reached.
Therefore, it is necessary to diversify from non-renewable energy sources and look for alternatives, which must be sustainable and have minimum environmental impact. On this road, the *Concentrated Solar Power* systems (CSP) can play an important role, as that is a technology that is able to produce utility-scale electricity, offering dispatchable power on demand by integrating thermal energy storage or in hybrid configuration.

1.1 Concentrated Solar Power

The Concentrated Solar Power includes systems used to generate electricity by the concentration of the direct solar beam and the use of a conventional power block. The technology was first introduced in large scale in the early 1980's as a result of efforts made to face the oil crisis in 1970's, long before global warming has become an issue. After a couple of decades of low oil prices, the investments and the R&D projects started again at the beginning of the 2000s, promising an important growth for this technology [2]. Today the CSP scenarios proposed by the IEA for the next years are very promising: 20 GW of installed capacity by 2020 and 800 GW by 2050 [3].
Solar radiation available on Earth is approximately 10^4 times the current annual demand of primary energy [4]. However, this is absolutely theoretical as many regions of the world with very good sun conditions are not suitable for solar application (for example for dust or for the absence of water, ecc...), but Figure 1.1 gives an idea of how much powerful could be this source.

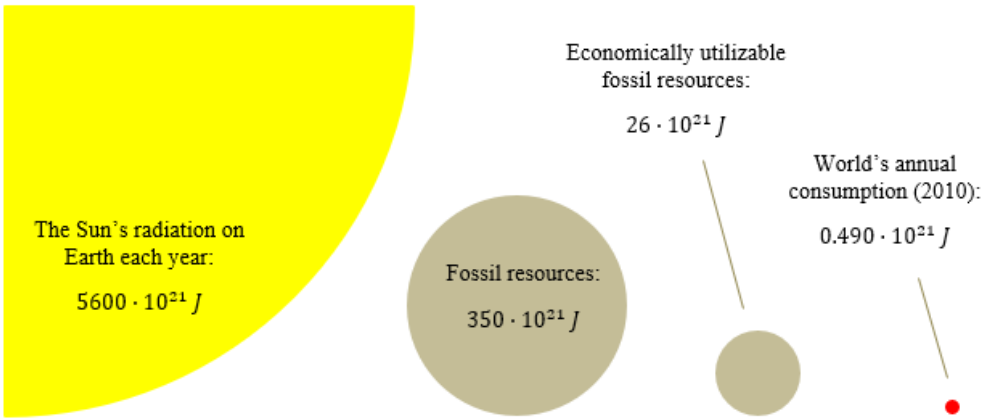

Figure 1.1: Proportions of World's energy resources and demand [4].

The CSP technologies are suitable for large scale electricity production, but they are also capable to provide base-load electricity. This is a very special feature, which makes it unique among the renewable energies: in a market dominated by more weather dependent technologies, as wind energy and photovoltaics, it allows to carve out a space in the current energy market.
CSP systems can also be combined with existing thermal-fired power plants that use coal, natural gas or biofuels and can also be integrated with combined cycle power plants resulting in hybrid power plants which provide higher reliability and affordability. In Figure 1.1 it is shown a scheme of HYSOL configuration for a CSP hybrid power plant using a central tower solar field [5].

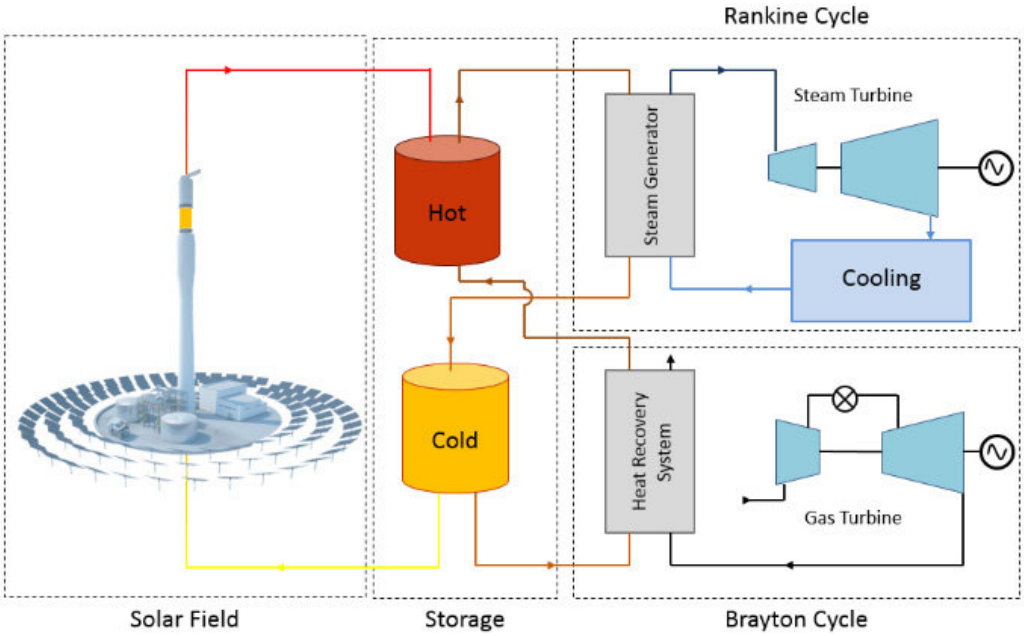

Figure 1.2: HYSOL configuration for a CSP hybrid power plant using a central tower solar field [5].

1.2 Overview of CSP technologies

In CSP power plants, electricity is generated by concentrating solar radiation and they consist of several components, such as solar concentrators, receiver, turbines and electrical generator. Nowadays, four different kinds of CSP power generation plants are found:

- Parabolic Trough systems;
- Solar Tower systems;
- Parabolic Dishes;
- Linear Fresnel systems.

In Figure 1.3, the four configurations are presented, including their installed ratios [6].

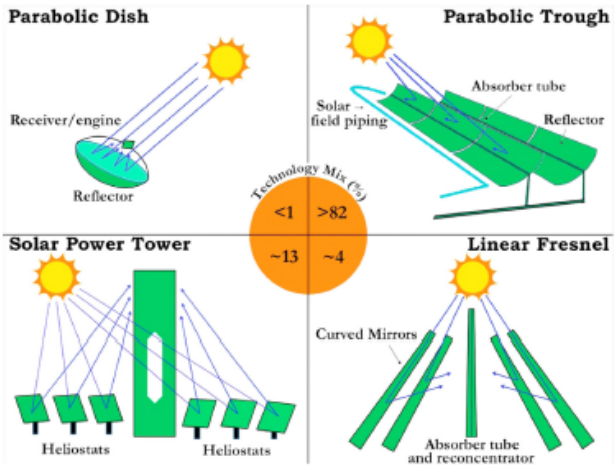

Figure 1.3: Layout of different CSP configurations along with their installed ratios [6].

1.2.1 Parabolic Trough systems

A parabolic trough solar collector is designed to concentrate the sun's rays via parabolic curved solar reflectors onto a heat absorber element (the receiver) located in the optical focal line of the collector. The solar collectors track the sun continuously, through a one-axis tracking system. The key components of a parabolic trough power plant are mirrors, receivers and turbine technology. The receiver consists of a specially coated absorber tube which is embedded in an evacuated glass envelope. The absorbed solar radiation warms up the heat transfer fluid flowing through the absorber tube to almost 400 °C. This is conducted along a heat exchanger in which steam is produced, which then generates power in the turbines. Typically, the working fluid is a diathermic oil because of its high boiling point; otherwise, it can be water, but its pressure has to be raised up and controlled to avoid the evaporation.

1.2.2 Solar Tower systems

Solar Central Tower systems have a single receiver placed on top of a tower surrounded by hundreds or even thousands of mirrors, called heliostats, which follow the apparent motion of the sun in the sky and which re-direct and focus the sunlight onto the receiver. As it is possible to reach very high concentration ratios, higher temperatures and greater thermodynamic cycle efficiency are expected.
The key elements of a solar tower system are the heliostats, provided with a two-axis tracking system, the receiver, the steam generation system and the storage system. According to the selected supply task (base, intermediate and peak load), steam turbine capacity, solar field size and storage size have to be matched in an appropriate way.
The materials for the receiver are generally ceramics or metals that are stable at relatively elevated temperatures. Different receiver technologies exist and various working fluids have been applied during the years: molten salt, air, water/steam, sodium.

The 10 MW Solar One (1981) and Solar Two (1995) were the first central receiver plants to be demonstrated,built in the Mojave Desert of California. Other plants, such as the 11 MW PS10 and 20 MW PS20 in Spain,and the 5 MW Sierra Sun Tower in California were completed in the 2000s [7].

1.2.3 Parabolic Dishes

In solar dish/engine systems, parabolic dishes capture the solar radiation and transfer it to a Stirling engine, which uses external heat sources to expand and contract a fluid, placed in the focus of the parabolic dish. This approach is particularly suited for decentralised electricity generation. Stirling and Brayton cycle engines are currently favored for power conversion.

1.2.4 Liner Fresnel systems

LFR-CSP plants consist of an array of linear mirror strips as reflectors, with receivers, tracking system, process and instrumentation system, steam turbine and generator. The reflectors are the most important components in the system and the mechanism of the reflectors is the same as that of the Fresnel lens. The sun's rays are reflected by the Fresnel lens and focused at one point, generally on to a permanent receiver on a linear tower. In the daytime, the Fresnel reflectors are directed automatically toward the sun, and from there the reflected solar irradiation carries on to the linear tower where a receiver shaped like a long cylinder contains a number of tubes filled with water. With high solar radiation the water evaporates and under pressure runs into the steam turbine that spins a generator that generates electricity [8].
The attraction of the Linear Fresnel option is that the installation cost on a m^2 basis is low, however, other solutions have a higher annual optical performance.

A resume of the key features of all the technologies can be found in Table 1.1. See [6] for more categories.

	Parabolic Trough	**Linear Fresnel**	**Solar Tower**	**Parabolic Dish**
Capacity [MWe]	10-200	10-200	10-150	0.01-0.4
Concentration ratio	25-100	70-80	300-1000	1000-3000
Optical efficiency	Medium	Low	Medium	High
Plant efficiency [%]	14-20	~ 18	23-35	~ 30
Land requirement	Large	Medium	Medium	Small
Operating temp [°C]	290-550	250-390	250-650	800
Annual CF [%]	29-43 (7h TES)	22-24	55 (10 h TES)	25-28
Heat transfer fluid	Synthetic oil, Water/Steam, Air, Molten Salt	Water/Steam	Molten salt, Water/Steam, Air	Air, Hydrogen, Helium
Development status	Most proven	Demonstration	Mature	Demonstration

Table 1.1: Characteristics of CSP technologies [6, 9, 10, 11, 12, 13].

1.3 CSP Global Capacity

The European project "Risk of Energy Availability: Common Corridors for European Supply Security" (REACCESS) evaluated technical, economical and environmental characteristics of present and future energy corridors within Europe and among Europe and the supplying regions of the World, taking into account the different typology of infrastructures and technologies (railways, pipelines, cables, terminals, ships and other carriers, ..), the flows and the distances involved for oil, natural gas, coal, electricity, uranium, biomass and hydrogen. In this project, an analysis of the technical potential of concentrating solar power (CSP) on a global scale was carried out [14].
The analysis was based on the annual direct normal irradiation data (DNI) provided by NASA Surface Meteorology and Solar Energy program (SSE) Version 6.0. The solar resource data was uploaded to a geographic information system and processed together with spatial data on land use, topography, hydrology, geomorphology, infrastructure, protected areas, excluding sites that are not technically feasible for the construction of concentrating solar power plants. In particular, the exclusion criteria included: slope > 2.1%, land cover like permanent or non-permanent water, forests, swamps, agricultural areas, shifting sands including a security margin of 10 km, salt pans, glaciers, settlements, airports, oil or gas fields, mines, quarries, desalination plants, protected areas and restricted areas. Spatial resolution of the data was 1 km^2.
Since CSP uses direct solar radiation, there are just some regions with high DNI (Direct Normal Irradiance) that are suitable for it, the so called world's *Sun Belt*: see Figure 1.4.

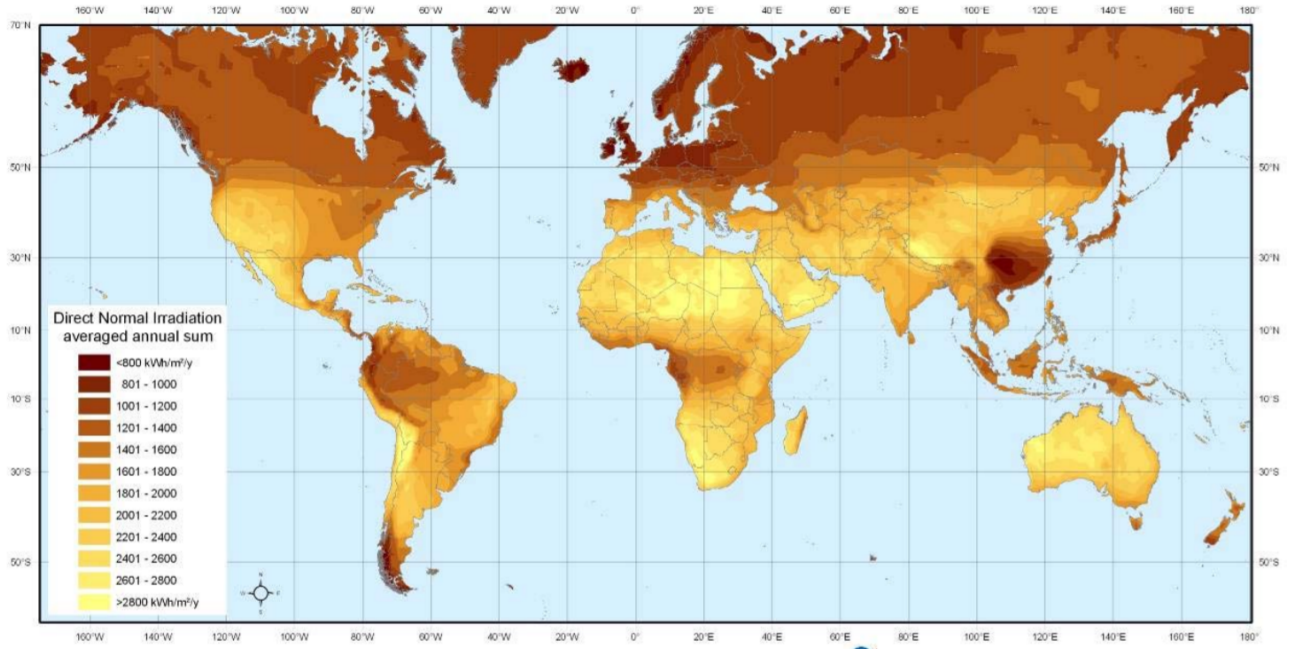

Figure 1.4: World wide annual direct normal irradiation in $kWh/m^2/y$ [14].

The resulting map in terms of excluded sites due to the above mentioned criteria (green colored) is presented in Figure 1.5. Dark areas indicate suitable sites from the point of view of land suitability.

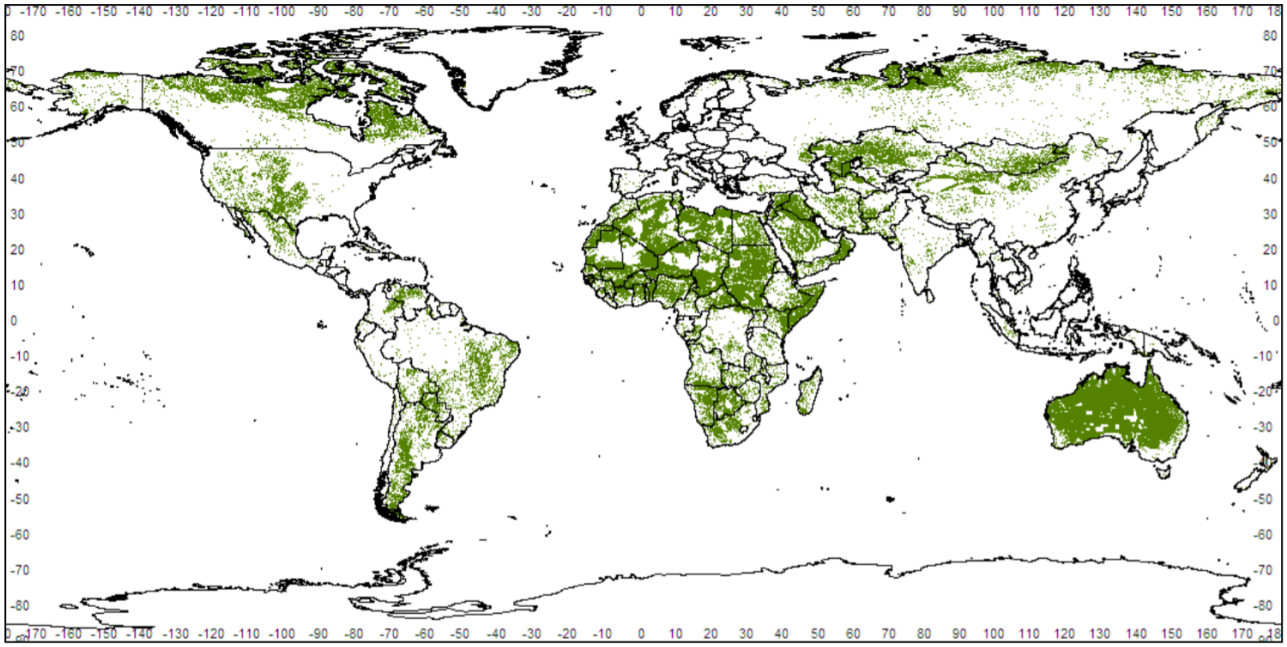

Figure 1.5: World wide exclusion of sites for CSP plant construction [14]

.

From the combination of Figure 1.4 and Figure 1.5, it comes out the global map of annual direct normal irradiance for potential CSP sites (Figure 1.6). The analysis shows that most world regions except Canada, Japan, Russia and South Korea have significant potential areas for CSP at an annual solar irradiance higher than 2000 $kWh/m^2/y$, while Africa, Australia and the Middle East have the largest potential areas, subsequently followed by China and Central and South America [14].

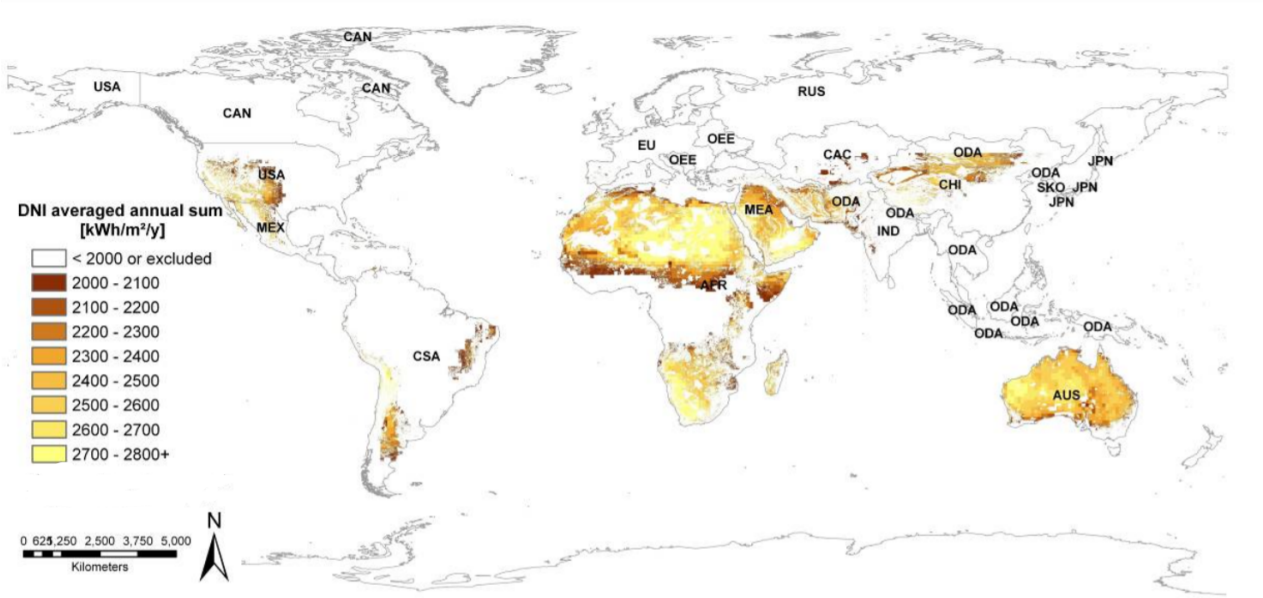

Figure 1.6: Resulting map of the annual sum of DNI for potential global CSP sites [14].

1.4 CSP Global Scenario

An estimated 550 MW of concentrating solar thermal power came out in 2018, increasing cumulative global capacity more than 11% to about 5.5 GW (see Figure 1.7). This annual increase represents the largest gain since 2014, and it occurred despite delays in several projects that had been scheduled to begin operation in 2018. For the third consecutive year, new capacity came online only in emerging markets. This trend is expected to continue because nearly all commercial CSP capacity under construction by the end of 2018 was in emerging countries. China and Morocco led the market in new additions, followed by South Africa and Saudi Arabia.

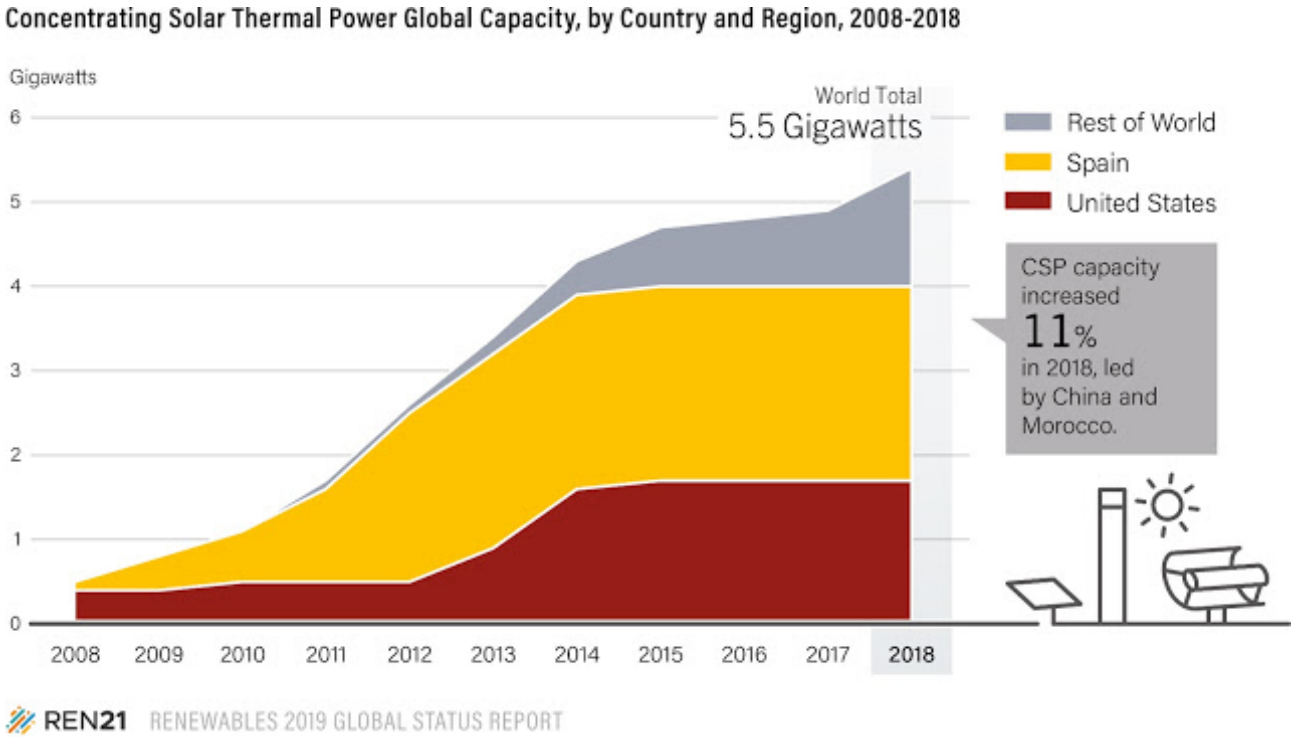

Figure 1.7: Concentrating Solar Thermal Power Global Capacity, by Country, 2008 - 2018 [15].

Spain remained the global leader in existing CSP capacity, with 2.3 GW in operation at the end of 2018, followed by the United States, with just over 1.7 GW. These two countries accounted for around 75% of the global CSP capacity in operation at year's end, but no new capacity has entered commercial operation in Spain since 2013 and in the United States since 2015. Parabolic trough and tower technologies continued to dominate the market. Parabolic trough plants represented around 70% of new capacity additions in 2018, with the balance made up by central tower plants.
All but 3 of the 23 plants under construction by the end of 2018 planned to include thermal energy storage (TES). Storage capacity for CSP facilities with TES is typically reported in "hours" of storage. Almost 17 GWh of thermal energy storage (Figure 1.8), based almost entirely on molten salts, was operational in conjunction with CSP plants across five continents by the end of 2018. The possibility to store heat is central to the operational value of CSP by enabling it to be a dispatchable source of power, increasing its capacity factor, providing a source of grid flexibility and allowing for the integration of higher shares of variable renewable energy in power systems. The total TES capacity in MWh is derived from the sum of the individual storage capacities of each CSP facility with TES operational at the end of 2018.

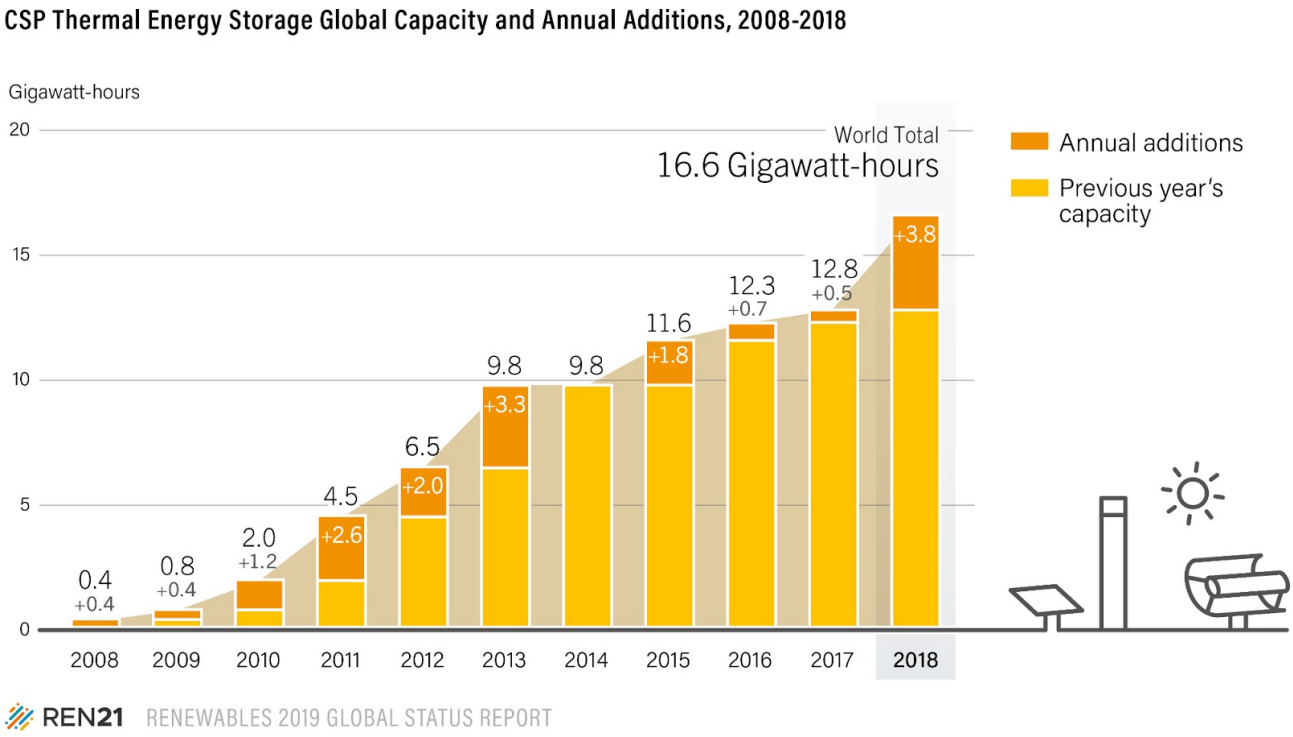

Figure 1.8: CSP Thermal Energy Storage Global Capacity and Annual Additions, 2008-2018 [15].

In the World Energy Outlook 2018 [3], published by the International Energy Agency, three different scenarios for future evolutions have been proposed:

- The *Current Policies Scenario*, which will lead to increasing strains on almost all aspects of energy security and a major additional rise in energy related CO2 emissions;
- The *New Policies Scenario*, which includes policies and targets announced by governments;
- The *Sustainable Development Scenario*, in which accelerated clean energy transitions put the world on track to meet goals related to climate change.

For each of these scenarios, a perspective of world primary energy demand and energy-related CO2 emissions have been outlined. As shown in Figure 1.9, the current policies and the new policies won't allow to reduce the energy-related CO_2 emissions: achieving sustainable development goals will require a complete reversal of the historic relationship between economic growth, energy demand and emissions. The Sustainable Development scenario is the only one where the economic growth (on the left hand side axis) and the CO_2 emission are decoupled. Note that the bubble size and numbers represent total primary energy demand (Gtoe = gigatonnes of oil equivalent; Gt CO_2 = gigatonnes of CO_2).

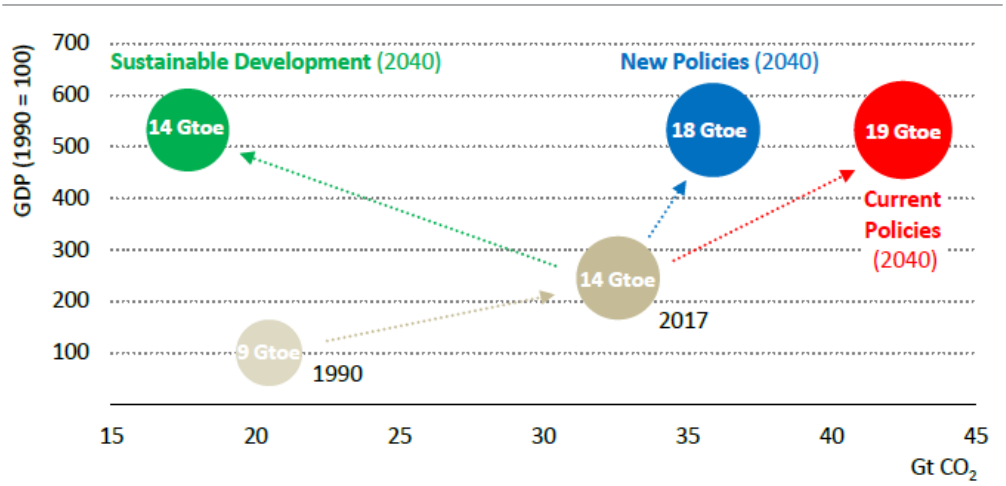

Figure 1.9: CSP Thermal Energy Storage Global Capacity and Annual Additions, 2008-2018 [3].

So, it is clear that renewable energy sources will have a leading role in the very next future: in the trends proposed by the IEA, the CSP growht appears to be promising in all the three scenarios, as shown in Table 1.2. For the first time, the CSP quote has its own detail, while typically it was included into the category "other renewables".

	Power generation capacity [GW]								
	Current Policies			**New Policies**			**Sust. Development**		
year	2025	2030	2040	2025	2030	2040	2025	2030	2040
CSP	11	18	36	13	25	68	20	62	267

Table 1.2: Worldwide CSP power generation capacity in GW through time by scenario [3].

In the New Policies scenario, the most reliable at the moment, the power generation capacity for the CSP plants in the world is expected to raise up to 12 times the current one. In the Sustainable Development scenario, the investments in the concentrated solar power technology would be significant and would lead to an average LCOE drop by more than 30% in nearly all markets to 2030. Furthermore, the LCOE is projected to decline by 10-20% from 2017 to 2040.

1.5 Tubular Receiver Technology

The tubular receiver technology is the most used in the central tower systems: the solar radiation reflected by the heliostat field is concentrated on the external surface of the absorber tube. Here, a working fluid is pumped and heated up, in order to produce electricity in the traditional power block. Solar central receiver systems are designed by matching thermal requirements of thermal processes such as temperature, power level, transient variations, to thermal characteristics of a receiver. Its selection/design is inherently coupled to the selection/design of an optical concentrator. Here, the classification is limited to the basic types, external receiver and cavity receiver, as schematically shown in Figure 1.10.

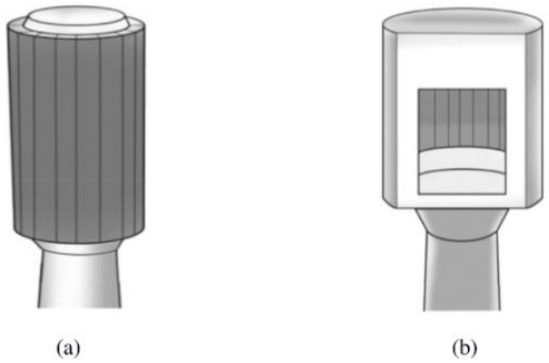

Figure 1.10: Basic receiver types: (a) external receiver and (b) cavity receiver [16, 17].

For an external receiver (Figure 1.10 (a)), radiation absorption, radiative and convective heat losses to the surrounding, and heat transfer to a working fluid or chemical reaction occur at the same surface. Due to the large surface area required for heat transfer, at high temperatures external receivers exhibit high radiative and convective losses. The cavity receiver (Figure 1.10 (b)), consists of a cavity with a small opening (inlet aperture), where the concentrated solar radiation is aimed at. The idea behind the cavity receiver is to minimise the radiation losses: from the radiation entering the inlet aperture, only small amounts are reflected back into the atmosphere through the inlet aperture.
The heat transfer fluid can be different, depending on the plant design features, such as storage, loop configuration and hybridization. At the commercial level, tubular receivers adopt liquid heat transfer fluid, like water and molten salts; however, they can easily work also with pressurized gases, as demonstrated for example in the GAST [18], SOLHYCO [19] and SOLUGAS [20] projects. The choice of pressurized air as heat transfer fluid is widely justified by the following advantages:

- It allows reaching very high temperatures and thus high efficiency of the thermodynamic cycle downstream the receiver;
- It is possible to directly drive a Brayton cycle, which in turn allows adopting a highly efficient solar-driven combined cycle;
- It is for free and abundant;
- It has no risks of phase change.

Nonetheless, there are some disadvantages that are absolutely not negligible: since air has low thermal conductivity and low energy density, it is not the optimal fluid for the thermal storage system, which in principle should be the most powerful feature of the CSP plants.
The drawback of the tubular receivers is that they are limited in the maximum heat flux that they can withstand. This is because these receivers suffer the high mechanical stresses caused by the temperature gradient typically established along the tube circumference due to the one-sided heating. In addition, the thermal fatigue plays a relevant role in the reduction of the absorber tube lifetime, since the tube is exposed to thermal cycles consisting in alternating heating and cooling processes related to daily switching on and off and variations in atmospheric conditions.

1.5.1 GAST project

Tubular receivers have been deeply studied since 1989 within the GAs-cooled Solar Tower project (GAST) project: the aim of the project was the development of a 20 MW_{el} pilot plant in Almería (Spain) to be used also for specific solar-components tests. In the frame of the project, different tubes

materials (metals and ceramic) have been analyzed. Extensive material tests and thermo-mechanical analysis were performed to investigate the effects on the receiver components of this high temperature operating conditions. In particular Low Fatigue Cycle (LFC) and thermal cycling tests on Incoloy 800 H have been performed under an inner pressure of 10 bar and maximum air temperature of about 800°C. In 1985 the metallic tube bundle was replaced with a new ceramic one. These ceramic (SiSiC) tubes had been tested under realistic thermal loading conditions, up to 1000 °C.

1.5.2 SOLHYCO project

The SOLHYCO project [19] started on 1^{st} January 2006 and finished on 30^{th} June 2010 and the setup was mounted in the CESA-1 tower at Plataforma Solar de Almería. The scientific and technological objective of the SOLHYCO project was to develop and test a highly efficient, reliable and economic solar-hybrid cogeneration system based on a 100 kW microturbine, able to operate in parallel on varying contributions of solar power input and fuel. In addition, an innovative solar receiver was developed, based on a "profiled multilayer tube" (PML) receiver concept (Figure 1.11).

Figure 1.11: PML tube sample [19].

The sample included three metallic tube layers: a high temperature alloy at the outer side, copper as intermediate layer and another high temperature alloy layer at the inner side of the tube. The function of the copper with its much higher heat conductivity was to distribute the heat by conduction throughout the circumference. It was demonstrated that this technology enhances the heat transfer from the irradiated tube wall to the gas and allow for reduced temperature differences on the circumference of the tube, thus reducing stress and leading to higher life time. As it is shown in Figure 1.12, the temperature distribution with the PML configuration is more homogeneous and the peak is quite reduced.
Unfortunately, the different thermal expansion of Inconel and Copper led to a progressive degradation of the inter-metallic connection, dramatically reducing the lifetime of the component. The estimated lifetime was calculated by comparison of mechanical stresses and design stresses: mechanical stresses were calculated by a FE analysis of tubes subjected to internal pressure and thermal gradients. It also was shown that the pressurized volumetric solar receivers still worked fine after more than six years, while the considered period of amortization was of 20 years.

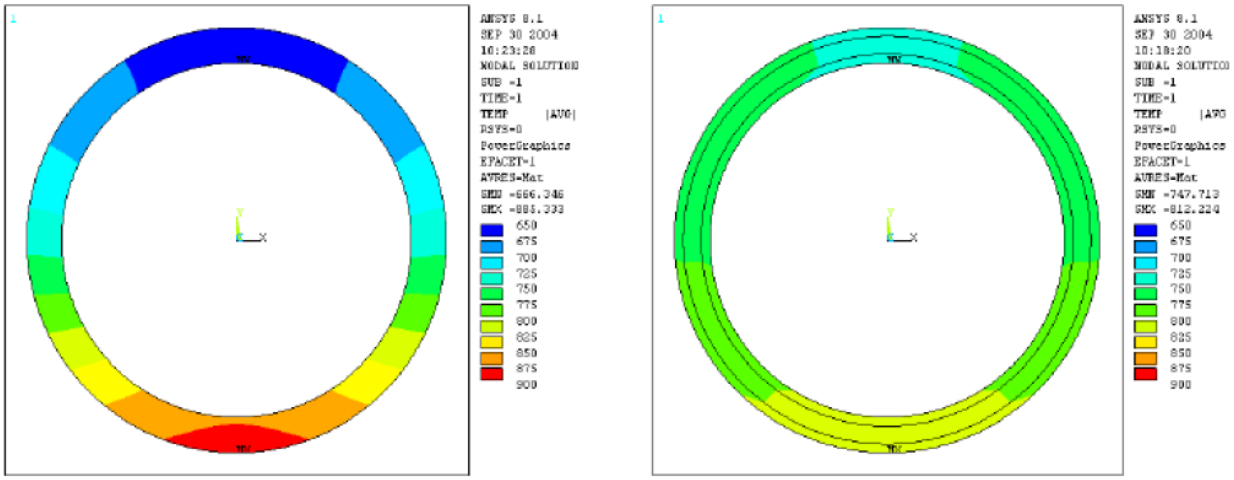

Figure 1.12: Temperature distribution in standard mono-layer Inconel tubes (left) and in PML tubes (right) [19].

The target air temperature of $800°C$ was reached during the experimental campaign, with a $35∠$ inclined cavity receiver, shown in Figure 1.13.

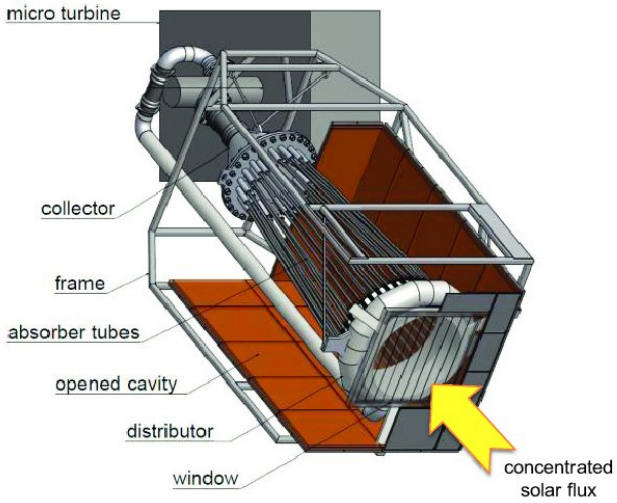

Figure 1.13: Selected design of the solar cavity tubular receiver for the SOLHYCO project [19].

1.5.3 SOLUGAS project

The SOLUGAS project [20] consisted in the demonstration of the first solar hybrid power system with direct heating of a gas turbine's pressurised air at the MW scale. The solar plant was operated during one year under a wide range of conditions, including standard working regime for commercial plants and specific situations in order to obtain accurately its efficiency and characterise the solar receiver, which was made out of 170 nickel alloy tubes (Figure 1.14) and heats pressurized air up to 800°C.

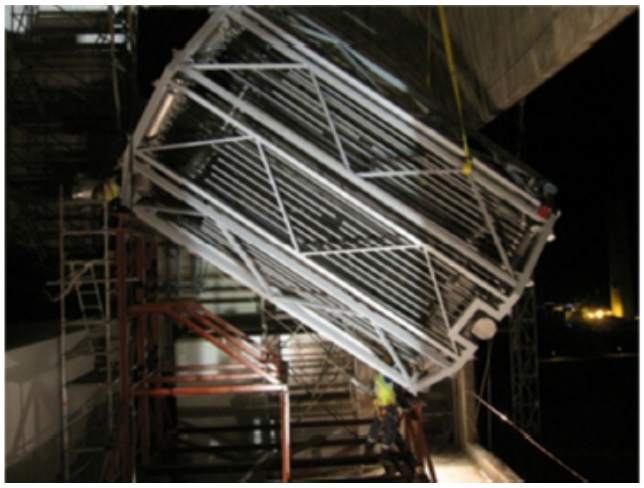

Figure 1.14: SOLUGAS receiver placed on tower [20].

Figure 1.15 shows the main scheme of Solugas system: pressurized air from turbine compressor is heated in the receiver, feeding the combustion chamber of a commercial Mercury 50 gas turbine modified to operate driven by solar energy. Here, the air is heated further with natural gas to reach its nominal working temperature of 1150 °C. The plant consisted of a heliostats field of 69 units, each of them with a reflective area of $121m^2$. The tower bears the receiver in a height of 65 m with an inclination angle of $35\angle$ from the horizontal axis. This allowed minimising thermal convectional losses and increasing optical efficiency.

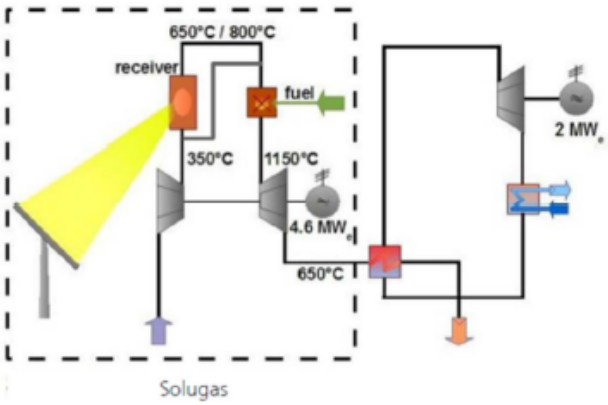

Figure 1.15: Solugas cycle scheme (inside dashed line) [20].

1.6 Aim of the Thesis

Concentrating Solar Power has received significant attention among researchers, companies and global policies for its great potentiality and its features that distinguish it from the other technologies. Spain and USA are worldwide leaders in this sector, but they're not currently planning to invest strongly in new CSP plants, while the developing countries such as China and India are emerging by aggressive investment. The main challenge is to make them more attractive by means of LCOE comparable to the other electricity generation systems.
The aim of the present work is to investigate the thermal behaviour of four absorber tubes, different for material and for turbulence promoters configuration. The idea behind the equipment of turbulence promoters is that tubular receivers suffer dramatically the thermal stresses induced by significant thermal gradients. In fact, since tubular receivers are irradiated just by one side, the thermal fatigue plays

a relevant role in the reduction of the absorber tube lifetime and, so, their reliability.
The four tubes were manufactured by means of additive manufacturing and were tested at the solar furnace SF60 of the Plataforma Solar de Almería (PSA) in 2017 within a SFERA project, financed by the EU. In Chapter 2, a detailed description of the experimental setup is carried out, including all the features and components of the thermo-hydraylic circuit where the samples were tested. Three of these are made of Inconel 718, while the last one is made of AISI 316. The list of the four tubes is the following:

1. Inconel 718 smooth (IS);
2. Inconel 718 equipped with helical ribs (IH);
3. Inconel 718 equipped with annular rings (IA);
4. AISI 316 equipped with helical ribs (AH).

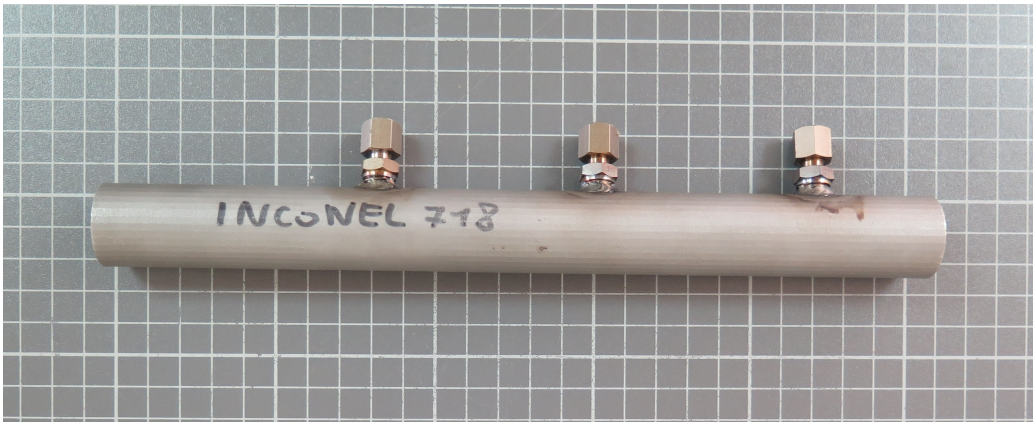

Figure 1.16: Picture of the manufactured Inconel tube.

One of the tubes is shown in Figure 1.16: three thermocouples are inserted from the back side and the sensors are positioned in the irradiated wall thickness. All the details about the geometric parameters will be presented in Chapter 2.
The tubular receivers have been analysed both from the experimental and numerical point of view. The most relevant results from the analysis of the data collected at the PSA are presented in Chapter 3: the focus was mainly concentrated on the steady state tests, being aware that this condition was really difficult to achieve due to the dependence on the weather conditions. For example, clouds or wind can cause instability of both focus point and power source, so that tests can be invalid. In Figure 1.17 both DNI instability due to clouds (left) and high wind velocity (right) examples are shown. In particular, when wind velocities increase, the flat heliostat can face very high stresses, so that it can't be used.
The use of turbulence promoters has been experimentally demonstrated to reduce the wall temperature with respect to the case of a smooth tube, as expected. Then, Computational Fluid Dynamic (CFD) 3D models have been developed for the tested components. Since no surface coating was included in the manufacturing stage, the emissivity is not known a priori: an accurate estimation of the emissivity distribution is obtained by calibrating the model through the experimental results: consequently, the test used for the calibration will not be used in the subsequent validation phase.

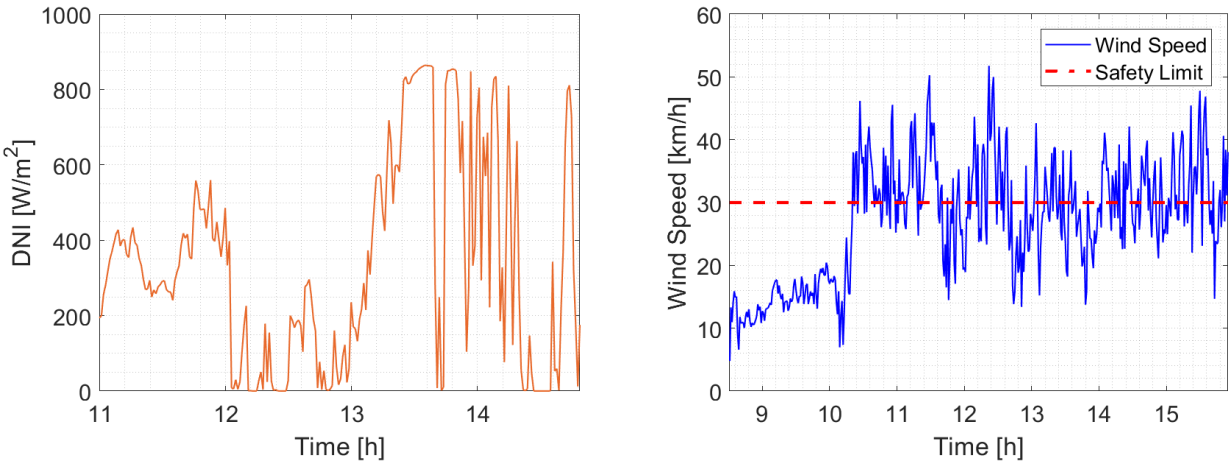

Figure 1.17: Example of day with high DNI instabilities (left) and high wind speed (right).

The rationale behind the CFD analysis is to validate the numerical model on the experimental data, to have a powerful tool for the investigation of the thermal gradients on the tube wall: it will be possible to perform a thermal optimization design to increase the life time of the component against thermal fatigue.
To sum up, the organization of the present work and its logical path is shown in Figure 1.18

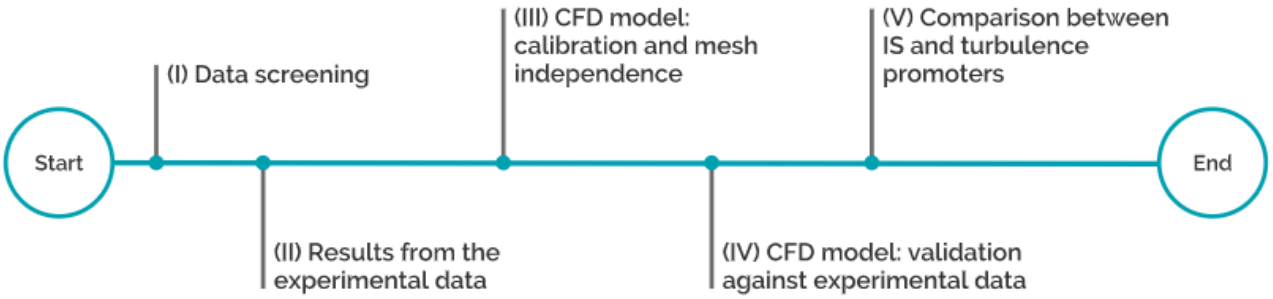

Figure 1.18: Subsequent steps of the present thesis work.

- (I) The Data screening is fundamental to select which are the reliable performed tests that will be used to analyse the thermal behaviour of the four samples at the PSA;
- (II) Once the quasi steady state tests have been collected, a first comparison among the samples will be done in terms of wall temperatures and outlet air temperatures, being sure that the conditions of peak heat flux and mass flow rate are similar;
- (III) A 3D CFD model will be created to simulate the thermal and hydraulic behaviour of the receivers. The robustness of the model will be assured through the grid independence and mesh quality studies. Furthermore, as no absolute values are known, the emissivity and the absorptivity have to be calibrated on STAR-CCM+ to go through in the numerical analysis: a Gaussian distribution of the two parameters will be tailored for three of the four samples;
- (IV) The numerical model will be compared with the experimental results to validate the model. This is a fundamental step because it will make the model useful to go through the thermo-mechanical stresses analysis;

- (V) A detailed comparison between the IS and IH tubes will be proposed in terms of thermo-hydraulic behaviour to demonstrate that the equipment of turbulence promoters allows to smooth the wall temperature peaks and to drop down the thermal gradients along the tube circumference. It means that the stresses on the solar receivers will be softer for the IH tube case study, which means increase of the component lifetime.

2. Experimental Campaign at the PSA

The experimental campaign was financed by the SFERA II project – Transnational Access activities (EU 7th Framework Programme Grant Agreement n 312643) and it lasted for a total duration of two weeks, from September 18^{th} to September 29^{th}, in 2017. In these two weeks, four different tube samples were tested under different solar peak heat flux ranges, monitoring temperatures of both solid and fluid regions. This EU-funded research project (Solar Facilities for the European Research Area) aims to boost scientific collaboration among the leading European research institutions in solar concentrating systems, offering European research and industry access to the best research and test infrastructures and creating a virtual European laboratory.
The project incorporates the following activities:

- Transnational Access: researchers will have access to five state-of-the-art high-flux solar research facilities, unique in Europe and in the world. Access to these facilities will help strengthen the European Research Area by opening installations to European and partner countries' scientists, thereby enhancing cooperation;

- Networking: this includes the organisation of training courses and schools' to create a common training framework, providing regularised, unified training of young researchers in the capabilities and operation of concentrating solar facilities. Communication activities will seek to both strengthen relationships within the consortium, creating a culture of cooperation, and to communication to society in general, academia and especially industry what SFERA is and what services are offered;

- The Joint Research Activities aim to improve the quality and service of the existing infrastructure, extend their services and jointly achieve a common level of high scientific quality.

The purpose of the campaign was to measure the wall thickness temperatures along the length of the absorber tubes to analyse the capability of the turbulence promoters to smooth the peak temperatures on the irradiated side (and so, the temperature gradient along the tube circumference). Furthermore, the experiments will allow comparing two materials that can be potentially adopted for absorber tubes: Inconel and Stainless steel. In particular, the latter could be interesting, since the market price is lower.
Four monolayer tube configurations have been manufactured by means of addictive manufacturing (3D printing). All tubes have the same size, as shown in Table 2.1, while they differ in terms of materials and turbulence promoters. Three of these are made of Inconel 718, while the last one is made of AISI 316 stainless steel. The pitch, width and height of the ribs were designed to maximize the heat transfer coefficient on the base of a preliminary CFD study. The helical-ribbed tube consists of three starts with pitch 22.5 mm and height of the ribs 2 mm. The annular rings have the same shape of the helical ribs, but with a height of 1 mm and a pitch of 6 mm. The fourth configuration consists of a stainless steel tube, equipped with the same helical ribs as the IH tube. The section of a subset of the tested tube is shown in Figure 2.1.

Test ID	Material	Turbulence Promoter	L [mm]	D [mm]	Wall Thickness [mm]
IS		None (Smooth)			
IA	Inconel 718	Annular rings	250	25.4	2.4
IH		Helical ribs			
AH	AISI 316	Helical ribs			

Table 2.1: Geometric parameters of the tubes tested at the PSA.

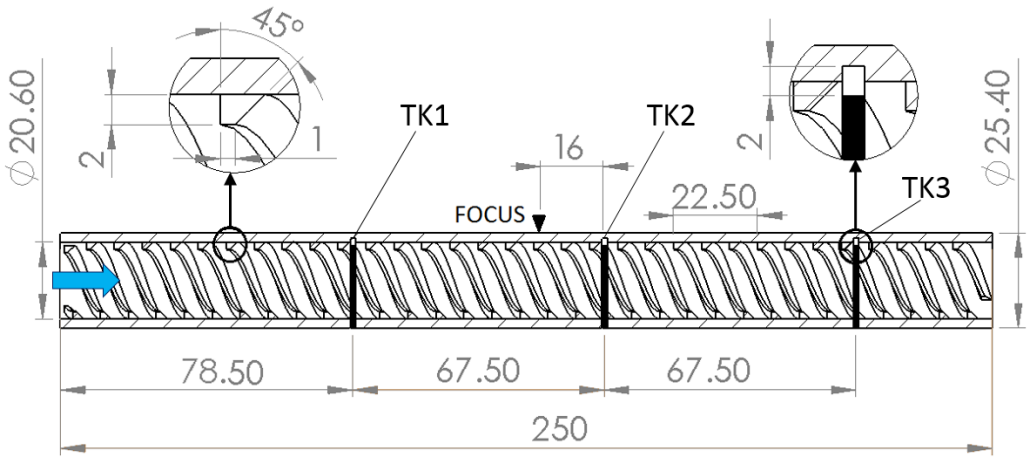

Figure 2.1: Drawing of the helically ribbed tube. All the quotes are expressed in [mm].

Three thermocouples of the K-type were inserted from the back side (the not irradiated one), reaching the wall thickness close to the external irradiated surface. These thermocouples were not welded and were partially inserted by 1 mm inside the inner front wall thanks to pre-formed holes. The sensitive part of these thermocouples extends for 2 mm at the end of the sensor, so that they measure an air/wall average temperature in the proximity of the inner surface of the tube. The nominal position of the focus point in each test is shown in Figure 2.1, being aware that the position of the focus during the tests can change in a non-controlled way, due to small variations of the sample position and of the heliostat orientation.

2.1 Plataforma Solar de Almería

In the province of Almería in southeast Spain, on the edge of Tabernas Desert, lies the Plataforma Solar de Almería (PSA). Owner and operator of the PSA is the spanish research center for energy, environmental studies and technology CIEMAT (Centro de Investigaciones Energéticas, Medioambientales y Tecnológicas). On this over 1 km^2 site, the full force of the Andalusian sun has been exploited since 1980 for the testing and optimisation of a variety of high-temperature solar technologies under nearly practicable conditions. More than 20000 m^2 of mirrors of various shapes in different test facilities concentrate the direct solar radiation to generate high and extremely high temperatures. This facility is the largest test centre in Europe for concentrating high-temperature solar technologies [21].
The research activity at the Plataforma Solar de Almeria has been structured around three R&D Units:

- Solar Concentrating Systems unit, which is devoted to promote and contribute to the development of solar concentrating systems, both for power generation and for industrial processes heat

applications requiring solar concentration, whether for medium/high concentrations or high photon fluxes;

- Solar Desalination unit, which has the objective of new scientific and technological knowledge development in the field of brackish and seawater solar desalination;
- Solar Treatment of Water unit, which explores the photochemical possibolities of solar energy, especially regarding to its potential for water detoxification and disinfection.

Today, the PSA installations are a vehicle for precision testing of the entire range of concentrating solar test applications. The major facilities are:

- 2.7 MW, SSPS-CRS Central Receiver Test Facility;
- 7 MW_{th}, CESA-1 Central Receiver Test Facility;
- 0.6MW_{th} High-Flux Solar Furnace;
- 1.3 MW_{th} ACUREX Parabolic Trough Test Facility with storage and desalination;
- 174 kW_{th} LS-3 Loop Parabolic Trough Test Facility;
- 1.8 MW_{th} DISS Loop;
- 3 x 40 kW_{th} DISTAL I Parabolic Dish Test Facility;
- 3 x 50 kW_{th} DISTAL II Parabolic Dish Test Facility;
- Solar Detoxification Loop;
- Compound Parabolic Concentrator (CPC) Photoreactor;
- SOLFIN (Solar Fine Chemicals Synthesis) Test Facility
- LECE (Laboratory for Energy Testing of Building Components) Facility;

An aerial view of the PSA while the two towers were working is shown in Figure 2.2 below. A more technical map is presented in Figure 2.3, where all the projects are associated to the installation.

Figure 2.2: Aerial view of the Plataforma Solar de Almeria [22].

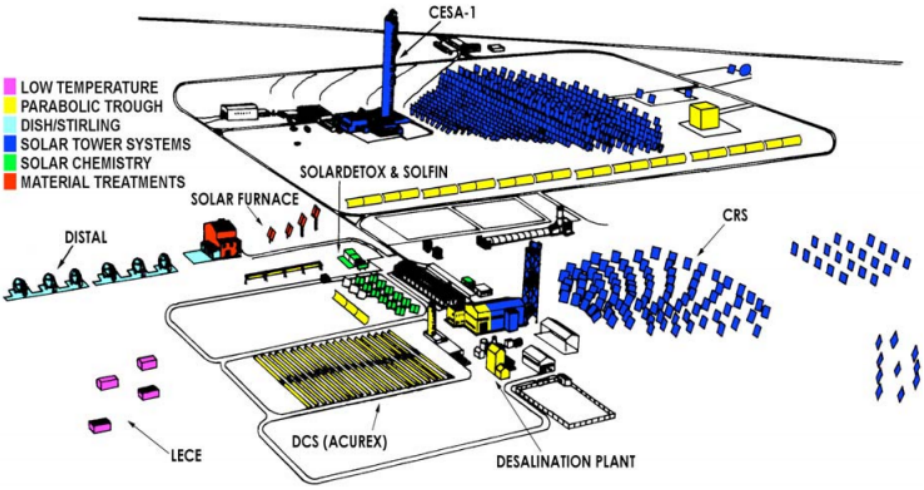

Figure 2.3: PSA Facilities [22].

2.1.1 Solar Furnace

A solar furnace basically consists of a flat solar-tracking heliostat, a parabolic collector mirror, an attenuator or shutter and a test bed located in the concentrator focus (Figure 2.4). The flat collector mirror, or heliostat, reflects the parallel horizontal solar beams on the parabolic dish, which in turn reflects them on the test sample focus. The amount of incident radiation is regulated by the shutter located between the concentrator and the heliostat. A test table movable in three directions (East-West,North-South, up and down) places the test samples in the focus with great precision [23].

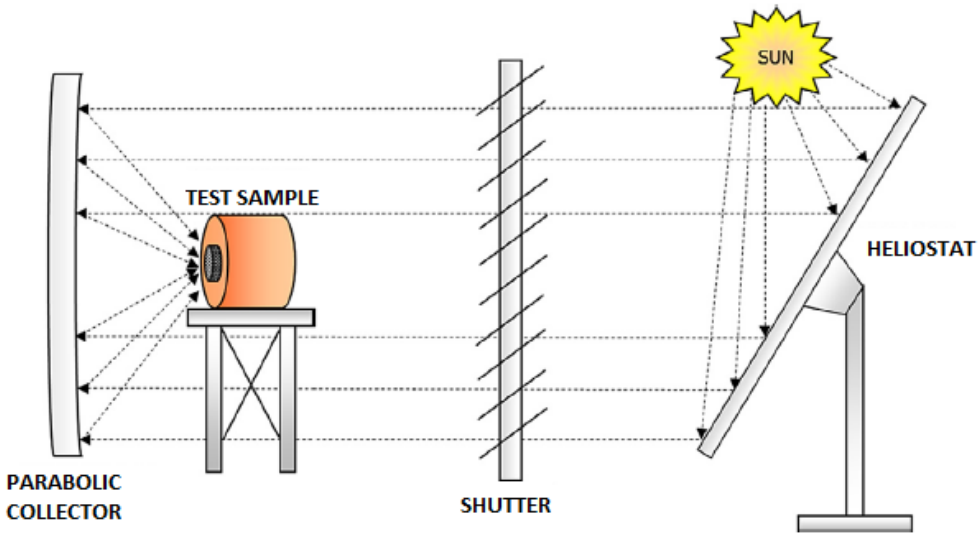

Figure 2.4: PSA Solar Furnace diagram [23].

The first Solar Furnace (SF60) was inaugurated at the PSA in 1991 and currently there are three different solar furnaces:

1. SF60, of 60 kW_{th} and horizontal axis, associated with a 140 m^2 heliostat (Figure 2.5);
2. SF40, of 40 kW_{th} and horizontal axis, associated with a 100 m^2 heliostat (Figure 2.5);
3. SF5, of 5 kW_{th} and vertical axis, associated with a 25 m^2 heliostat.

Figure 2.5: SF40 on the left, SF60 on the right.

The SF60 was used for all the experimental campaign tests: the reflectivity of the heliostat, which is made up of 28 non-concentrating flat facets is about 90%. The parabolic concentrator is the main component of the solar furnace: it is composed of 89 spherical facets with a total surface of 98.5 m^2, 92% reflectivity, focal distance of 7.45 m^2 and rim angle 50.5. When 100% open with Direct Normal Irradiance (DNI) of 1000 W/m^2, peak irradiance at the focus is about 3 MW/m^2, total power is 69 kW and power focal diameter is 26.2 cm [23].

2.2 Experimental setup

The hydraulic circuit was mounted on during the first day of the experimental campaign, thanks to the help of the PSA staff. The instrumentation was calibrated and all the datasheets of the components were analysed. A detailed scheme of the overall system is presented in Figure 2.6.
A 7.5 kW compressor increases the pressure of ambient air up to 10 bar (absolute pressure). The sample tube is connected to the air circuit through a couple of nuts, which are mounted on the sample tube ends, reducing the irradiated length to about 210 mm (from 250 mm). The nuts, as well as the rest of the air circuit, are protected against the concentrated solar radiation by means of an alumina plate placed in front of the test bed. A hole allows to focus the concentrating solar power just on the sample tube (see Figure 2.7). The air heats up, removing heat from the tubes and it is finally cooled down in a water heat exchanger. The circuit is open: the flow rate is measured and it can be regulated through a valve positioned before the sample. The air is now thrown out to the ambient.

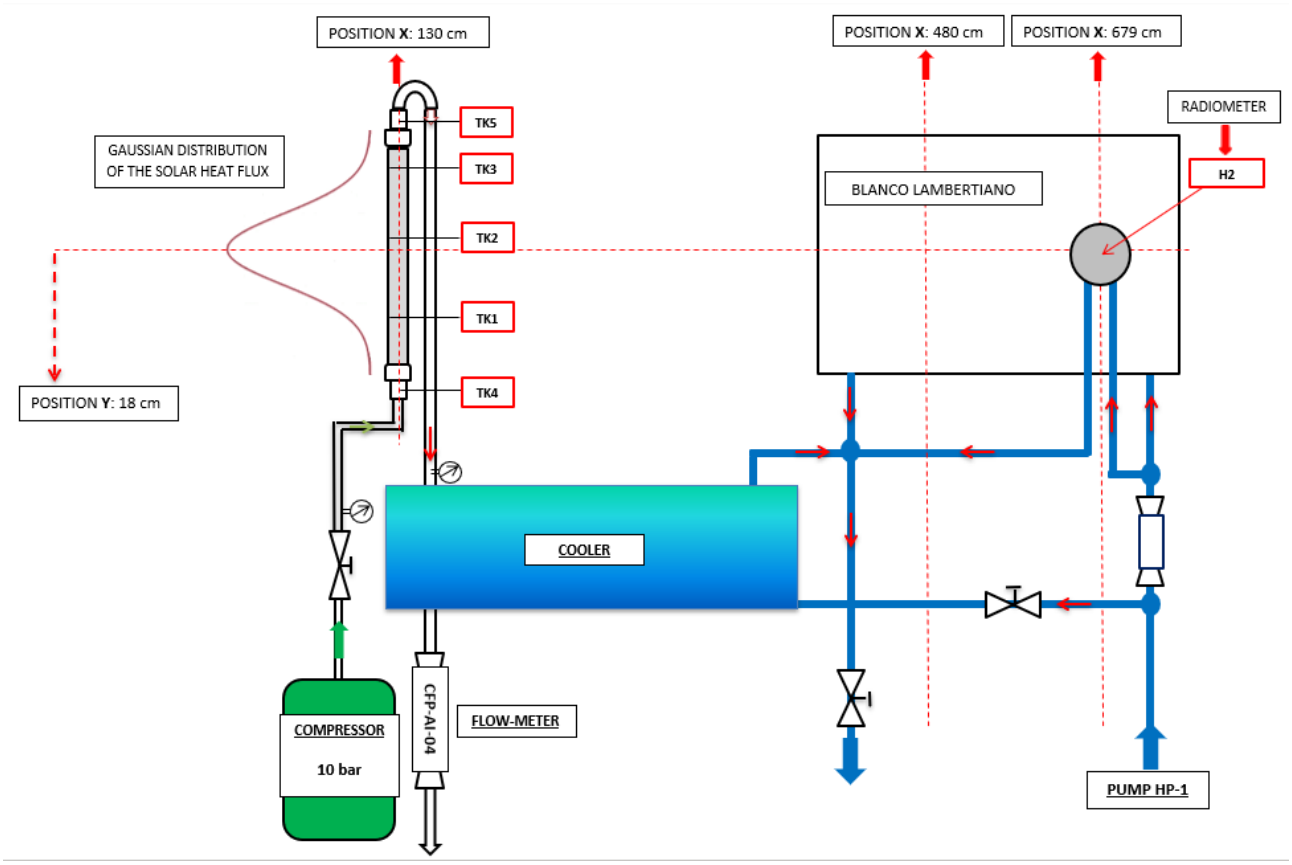

Figure 2.6: Hydraulic circuit at the PSA.

On the right part of the Figure 2.8, it is also included the radiometer for the flux measurement. Since it is irradiated, there is a dedicated cooling circuit to ensure that no high temperature occurs in the instrument, as instead it would affect the its output's precision.

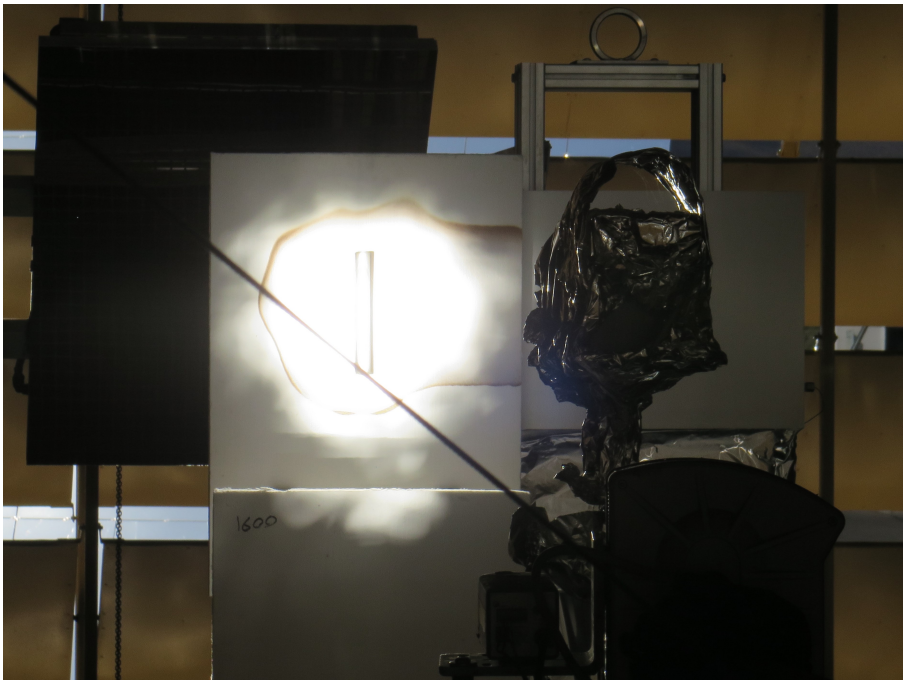

Figure 2.7: Alumina sheet to protect the connections to the sample.

The sample is mounted on a test bed consisting of a three-axis mobile support that allow to move the tube position to the focal area. The amplitude of the peak of the Gaussian distribution has been measured by means of a radiometer (accuracy $\pm$ 3% [24]), which has to be placed in the focus instead of the sample tube. For this reason, the tube samples cannot be tested while the heat flux is being monitored and the incident radiation is measured before/after each test. The overall system during operation is shown in Figure 2.8. Please note that the green point is the laser coming from the parabolic collector, which indicates the center of the focus.

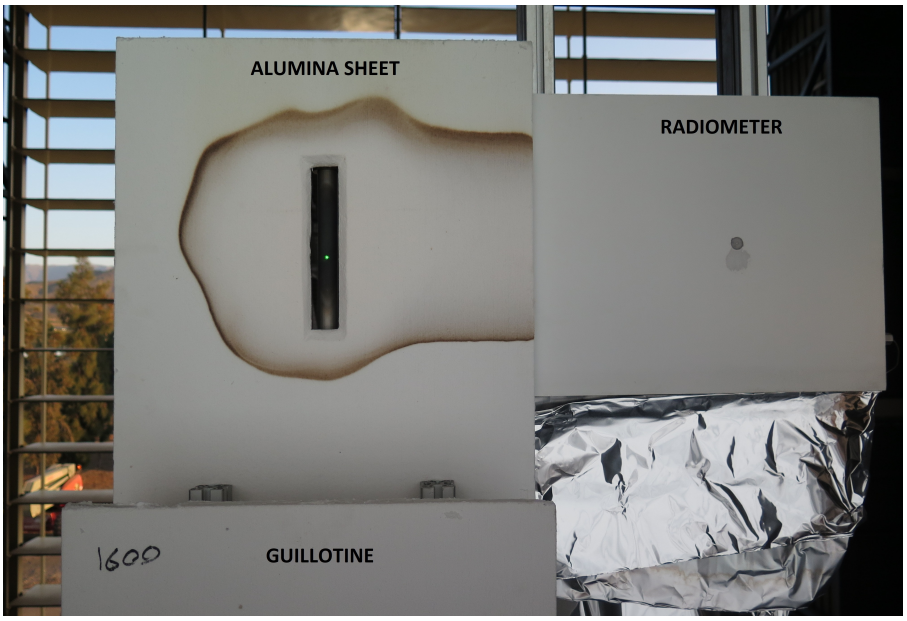

Figure 2.8: Picture of the test bed.

2.3 Measurement Instrumentation

The description of the instrumentation will be crucial for the calculation of the error bars of the experimental data, as then these data will be compared with the CFD results. The most important components of the experimental circuit are:

- Thermocouples of the K-type for the temperatures in $^{\circ}\mathrm{C}$ or K;
- Radiometer for the peak heat flux in kW/m^2;
- Flow meter for the volume flowrate in l/min;
- Pressure switch for the air inlet pressure in bar;
- Pyrheliometer for the instantaneous DNI in W/m^2;
- Infrared camera for the irradiated front face.

2.3.1 Thermocouples

A thermocouple is a simple, robust and cost-effective temperature sensor used in a wide range of temperature measurement processes. Thermocouples consist of two wire legs made from different metals. The wires legs are welded together at one end, creating a junction. This junction is where the temperature is measured. When the junction experiences a change in temperature, a voltage is created

(Figure 2.9). The voltage can then be interpreted using thermocouple reference tables to calculate the temperature.
Thermocouples are available in different combinations of metals or calibrations. The most common are the "Base Metal" thermocouples known as Types J, K, T, E and N. There are also high temperature calibrations - also known as Noble Metal thermocouples - Types R, S, C and GB. The K-type thermocouples are known for low cost and interesting operation temperature range and they're made of Nickel-Chromium / Nickel-Alumel. The thermocouples used in the SFERA II project were all of the K-type, with an error of $\pm 1.5K$.

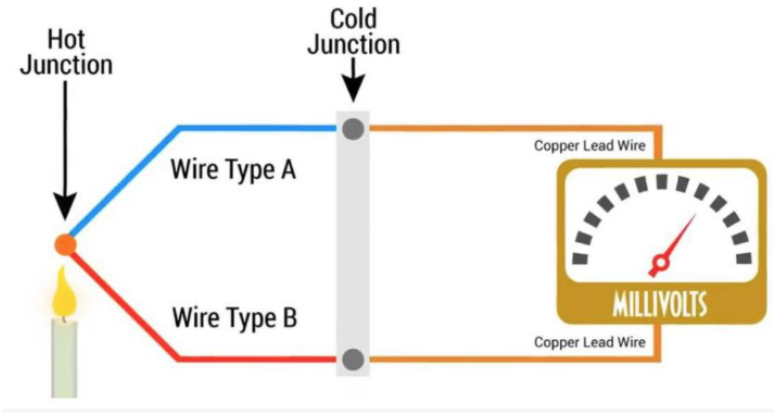

Figure 2.9: Thermocouple measuring circuit [25].

The wires of the thermocouple are protected from the surrounding ambient by a sealed sheath. The sheath is usually made by Inconel or stainless steel. The first works better at high temperature, but the second is usually preferred thanks of its wide chemical compatibility. The measuring junction of the thermocouple can have several configurations, as shown in Figure 2.10.

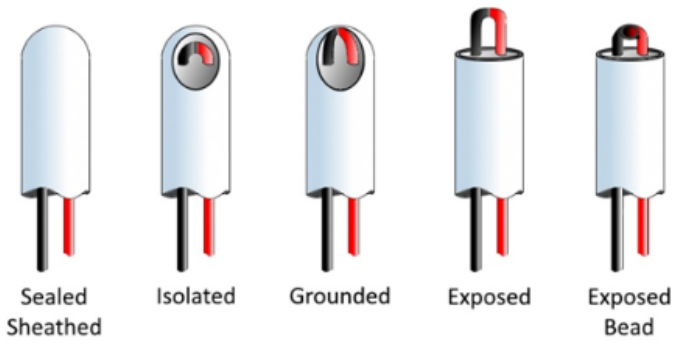

Figure 2.10: Thermocouple protection configurations [26].

The thermocouples useful for the current work are six, as follows:

- TK01 to TK03, positioned in the wall thickness of the irradiated side (Figures 2.1 and 2.11);
- TK04, positioned in the air core flow at the inlet of the sample (Figure 2.11);
- TK05, positioned in the air core flow at the outlet of the sample (Figure 2.11);
- TK06, positioned in the air core flow at the outlet of the circuit (close to the flow meter);

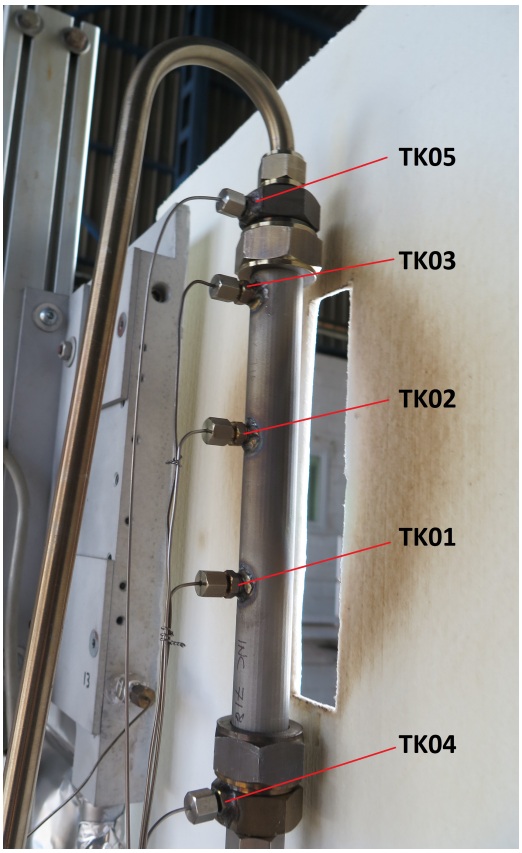

Figure 2.11: Connection of the sample to the hydraulic circuit and installed thermocouples.

Since the thermocouples TK01, TK02 and TK03 were not welded, the precision of their measures can't be assured. By the way, these measures appeared to be in line with the expectations of the preliminary CFD simulations. The thermocouple TK04 is present but not really necessary, as the hydraulic circuit is open: so, the expected air inlet temperature is the ambient one, which is also provided by the PSA control panels. On the other hand, the thermocouple TK05 could be significant in the post processing of the data, as it could give a good estimation of the useful power transferred to the fluid and, therefore, the thermal efficiency of the absorber tubes. Unfortunately, as it will be shown in Section 3.2.4, the TK05 output is very far from the bulk temperature and really close to the inner wall temperature. The reason could be a wrong positioning of the thermocouple during the mounting phase. The thermocouple TK06 is coupled with the flow meter reading: the two will give the mass flow rate, in kg/s or g/s, that could be significant for the simulation results comparison and for first principle balance.

2.3.2 Radiometer

Incident heat flux measurement is essential for the calculation of receiver efficiency, because the integration of the heat flux distribution on the receiver surface determines the radiant power incident on the receiver aperture from the heliostat. There exist two different methods to do it: direct and indirect. The direct method is basically the one used in this experimental campaign, which consists in a water-cooled radiometer. This kind of strategy was used in the PS10 plant in Seville [27]. On the other hand, the indirect method would consist in a capture of the irradiance distribution through a moving lambertian target with a high resolution camera. In order to measure the physical features of the beam, the system must be calibrated. This procedure is based on the correlation with the gray-scale value of any pixel of the image with the corresponding irradiance value measured by a water-cooled radiometer at the same location (see Figure 2.13).

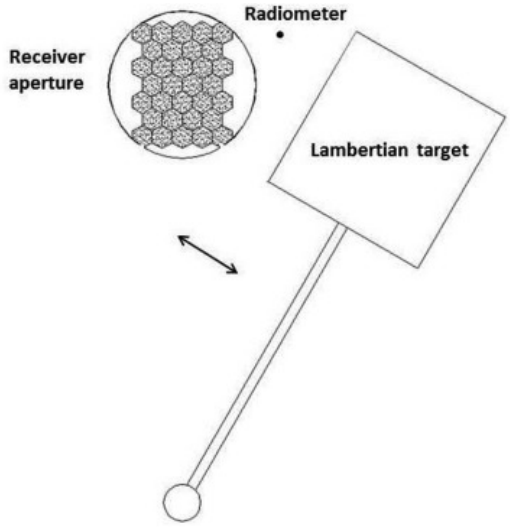

Figure 2.12: Indirect flux measurement system [28].

The radiometer adopted at the SF60 is affected by a systematic error that depends on the spectral absorptivity of the black coating of the sensitive part (made of colloidal graphite) and results in an overestimated heat flux. To take into account this error, the measured heat flux must be multiplied by a correction factor equal to 0.782, which was determined in [24]. The amplitude of the peak of the Gaussian distribution has an accuracy of $\pm$ 3% [24]. The incident heat flux can be then calculated according to the Gaussian distribution defined in [23], which has to be multiplied by the cosine of the local incident angle to take into account the radial curvature of the tube surface.

$$\varphi = \varphi_{peak} \cdot [exp(-\frac{1}{2} \cdot (\frac{x^2}{\sigma_x^2} + \frac{z^2}{\sigma_z^2}))], \tag{2.1}$$

where σ_x and σ_z are the standard deviations provided by [23]: $\sigma_x = \sigma_y = 0.064$. The resulting heat flux distribution given in Equation 4.11 can be visualized in the following figure:

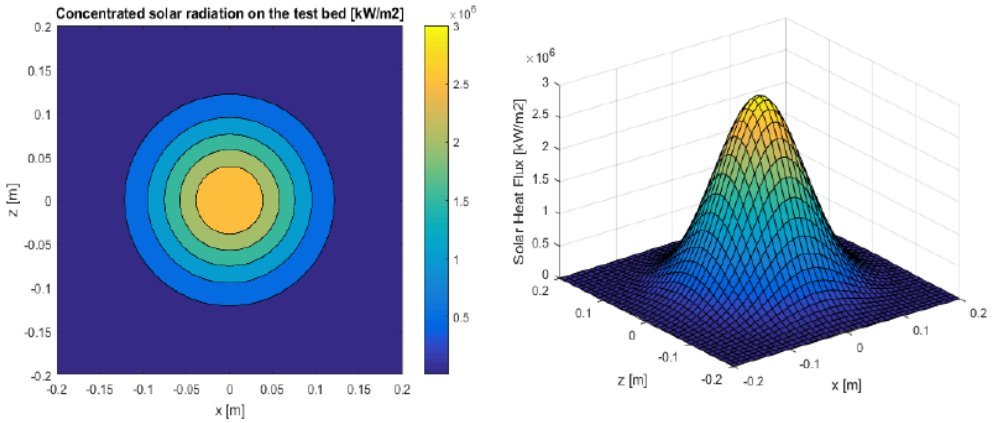

Figure 2.13: Concentrated solar radiation distribution on the focal plane [29].

In addition, two more problems can occur:

1. It misses the exactly peak heat flux applied during the test phase, as the two stages are decoupled;

2. The 25 cm focus on the sample has instantaneously a different position, as the heliostat, tracking the sun, is moved by the wind coming from any possible direction. It is not possible to quantify this error.

2.3.3 Flow meter

The flow rate is one of the variable parameter of the experimental campaign and therefore this value also plays a fundamental role into the data analysis. In fact, a low accuracy and a non suitable calibration of the measuring instrument would lead to more inaccurate experimental results of the thermocouples inside the pipes.
In the SF-60 the air flow rate passing though the sample circuit is measured and controlled by means of a flow meter with an integrated control system. Specifically, the model is the Bronkhorst High-Tech model F-203AV Mass Flow Controllers (MFCs) [30]. F-203AV MFCs are suited for precise control of virtually all conventional process gases. In particular, the MFC consists of a thermal mass flow sensor, a precise control valve and a microprocessor based on a PID controller with signal and field-bus conversion. As a function of a setpoint value, the flow controller swiftly adjusts the desired flow rate. The mass flow, expressed in normal litres per minute or normal cubic metres per hour, is provided as analog signal or digitally via RS232 or field-bus. The flow range, wet materials and orifice size for the control valve are determined depending of the type of gas and the process conditions of the application, therefore this implies that a calibration is needed [30].
The heart of the thermal mass flow meter/controller is the sensor, that consists of a stainless steel capillary tube with resistance thermometer elements [30]. The entire measuring principle, which scheme is shown in Figure 2.14 below, is based on this sensor.
A part of the gas flows through this bypass sensor, and is warmed up heating elements. Consequently the measured temperatures T_1 and T_2 drift apart. The temperature difference is directly proportional to mass flow through the sensor.
In the main channel Bronkhorst High-Tech applies a patented laminar flow element consisting of a stack of stainless steel discs with precisionetched flow channels. Thanks to the perfect flow-split the sensor output is proportional to the total mass flow rate [30]. The accuracy of the flow meter depends on the type of gaseous fluid and on the calibration of the instrument itself, however in its data sheet [30] are described some degrees of accuracy concerning air. The stated accuracy of the sensor [30] is of $\pm$ 0.5% of the actual flow rate reading plus a $\pm$ 0.1% of the full scale (F.S.) of the instrument (1650 l/min in this specific case), additionally another $\pm$ 0.1% of the F.S. error has still to be added due to some uncertainty related to the control stability. In case of quick uses of about 2 minutes the uncertainty related to the F.S. increases up to 2% while the most accurate precision comes with a warm-up time of, at least, 30 minutes.

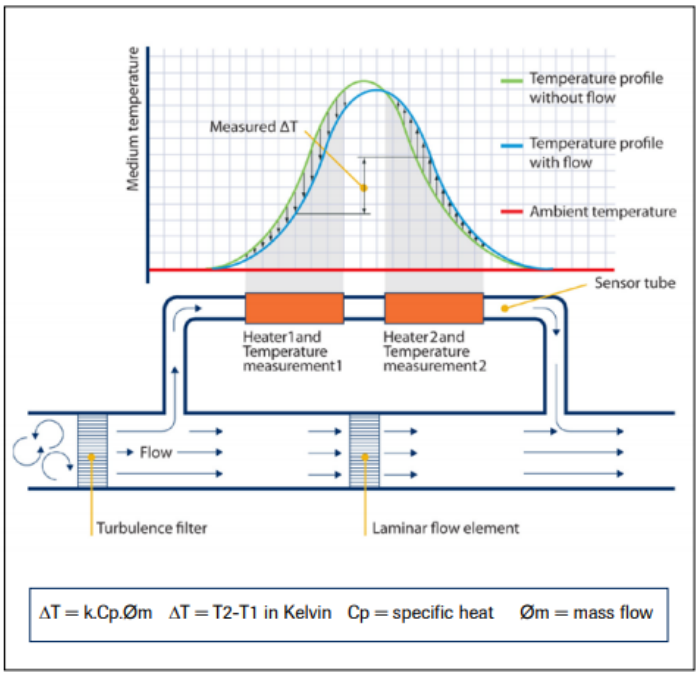

Figure 2.14: Scheme of the Flow meter measuring principle [30].

2.3.4 Pressure switch

A pressure switch is an electro-pneumatic control device that is installed on the air receiver to regulate the output of the air compressor. It is a type of switch that makes or breaks electrical contact when a certain set pressure has been reached at the input. The input is the process pressure connected through impulse line. The process is air, gas, or liquid and would provide ON/OFF switching with adequate current-carrying capacity. Pressure or DP switches are simple electromechanical devices operating on basic principles of deformation/deflection of sensing elements, movement transmitting/multiplying levers/gears, and springs to provide opposing forces.
The working pressure of the overall experimental campaign was about 10 bar, as shown in Figure 2.15: this pressure was checked at each test performance, as it will be an input parameter of the CFD model.

Figure 2.15: Pressure switch at the PSA while measuring the working absolute air pressure.

2.3.5 Pyrheliometer and IR camera

The sun irradiates the top of the earth's atmosphere at an average intensity of 1367 W/m^2. The solar rays travel through our atmosphere and they are absorbed and scattered. This results in different components of solar radiation reaching the earth's surface. The direct component travels in a straight beam from the sun, while a diffuse component comes from all directions, due to the atmospheric scattering process.
A pyrheliometer is an instrument designed specifically to measure the direct beam solar irradiance,also known as DNI: Direct Normal Irradiance. This is achieved by the shape of the collimation tube, with precision apertures, and the detector design. The front aperture is fitted with a quartz window (Figure 2.16) to protect the instrument and to act as a filter that passes solar radiation between 200 nm and 4000 nm in wavelength. A pyrheliometer is used in tracker-mounted operation, to keep the instrument aimed at the sun. The pyrheliometer output was monitored in the control room, as the DNI is the first parameter to check if the operations have to start. In other words, if there is no Sun enough, or if the DNI is too unstable due to passing clouds, the test cannot start. Furthermore, as the error of this instrument cannot affect the accuracy of the experimental results, nor the CFD model, its error is not of interest.

Figure 2.16: Pyrheliometer Hukseflux DR03.

In addition, an infrared camera was positioned in front of the irradiated surface (Figure 2.17). The IR camera is a non-contact device that detects infrared energy (heat) and converts it into an electronic signal, which is then processed to produce a thermal image on a video monitor and perform temperature calculations. Heat sensed by an infrared camera can be very precisely quantified, or measured, allowing you to not only monitor thermal performance, but also identify and evaluate the relative severity of heat-related problems. The system has to be calibrated on the specific component in object: in particular, it was needed the info about the emissivity as a function of the temperature. The IR camera was covered by aluminium to avoid radiation impact and temperature increase which affect the functioning of the camera.

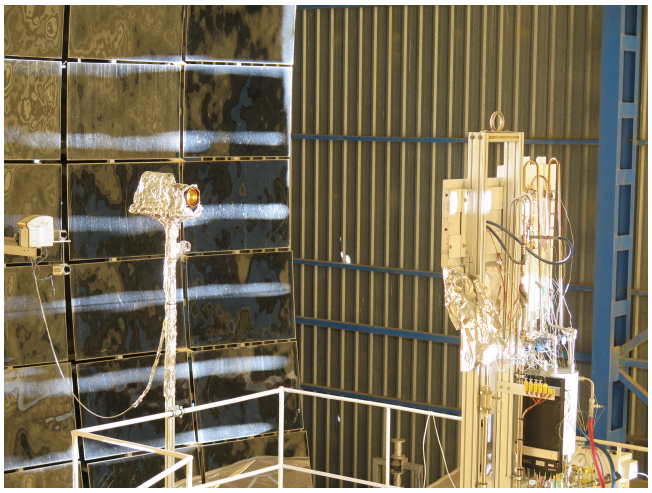

Figure 2.17: IR camera at the PSA.

2.4 Experimental test typologies

During the two experimental campaign weeks two different kind of test were performed:

1. Quasi Steady-State;
2. Transients.

A steady state test aims to obtain an equilibrium between the power applied to the sample, the thermal losses and the useful power to the fluid. Since it is not possible to control the Sun, so the peak heat flux, only "quasi" steady state tests can be performed. In particular, the procedure is the following, as presented in Figure 2.18: first, the shutter is regulated to have the desired peak heat flux; it is measured for a while and, then, the mobile test bed is moved to shine on the receiver. Now, depending on the time scale of the component, the test lasts until the temperatures (that can be monitored instantaneously on the control panel) become almost flat in time. To conclude the test, the radiometer is positioned a second time in the focus to measure the peak heat flux that can be compared with the initial one.

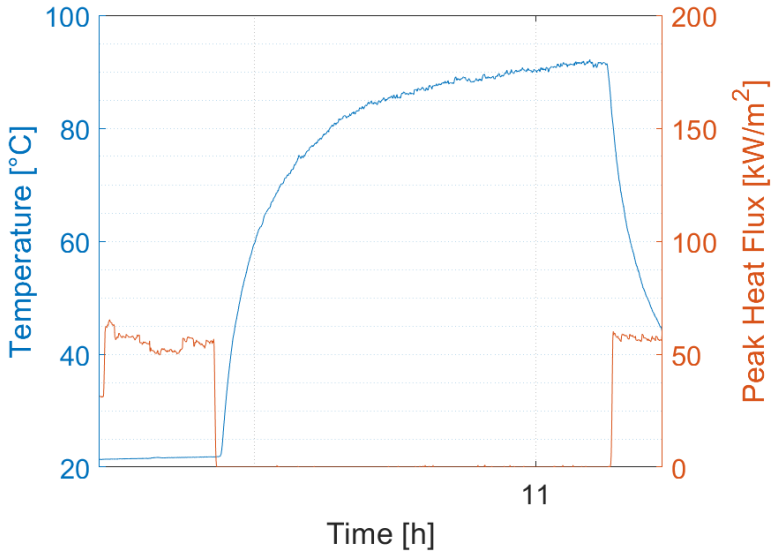

Figure 2.18: Example of quasi steady state test.

Transient cycles were performed to test the solar receivers from the point of view of thermal fatigue and life cycle reduction. These tests were performed on different days, moving the test bed or using the guillotine. In Figure 2.19 it is shown an example of 40 transient tests performed on September the 21^{th}, using the guillotine (60 s ON, 60 s OFF).

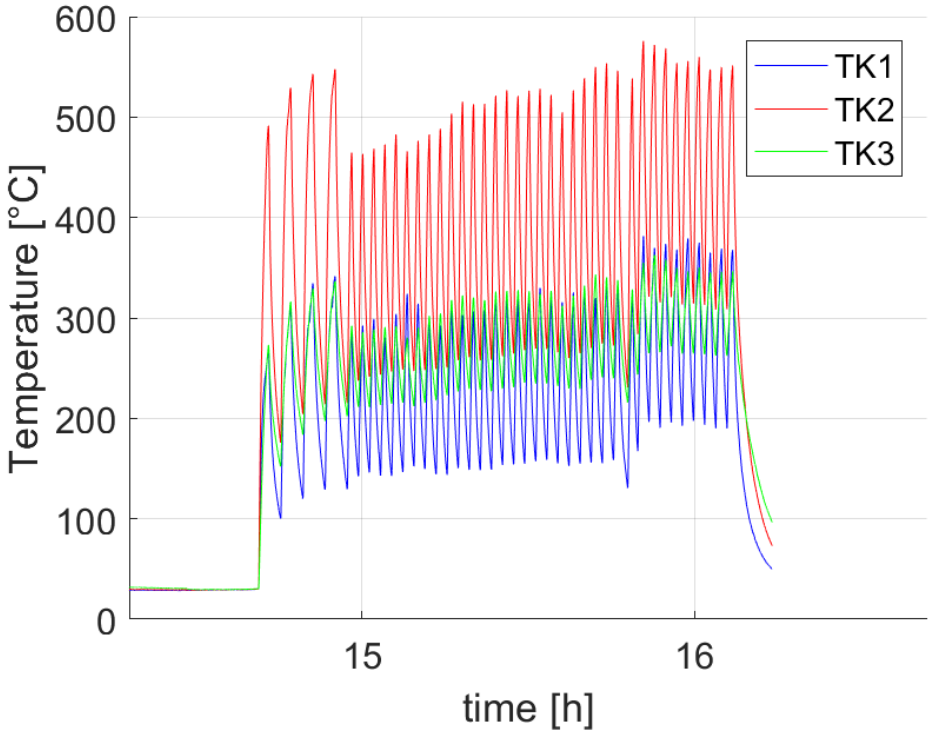

Figure 2.19: Example of transient tests.

3. Data Analysis

The aim of this chapter is to provide all the details of the analysis of the data collected at the PSA, starting from the procedures used to select the good test and to discard the invalid ones. All the days of the experimental campaign will be reviewed and all the results will be presented at the end. The analysis will involve just the "quasi" steady state tests.

3.1 Quasi-Steady State tests

The criteria used to establish the validity of a test as quasi-steady state test are listed below:

- The temperatures (TK01,TK02,TK03,TK05), as well as the peak heat flux must vary at most $\pm 3\%$, as the major instrumentation error;
- The duration of the quasi-steady state interval should be at least of couple of minutes;
- Check on the DNI during the heat flux measurement and test performance, to understand if significant variations occurred (if the DNI increases, the peak heat flux increases too);
- Check on the radiometer output before and after the test performed: it means that the heat flux was measured two times and it was necessary that no significant variations occurred;
- Check on shutter aperture and flow rate, which should be constant during the three phases of the steady state tests;
- Check on the wind velocity, which makes the focus position significantly unstable: the safety limit, provided by the PSA staff, which forced to move back the heliostat in horizontal position (and so to stop every test), was set to 30-35 km/h.

3.1.1 September 19^{th}

On this day, the Inconel Smooth (IS) tube was tested, both aiming at steady state condition and cycling performances, during the working hours. The thermocouples for the air temperatures (inlet and outlet) were not ready on the morning, but just for the three last tests.
The tests performed on this day are presented in Figure 3.1 and 3.2 in form of temperature monitors: then, in Table 3.1 the resume of the valid tests is shown. The values reported in this table have been taken as average on the interval of quasi-steady state; then, the maximum and the minimum of this interval will enter in the error bar.
All the tests from A to D can't be verified through very simple energy balances because of the absence of air temperature data. In addition, test B was invalid because of the shutter aperture, which changed between the radiometer measurement and the test phase. Furthermore, tests C and D were performed

consequently, changing the heat flux level, measuring it just for the C one. The very same occurred with tests F and G and, in addition, as the Sun was going down, the heat flux was quite unstable.

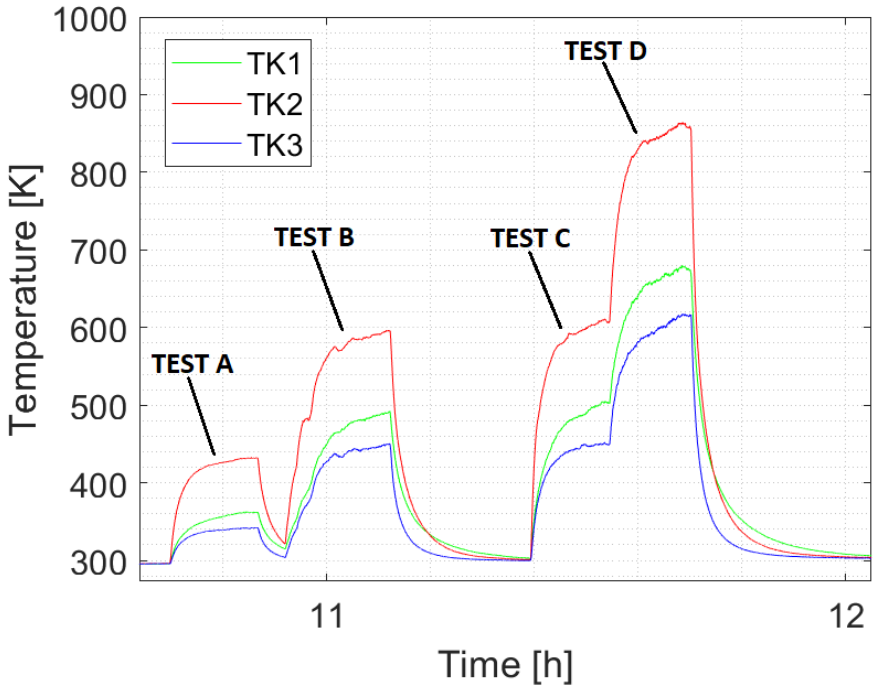

Figure 3.1: Temperatures measured on test day 19/09/17 (I).

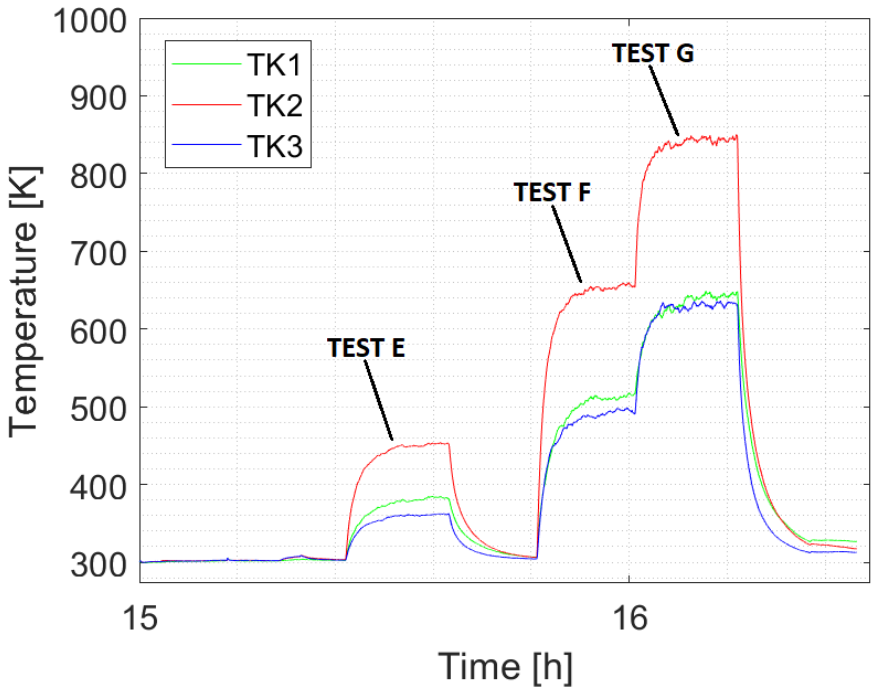

Figure 3.2: Temperatures measured on test day 19/09/17 (II).

Test	Sample	Heat Flux [kW/mq]	TK1 [K]	TK2 [K]	TK3 [K]	V [l/min]	TEST ID
C	IS	180.9	492.9	600.6	447.1	40	IS1
E	IS	63.5	380.9	450.6	360.8	25	IS2

Table 3.1: Resume of the valid tests performed on day 19/09/2017.

3.1.2 September 20^{th}

On this day, the Inconel 718 equipped with helical ribs (IH) was tested. The three reference levels of peak flux are 55, 180 and 280, as then the aim is to compare the different technologies in the same conditions (thermal driver and flow rate). By the way, on this day it was reached the highest flux level of the experimental campaign: some tests were performed at about 380 kW/m^2, as shown in Table 3.2.

Sample	Heat Flux [kW/mq]	TK1 [K]	TK2 [K]	TK3 [K]	V [l/min]	TEST ID
IH	390.1	734.6	905.9	674.6	40.5	IH1
IH	371.8	673.2	894.2	620.9	40.5	IH2

Table 3.2: Resume of the valid tests performed on day 20/09/2017.

3.1.3 September 21^{th}

On this day, the AISI 316 tube equipped with helical ribs (AH) was tested. The day was very good, as the DNI was stable during the tests (no clouds, no wind). The performed tests are presented in Figure 3.3 and the resume of the valid tests is shown in Table 3.3. Since in the afternoon transient tests were carried out, just three tests have been evaluated and they matched all the criteria chosen.

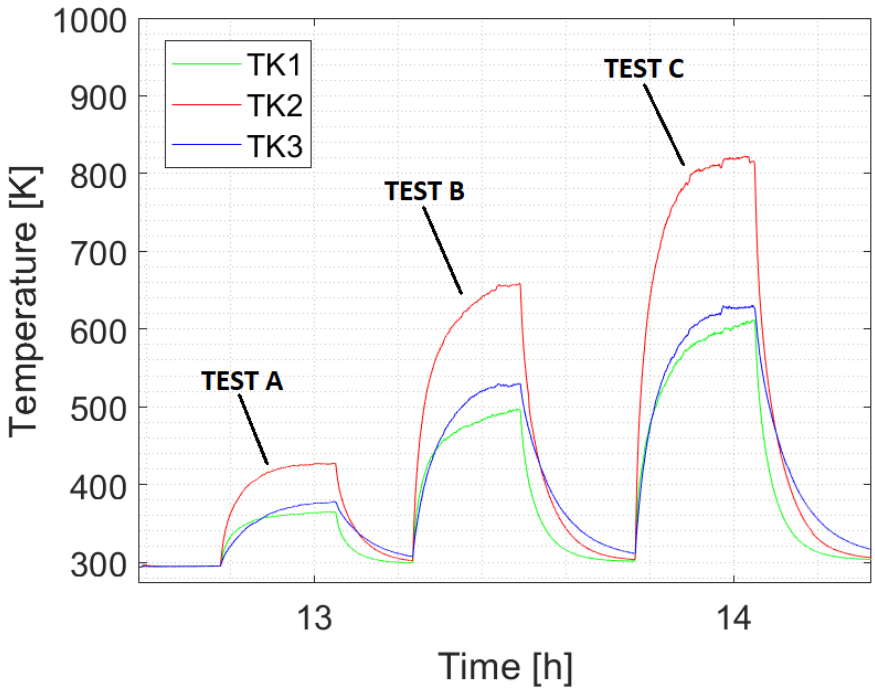

Figure 3.3: Temperatures measured on test day 21/09/17.

Test	Sample	Heat Flux [kW/mq]	TK1 [K]	TK2 [K]	TK3 [K]	V [l/min]	TEST ID
A	AH	57.2	361.3	421.9	369.7	39.5	AH1
B	AH	170.8	493.7	656.3	527.9	39.5	AH2
C	AH	277.7	603.9	820.0	627.4	41.8	AH3

Table 3.3: Resume of the valid tests performed on day 21/09/2017.

3.1.4 September 22th

On this day, the Inconel 718 tube equipped with annular rings (IA) was tested. All the cycles performed during this day were extremely corrupted by the passing clouds and by the strong wind that continuously moved the focus point. The test C was interrupted by passing clouds, which make this test completely invalid. The only useful data collected during this day are the test A and B.
The performed tests are presented in Figure 3.4 and the resume of the valid tests is shown in Table 3.4.

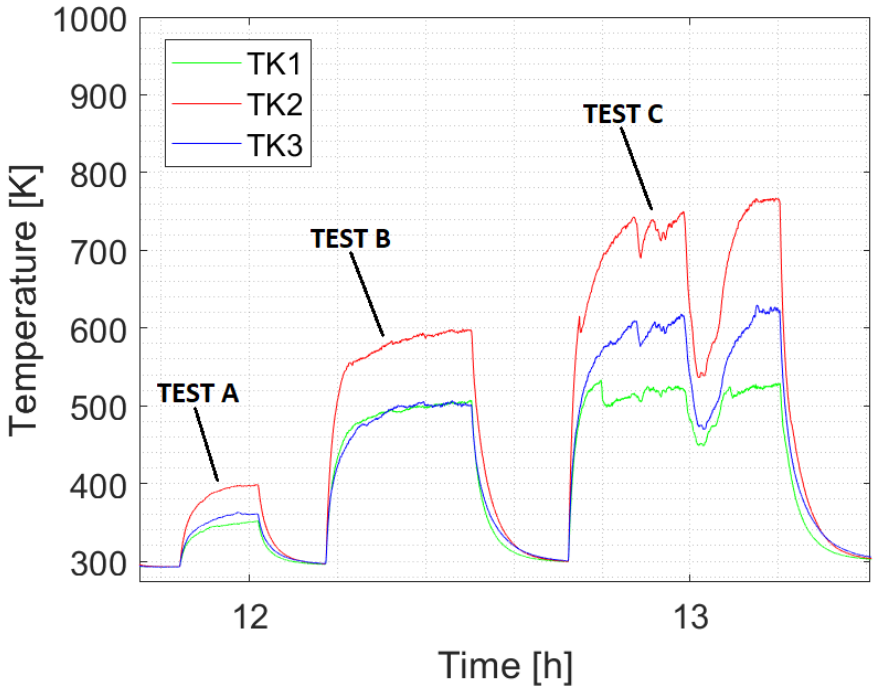

Figure 3.4: Temperatures measured on test day 22/09/17.

Test	Sample	Heat Flux [kW/mq]	TK1 [K]	TK2 [K]	TK3 [K]	V [l/min]	TEST ID
A	IA	50.4	346.3	397.6	360.2	39.5	IA1
B	IA	190.1	502.9	594.9	501.8	39.5	IA2

Table 3.4: Resume of the valid tests performed on day 22/09/2017.

3.1.5 September 25^{th}

On this day, the test bed was modified and the three Inconel tubes were mounted in parallel and tested one after the other in steady-state conditions. See Figure 3.5 and Figure 3.6.
The tests were performed following the schedule below:

1. Radiometer in the focal point;
2. Smooth tube in the focal point;
3. Radiometer in the focal point;
4. IA tube in the focal point;
5. Radiometer in the focal point;
6. IH tube in the focal point;
7. Radiometer in the focal point to check the heat flux.

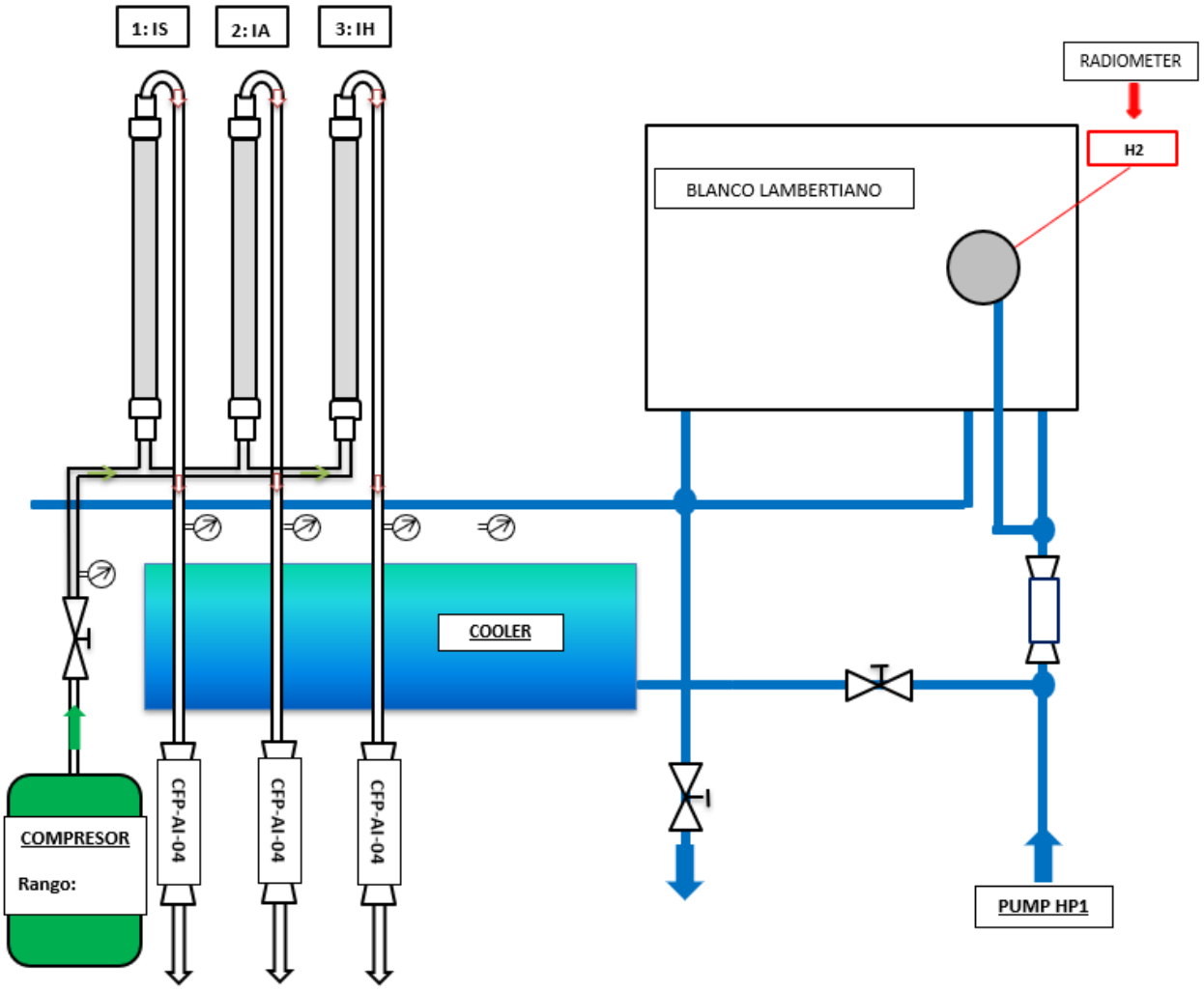

Figure 3.5: Hydraulic circuit at the PSA with the three Inconel tubes mounted in parallel.

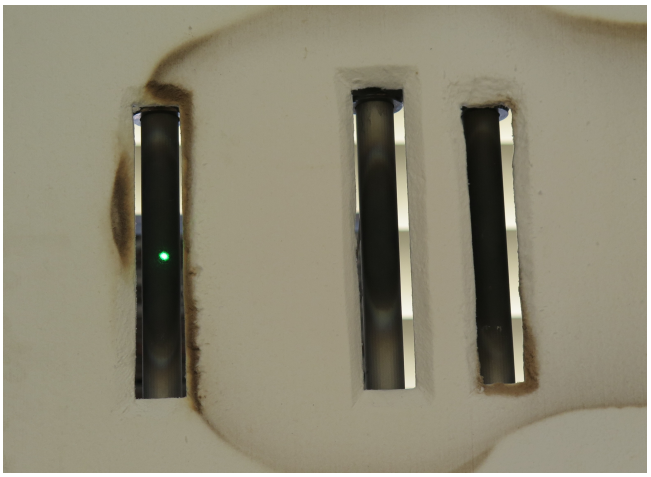

Figure 3.6: Photo of the three Inconel tubes mounted in parallel.

The test day started at 10 am because of the new installation and all the tests were well performed, thanks to a very stable DNI. The three peak flux levels of interest were about 55, 180 and 280 kW/m^2. The valid tests are presented in Table 3.5.

Sample	Heat Flux [kW/mq]	TK1 [K]	TK2 [K]	TK3 [K]	V [l/min]	TEST ID
IS	54.7	358.4	464.7	353.2	40.5	IS3
	177.7	489.3	683.3	482.8	40.5	IS4
	266.7	600.6	797.3	563.4	41.5	IS5
IA	54.6	379.8	446.7	376.1	39.5	IA3
	177.8	490.3	625.5	512.9	40.5	IA4
	279.3	535.8	754.7	614.4	40.5	IA5
IH	54.6	350.5	418.2	378.1	39.5	IH3
	182.9	448.0	622.0	538.4	39.5	IH4
	279.3	547.5	765.9	629.9	41.5	IH5

Table 3.5: Resume of the valid tests performed on day 25/09/2017.

3.1.6 September 26^{th} to September 29^{th}

On these days, no useful data for quasi-steady state tests were collected:

- Day 26/09: the DNI was unstable for almost all the day; when the conditions were favorable, transient tests were performed.
- Day 27/09: no radiation at all;
- Day 28/09: no radiation at all;
- Day 29/09: typically, on the last day, just couple of hours can be used to test the sample, as then it is necessary to disassemble the circuit. During the few good hours of Sun, no good tests were found.

3.1.7 Resume of the collected data

The tests where almost steady-state conditions were reached are summarized in the Table 3.6, together with the respective values of measured peak heat flux and flow rate, which are the controlled parameters of the experiments.

Sample	Heat Flux [kW/mq]	TK1 [K]	TK2 [K]	TK3 [K]	V [l/min]	TEST ID
IS	180.9	492.9	600.6	447.1	40	IS1
	63.5	380.9	450.6	360.8	25	IS2
	54.7	358.4	464.7	353.2	40.5	IS3
	177.7	489.3	683.3	482.8	40.5	IS4
	266.7	600.6	797.3	563.4	41.5	IS5
IA	50.4	346.3	397.6	360.2	39.5	IA1
	190.1	502.9	594.9	501.8	39.5	IA2
	54.6	379.8	446.7	376.1	39.5	IA3
	177.8	490.3	625.5	512.9	40.5	IA4
	279.3	535.8	754.7	614.4	40.5	IA5
IH	390.1	734.6	905.9	674.6	40.5	IH1
	371.8	673.2	894.2	620.9	40.5	IH2
	54.6	350.5	418.2	378.1	39.5	IH3
	182.9	448.0	622.0	538.4	39.5	IH4
	279.3	547.5	765.9	629.9	41.5	IH5
AH	57.2	361.3	421.9	369.7	39.5	AH1
	170.8	493.7	656.3	527.9	39.5	AH2
	277.7	603.9	820.0	627.4	41.8	AH3

Table 3.6: Resume of all the quasi-steady state valid tests.

3.2 Results

This section deals with the analysis of the quasi steady-state tests only. The most relevant results coming from the post-processing of the selected data (Table 3.6) are presented in the next subsections.

3.2.1 Inner Wall Temperatures

The focus of the parabolic collector is closer to the thermocouple TK2, as shown in Figure 2.1: it is expected to find there the maximum temperature among the three different positions along the tube axis. So, the very first necessary comparison between the four tubes can be done in terms of TK2: as expected, the smooth and the AISI 316 receivers perform the highest temperatures, one due to the absence of any turbulence promoters and the other one because of the different material. In Figures 3.7 and 3.8, the TK2 are shown for each typology of receiver and for each peak flux level (55-180-280 kW/m^2). The error bar takes into account the following uncertainties:

- The accuracy of the thermocouples: $\pm 1.5K$;
- The quasi steady-state tests were performed keeping the heat flux and the mass flow rate as constant as possible. A perfect steady-state test is not really possible, because of the intrinsically unsteady behavior of the incident heat flux, specially in the case of passing clouds and/or in the

presence of wind that moves the position of the focus point: so, each test is composed of a mean value of the temperature/flow rate/heat flux and their maximum and minimum during the quasi-steady state test time.

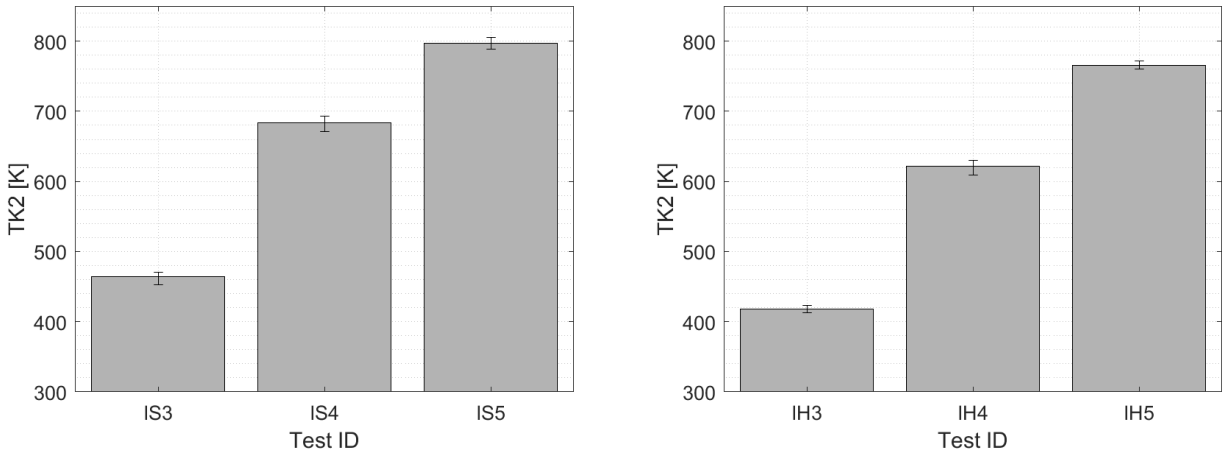

Figure 3.7: Measured peak temperature (TK2) for the IS tube (left) and IH tube (right).

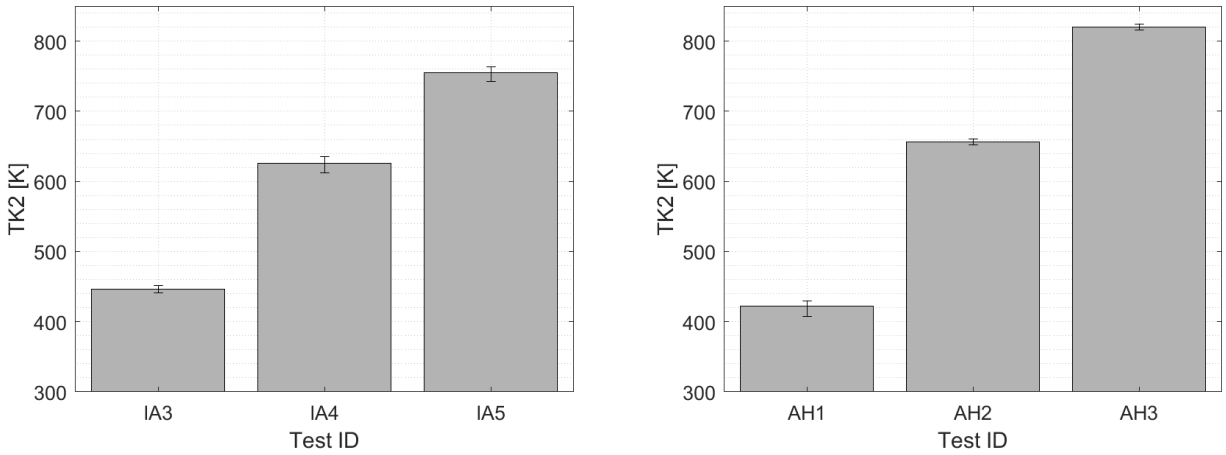

Figure 3.8: Measured peak temperature (TK2) for the IA tube (left) and AH tube (right).

In Figure 3.9, the measured peak temperature (TK2) for all the tube configurations are shown in the same plot, to better visualize the comparison between each other. As expected, as the heat flux level increases, it appears to be more clear the experimental evidence about the wall temperatures: for the IH and IA tubes, the peaks are quite smoothed. The news, maybe, is the thermal behaviour of the AH sample which appears to be comparable with the IS one: despite of the equipment of turbulence promoters, the worse material makes the result very similar.

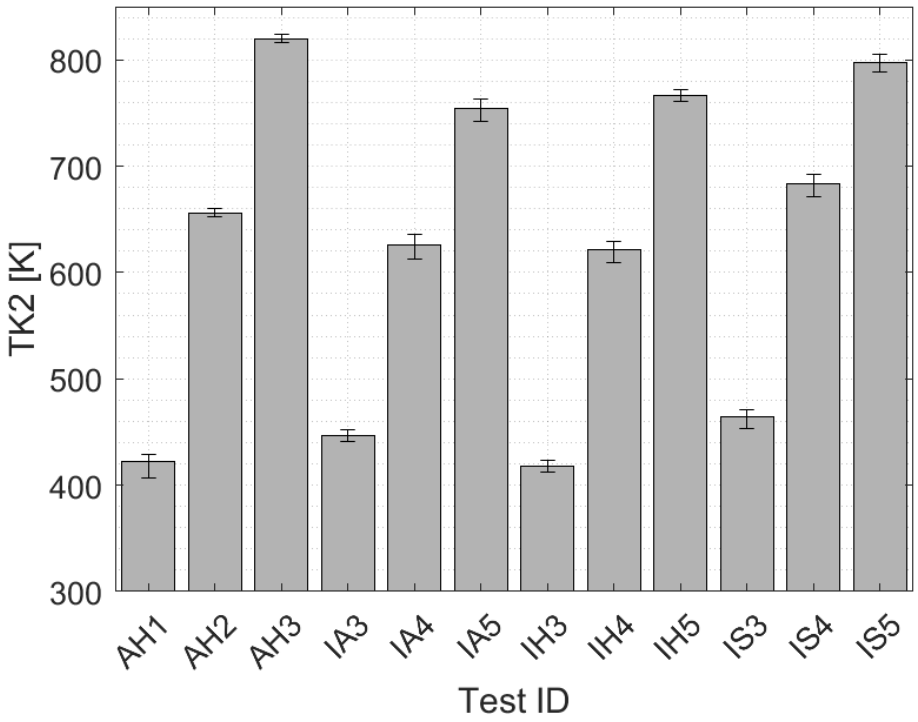

Figure 3.9: Measured peak temperature (TK2) for different heat flux levels and tube configurations.

The results are presented also in terms of TK1 and TK3, in Figure 3.10: the trend is confirmed in the TK1 plot, as the maximums can be found in the IS and AH, while different behaviour can be observed for the TK3.

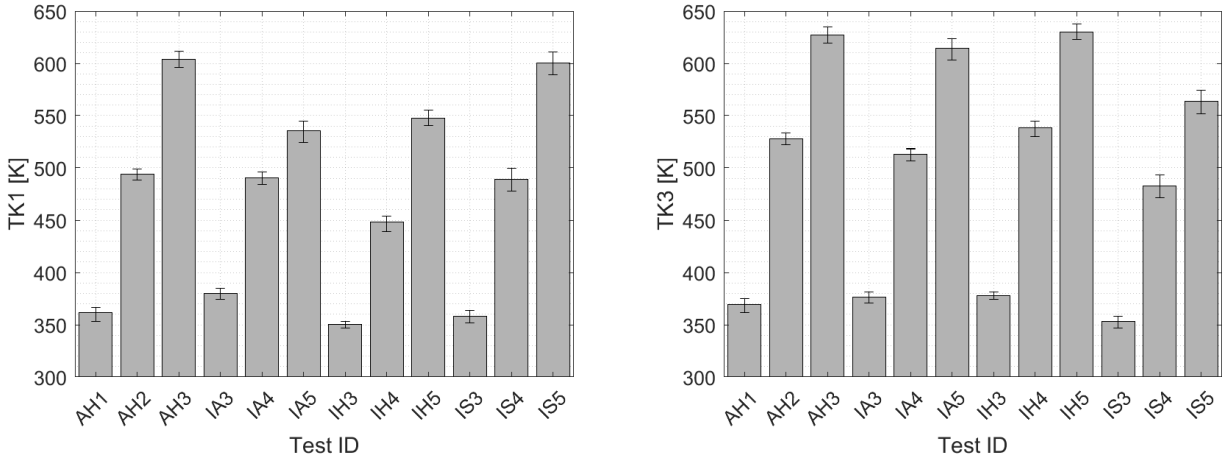

Figure 3.10: Measured TK1 (left) and TK3 (right) for different heat flux levels and tube configurations.

As shown in Figure 3.11, the temperature "profile" developed along the tube axis is different as the tube configuration changes. In particular, just for the smooth tube, the TK1 measure is higher than the TK3 one and two possible explanations can be found:

1. The focus was displaced closer to the TK1 during the tests performed with the Inconel Smooth receiver, so that the TK1 results higher than TK3;

2. Since the turbulence promoters enhance the heat transfer to the fluid, it is expected to have in TK3 position (along the length of the tube) an air temperature higher in the cases of IH-IA: so, in this position, the ΔT between wall and air is lower. In this case, the higher value of TK3 with respect to TK1 would be justified.

Please note that the same behaviour is verified also for the other heat flux levels.

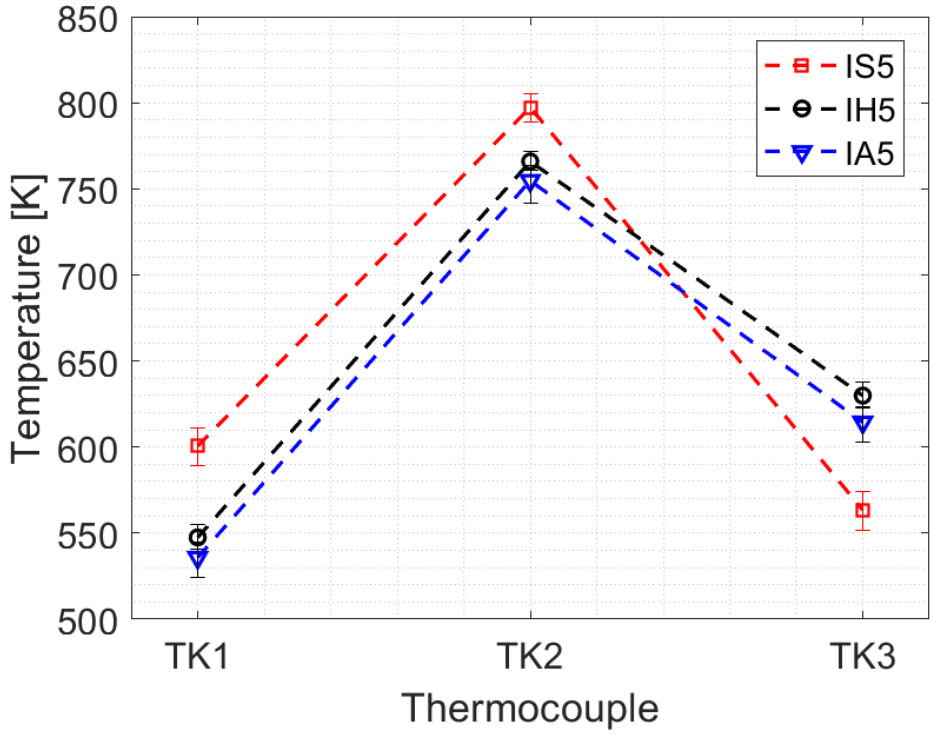

Figure 3.11: Temperature profile along the tube axis for three different configurations.

3.2.2 Oxidation

The samples were manufactured by means of additive manufacturing, but no surface coating was applied to that. This means that high concentrated heat flux can alter the wall surface properties by oxidizing it. In particular, emissivity and absorptivity can be affected by the oxidation level [31]. When the absorption factor increases, the amount of Sun power entering into the system increases. For this reason, it was carried out an analysis of the receivers behaviour in the same conditions, but in different day: as expected, the temperature results higher in the last tests, when oxidation already occurred (see Figure 3.12).

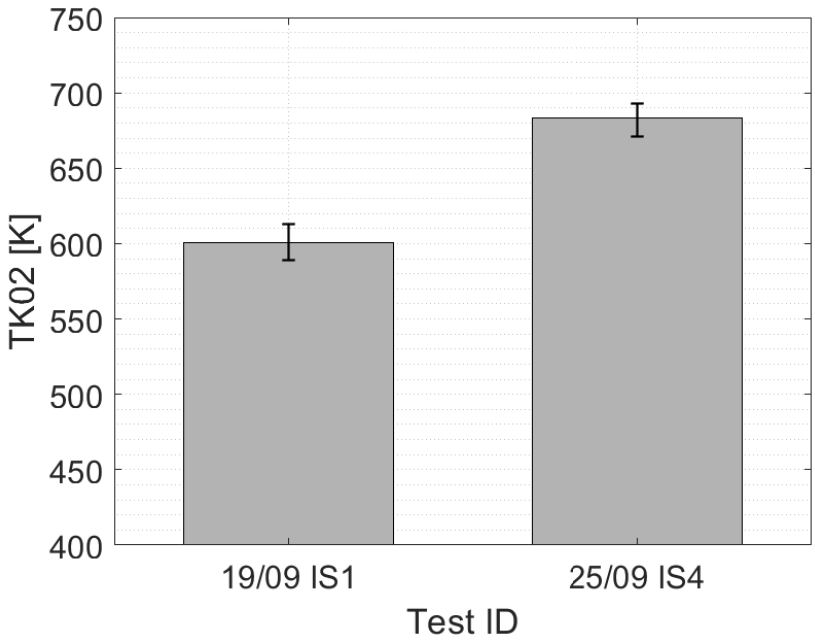

Figure 3.12: Measured TK2 for the IS tube in similar conditions, in different days.

Please note that the conditions are not exactly the same, there are very low differences in the peak flux and flow rate; by the way, the essential detail is that there were higher heat flux and lower flow rate in the test IS1. Considering the error bars, there could have been up to 100 K difference due to oxidation. The very same can be observed comparing the tests IA1 (performed on 22/09) with IA3 (performed on 25/09) and IA2 (performed on 22/09) with IA4 (performed on 25/09), see Figure 3.13.

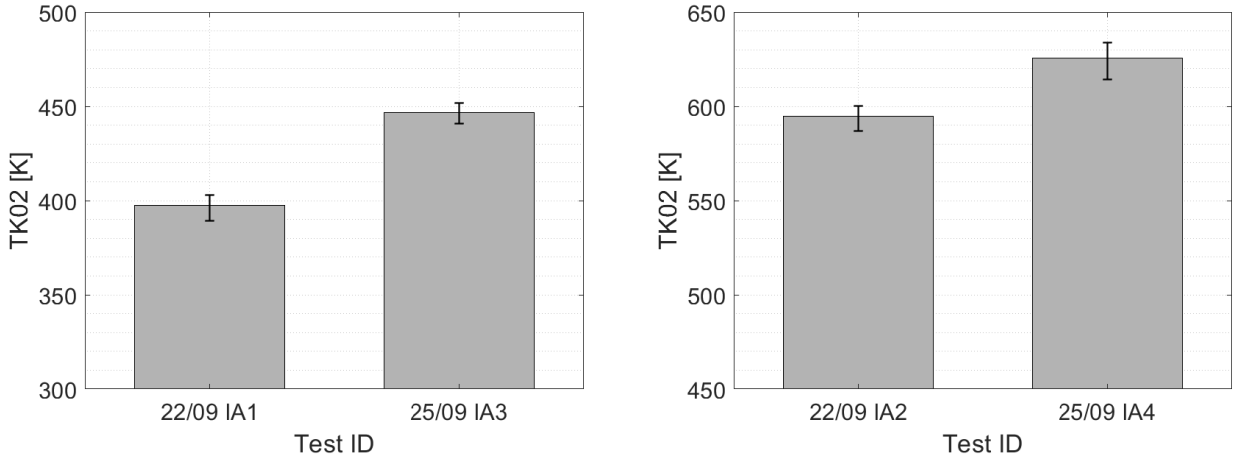

Figure 3.13: Measured TK2 for the IA tube in similar conditions, in different days.

The evidence of the oxidation will be relevant in the CFD analysis settings, as then it will be necessary to choose the day and the test to make a calibration of the emissivity and absorptivity.

3.2.3 Inconel vs AISI 316

One of the tube samples manufactured in 2017 was made of AISI 316: its lower market price could make it more attractive for the investors. So, the aim of its inclusion in the experimental campaign is to compare the performances with the Inconel 718 tubes.

As expected, the comparison with the Inconel tube equipped with helical ribs (IH), in the same test conditions, lead to a first evidence: the IH temperatures are lower than the AH ones. See Figure 3.14. Please note that the same analysis can be done comparing IA and AH samples, leading to the very same results: it means that the two best samples of the campaign are the Inconel ones equipped with turbulence promoters and that the interesting comparison will be the one between AH and IS tubes.

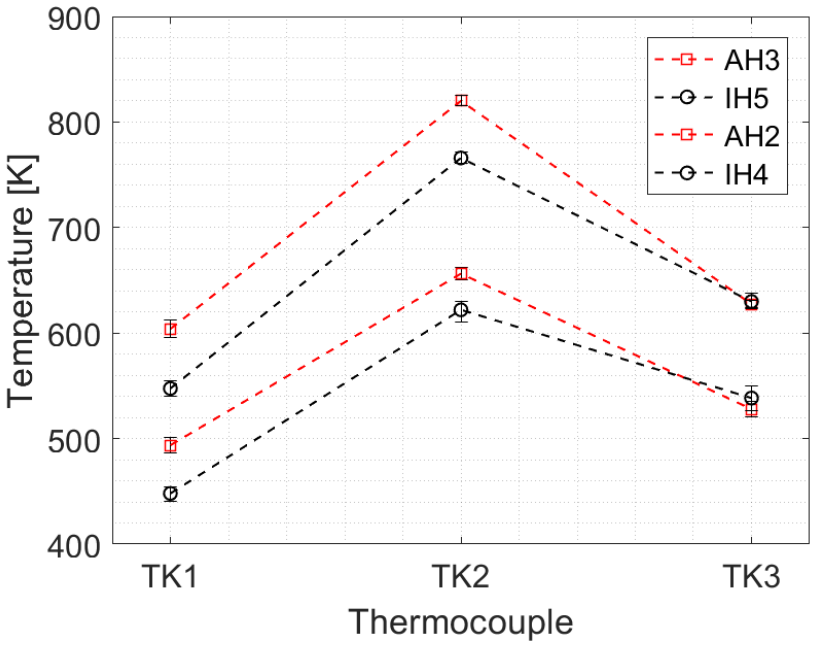

Figure 3.14: Comparison between AH and IH.

Instead of the previous comparison, it appears more difficult to forecast the behaviour of the IS tube versus the AH one. That's because, on the one hand, the first is made of Inconel, which has better heat transfer properties, while, on the other hand, the AISI 316 tube is equipped with turbulence promoters. The tests taken into account to make this comparison were performed under similar conditions: the IS tube appears to have lower wall temperatures with respect to the AH ones, even with an imposed heat flux that is slightly lower (see Table 3.6). In Figure 3.15, two different heat flux levels are investigated and more detailed analysis will be done through CFD simulations. What comes out is that:

- The AISI 316 tube equipped with helical turbulence promoters is worse than all the other configurations. So, the question is: will it be smart to carry out a CFD analysis for this sample, as no good preliminary results have been observed? In addition, the AH sample was tested just for couple of hours and no many tests have been selected. It means that it will be difficult to perform a characterization of the material;
- Despite of the better thermal behaviour of the IS against the AH sample, it could be interesting to carry out a thermo-economic analysis of the two configurations to go deeply into the comparison of the two. By the way, for the aim of this work, higher temperatures lead to higher stresses: so, the AH tube appears to have very low interest for the project.

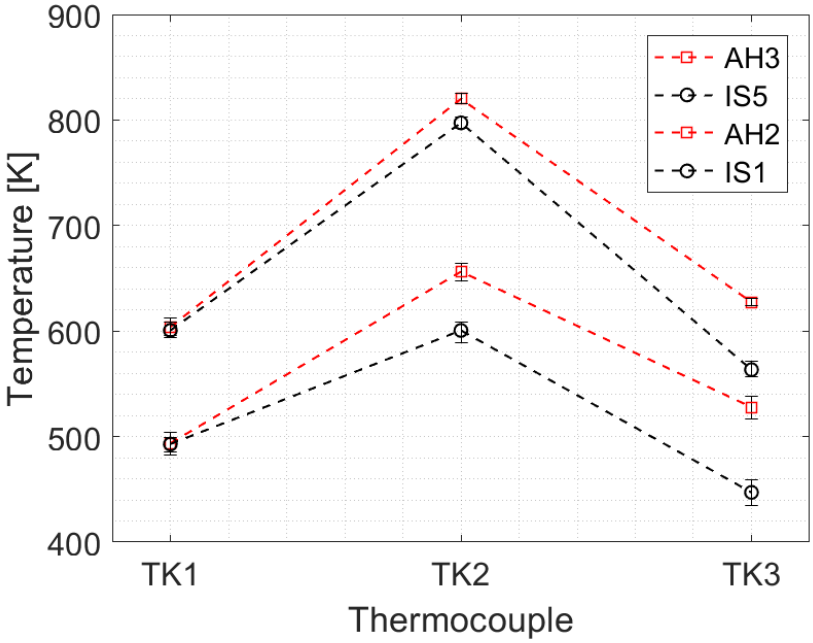

Figure 3.15: Comparison between AH and IS.

3.2.4 Air Temperature

In a pipe, if the fluid enters at a uniform temperature T(r,0) that is less than the surface one T_S, convection heat transfer occurs and a thermal boundary layer begins to develop. Moreover, if the tube surface condition is fixed by imposing either a uniform temperature or a uniform heat flux, a thermally fully developed condition is eventually reached. The shape of the fully developed temperature profile T(r,x) differs according to whether a uniform surface temperature or heat flux is maintained.
In the current experimental tests, the boundary heat flux has a Gaussian distribution and it is imposed just on half of the external surface. By the way, it is expected to have, partially, the temperature profile shown in Figure 3.16, on the very right. For this reason, the measure of the TK5, which is positioned at the receiver outlet and immersed in the core flow, won't be the *bulk temperature*. If convection heat transfer occurs, it can be defined the bulk or mean temperature so that the term c_pT_b is equal to the true rate of thermal energy (or enthalpy) advection integrated over the cross section. This true advection rate may be obtained by integrating the product of mass flux (ρu) and the thermal energy (or enthalpy) per unit mass, c_pT, over the cross section.
In the current data analysis, the air outlet temperature is not only far from the bulk temperature, but it appears to be a *near wall temperature.* It means that it is not possible to calculate any energy balance to verify the physics of the test. In fact, the energy balance would lead to a useful thermal power to the fluid higher than the imposed solar power (integrating the gaussian distribution over the surface).

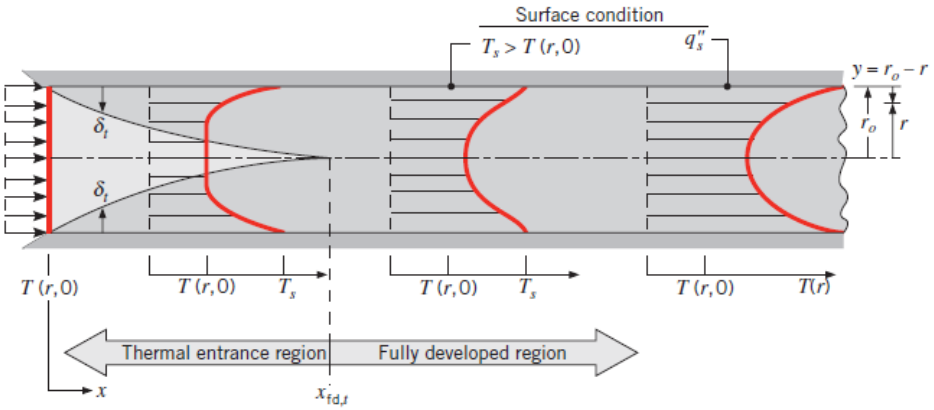

Figure 3.16: Thermal boundary layer development in a heated circular tube [32].

The tests IS4 and IH4 (see Table 3.7) were performed at comparable heat flux and air mass flow rate. The IH inner wall temperatures are lower with respect to the IS tubes, but the air temperature difference between outlet and inlet sections is, on the contrary, higher in the second case. This result is in disagreement with the energy conservation law, since the higher wall temperature measured in the case of the smooth tube should lead to higher heat losses and consequently, at comparable incident heat flux and mass flow rate, the air outlet temperature should be lower. The same conclusion is obtained comparing IS5 and IH5 and the bar plot is presented in Figure 3.17.

Test ID	Heat Flux [kW/mq]	TK1 [K]	TK2 [K]	TK3 [K]	m [g/s]	ΔT [K]
IS4	177.7	489.3	683.3	482.8	7.90	138.8
IH4	182.9	448.0	622.0	538.4	7.90	122.1
IS5	266.7	600.6	797.3	563.4	7.90	196.6
IH5	279.3	547.5	765.9	629.9	7.90	177.2

Table 3.7: Comparison between smooth and helical-ribbed Inconel tubes air outlet temperature.

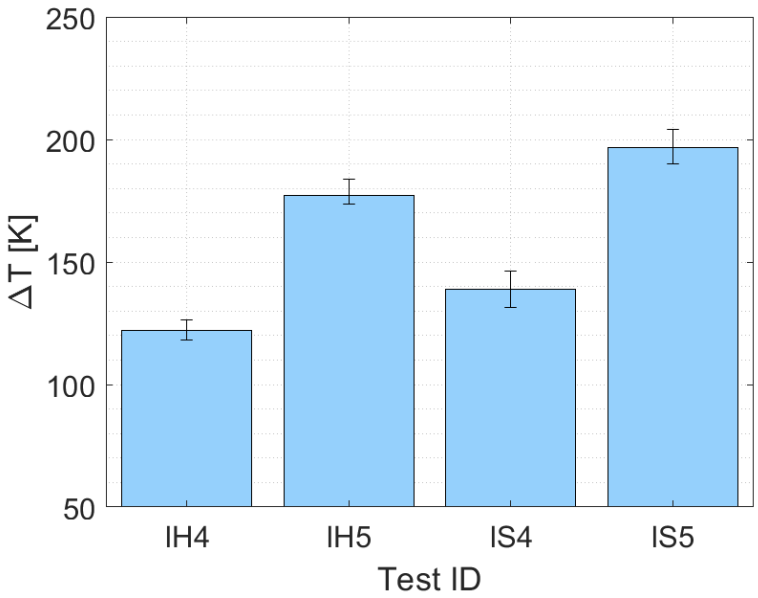

Figure 3.17: Comparison between smooth and helical-ribbed Inconel tubes air temperature jumps.

Furthermore, the tests IS4-IA4 and IS5-IA5 (see Table 3.8) were performed at comparable heat flux and air mass flow rate. The same occurs as before: the IA inner wall temperatures are lower with respect to the IS tubes, but the air temperature difference between outlet and inlet sections is, on the contrary, higher in the second case (see Figure 3.18).

Test ID	Heat Flux [kW/mq]	TK1 [K]	TK2 [K]	TK3 [K]	m [g/s]	\DT [K]
IS4	177.7	489.3	683.3	482.8	7.90	138.8
IA4	177.8	490.3	625.5	512.9	7.80	120.5
IS5	266.7	600.6	797.3	563.4	7.90	196.6
IA5	279.3	535.8	754.7	614.4	7.80	170.7

Table 3.8: Comparison between IS and IA tubes air outlet temperature.

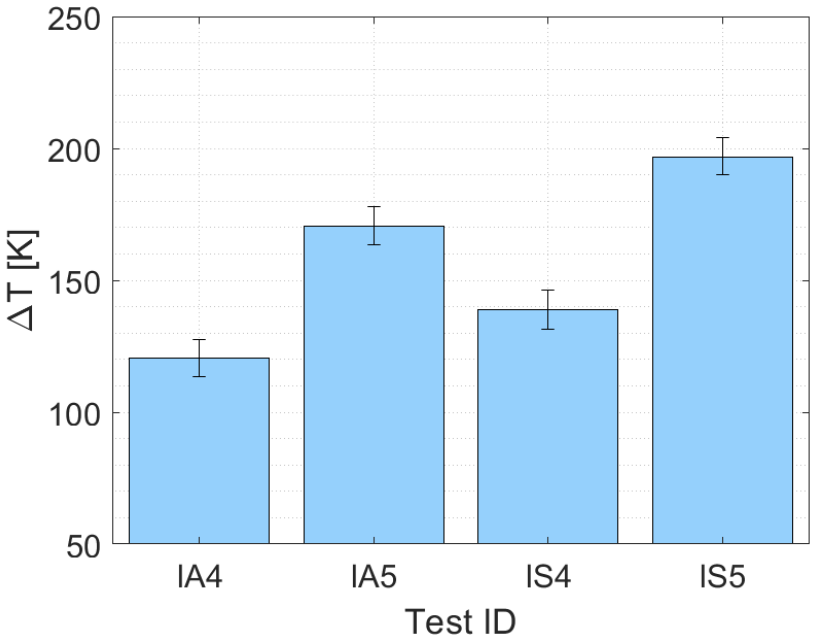

Figure 3.18: Comparison between IS and IA tubes air temperature jumps.

The conclusion is that, not only the measured temperature is a near wall temperature, but in the case of the smooth tube, the thermocouple was positioned closer the wall. This result makes invalid or, at least, useless the TK5 outputs.

4. CFD Analysis

Computational fluid dynamics or CFD is the analysis of systems involving fluid flow, heat transfer and associated phenomena, such as chemical reactions, by means of computer-based simulation [33]. The CFD codes are structured around the numerical algorithms that can tackle fluid flow problems. In order to provide easy access to their solving power all commercial CFD packages include sophisticated user interfaces to input problem parameters and to examine the results. Hence all codes contain three main elements: a pre-processor, a solver and a post-processor. In solving fluid flow problems it is needed to be aware that the underlying physics is complex and the results generated by a CFD code are at best as good as the physics (and chemistry) embedded in it and at worst as good as its operator. In the present work, the software chosen to go deep into the CFD analysis was *STAR-CCM+*, which is a Computational Aided Engineering (CAE) solution for solving multidisciplinary problems in both fluid and solid continuum mechanics, within a single integrated user interface. The *STAR-CCM+* simulation environment offers all stages required for carrying out engineering analyses, including [34]:

- Import and creation of geometries;
- Mesh generation;
- Solution of the governing equations;
- Analysis of the results;
- Automation of the simulation workflows for design exploration studies;
- Connection to other CAE software for co-simulation analysis.

In this chapter, 3D CFD models have been created for three of the four tubes (IS, IH, AH). The purpose is to validate the models against the experimental collected data, to have powerful tools to predict the thermal behaviour of the solar receivers. In addition, these models will be used to evaluate the thermo-mechanical stresses that can lead to a dramatic reduction of the lifetime of the component.

4.1 Setup

The three CFD models have some common settings, as the selection of the models, the material properties, the settings of the boundary conditions and the heat losses evaluation. All these features will be described in the current section.

4.1.1 Models

The 3D CFD conjugate heat-transfer models developed in this work include the solid and fluid regions of the irradiated tube, as well as the three thermocouples inserted in the wall. The turbulence model is the most important choice in the present work, but other models were selected for the Physics settings. Solid region - Inconel 718 or AISI 316:

- Three Dimensional;
- Steady State;
- Segregated Solid Energy;

Fluid region - Air:

- Three Dimensional: as the thermal driver has a Gaussian distribution, it is not possible to reduce the domain to a 2D domain;
- Steady State: as the comparison with experimental tests involves just the steady state tests;
- Segregated Flow: this model was found to be suitable for incompressible flows. The alternative was a Coupled Flow, which is optimized for compressible flow with large body forces, which was not the present case;
- Segregated Fluid Temperature: to solve the energy set of equations, the manual was consulted, and it was found a suggestion to use this model when no combustion occurs in the physics continuum;
- Ideal Gas;
- Turbulent, $k-\omega$ SST (Menter);
- All y+ wall treatment;
- Exact wall distance.

The above-mentioned model has been chosen, after a proper reasoning about the main benefits and drawback of the several RANS solvers, available in the STARCCM+ ambient:

- Reynolds stress turbulence model (RMS);
- Eddy viscosity models:
  - Spalart-Allmaras (1 equation model);
  - $k-\epsilon$ (2 equation model);
  - $k-\omega$ (2 equation model).

In opposition with eddy viscosity models, the Reynolds stress turbulence model accounts for the effects of turbulence anisotropy, solving additional transport equations for the Reynolds stresses, for the dissipation term, the turbulent diffusion term and the pressure strain term. Although RMS has higher accuracy in predicting complex flows, it carries significant computational cost, because of the higher number of equations to solve at each iteration. Spallart-Allmaras model solves the transport equation for the kinematic eddy viscosity and it's not optimal in describing transport processes in rapidly changing flows. The $k-\epsilon$ model is known to be unsatisfactory in predicting separating and rotating flows in the near wall region, resulting in an overestimation of turbulent kinetic energy k and the turbulent viscosity ν_t; this is mainly due to the empirical nature of the constants used in the equation for the dissipation rate ϵ [35]. On the other hand, $k-\omega$ has improved performance in modeling the boundary layers under adverse pressure gradients, which is a critical feature of the case under study: indeed, the turbulence promoters are designed specially to provide recirculation and rotating flows, in order to enhance heat transfer. Nevertheless, boundary layer computations are sensitive to ω values in the core stream, problem that does not occur for the $k-\epsilon$. Finally, SST Menter

$k-\omega$ resulted to be the most suitable model for the following main reason: it is able to work as a standard $k-\omega$ in the near wall region, and as the $k-\epsilon$ model in the fully turbulent region, using a blending function F_1, which adds an additional cross-diffusion term D_ω, activated only in the main stream.

4.1.2 Material Properties

The temperature dependence of the thermophysical properties such as thermal conductivity (k) and specific heat (c_p) of the Inconel 718 alloy is taken into account in the simulations (IS and IH) based on the following polynomial functions of the temperature T, in Kelvin.

$$k = 7.002 + 0.01514 \times T \quad [W/(mK)] \tag{4.1}$$

$$c_p = 384.4 + 0.1932 \times T \quad [J/kgK] \tag{4.2}$$

The above Inconel 718 polynomial function properties are shown below in Figure 4.1 and Figure 4.2, respectively.

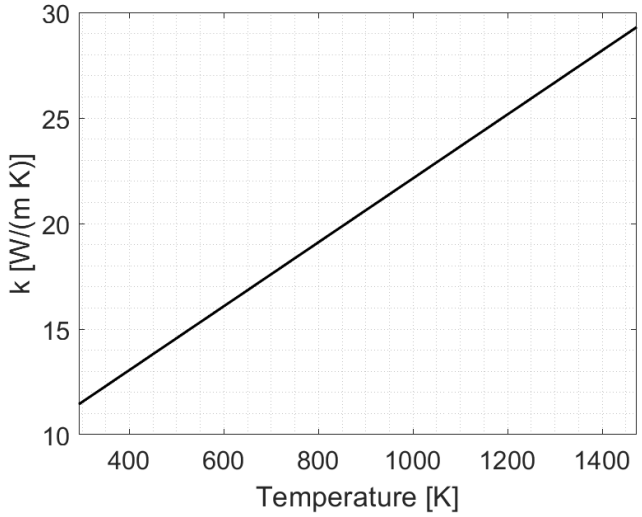

Figure 4.1: Inconel 718 thermal conductivity as a function of temperature.

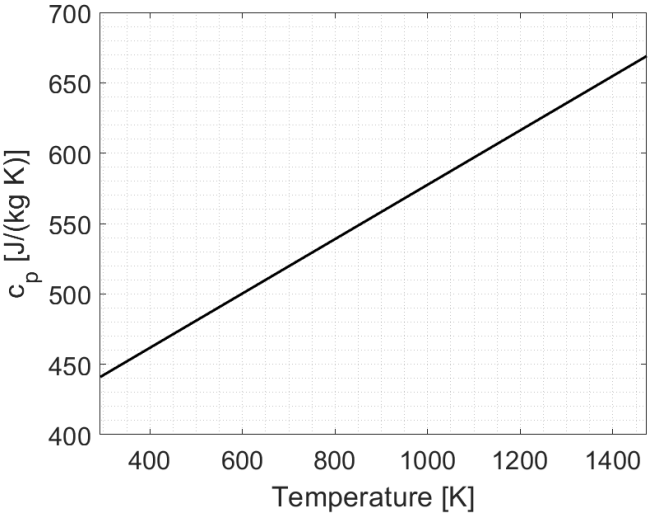

Figure 4.2: Inconel 718 specific heat capacity as a function of temperature.

The temperature dependence of the thermophysical properties such as density (ρ), thermal conductivity (k) and specific heat (c_p) of the AISI 316 alloy is taken into account in the simulations (AH) based on the following polynomial functions of the temperature T, in Kelvin.

$$\rho = 8043.3 - 0.3635 \times T - 6 \cdot 10^{-5} \times T^2 \quad [kg/m^3] \tag{4.3}$$

$$k = 13.98 + 1.502 \cdot 10^{-2} \times T \quad [W/(mK)] \tag{4.4}$$

$$c_p = 462.69 + 0.521 \times T - 1.171 \cdot 10^{-3} \times T^2 + 3.366 \cdot 10^{-6} \times T^3 - 2.196 \cdot 10^{-9} \times T^4 \quad [J/kgK] \tag{4.5}$$

The above AISI 316 polynomial function properties are shown below in Figure 4.3, Figure 4.4 and Figure 4.5, respectively.

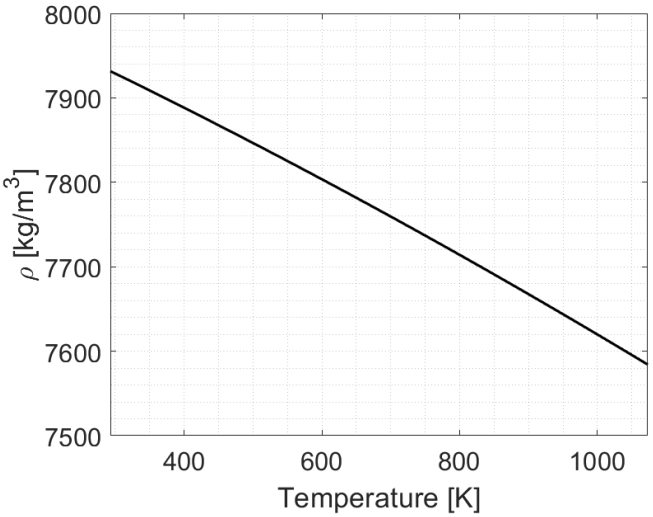

Figure 4.3: AISI 316 density as a function of temperature.

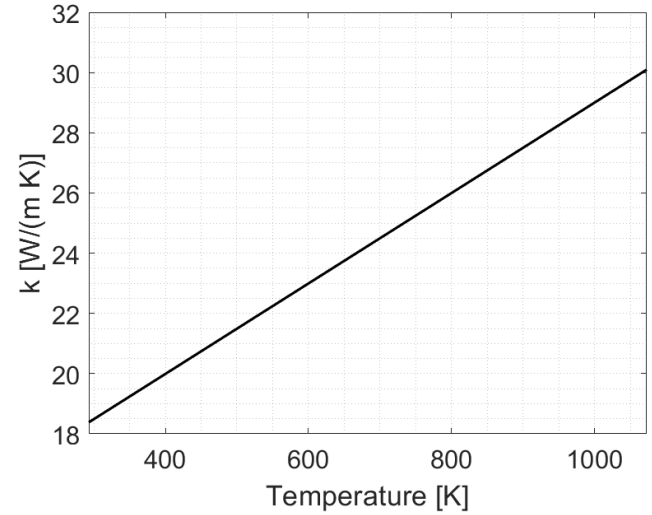

Figure 4.4: AISI 316 thermal conductivity as a function of temperature.

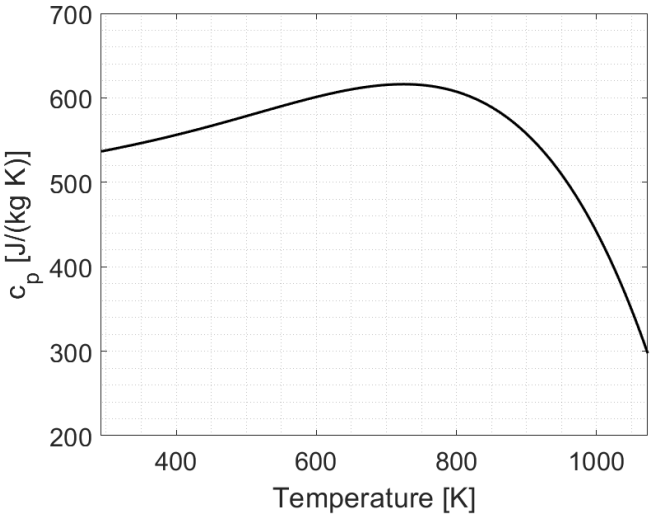

Figure 4.5: AISI 316 specific heat capacity as a function of temperature.

The following constant molecular weight (W_{air}) and Prandtl number (Pr_{air}) are chosen for the simulation of the air:

$$W_{air} = 28.9664 \quad [kg/kmol] \tag{4.6}$$

$$Pr_{air} = 0.7 \quad [-] \tag{4.7}$$

The temperature dependence of the material properties such as thermal conductivity (k_{air}), specific heat ($c_{p,air}$) and dynamic viscosity (μ_{air}) of the air is also taken into account in the simulations based on the following polynomial functions of the temperature T, in Kelvin [32]:

$$k_{air} = 0.0013 + 9.28 \cdot 10^{-5} \times T - 3.301 \cdot 10^{-8} \times T^2 + 6.52 \cdot 10^{-12} \times T^3 \quad [W/(mK)] \tag{4.8}$$

$$c_{pair} = 1136.5 - 7.6478 \cdot 10^{-1} \times T + 1.4917 \cdot 10^{-3} \times T^2 - 7.4111 \cdot 10^{-7} \times T^3 \quad [J/(kgK)] \tag{4.9}$$

$$\mu_{air} = 3.794 \cdot 10^{-6} + 5.450 \cdot 10^{-8} \times T - 1.555 \cdot 10^{-11} \times T^2 \quad [Pa \times s] \tag{4.10}$$

The above air polynomial function properties are shown below in Figure 4.6, Figure 4.7 and Figure 4.8 respectively.

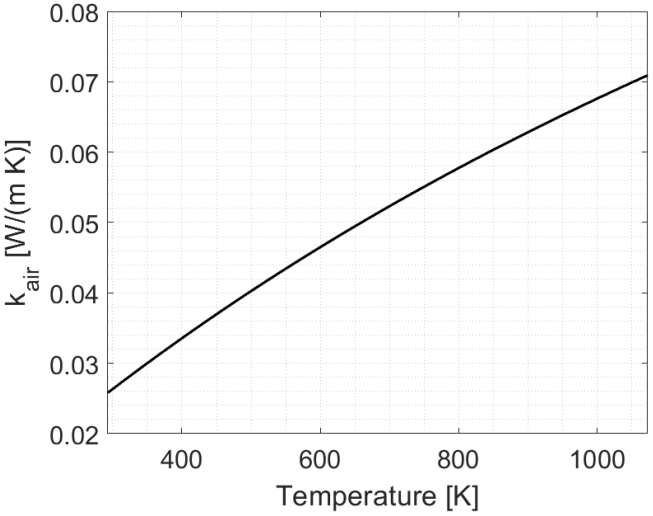

Figure 4.6: Air thermal conductivity as a function of temperature.

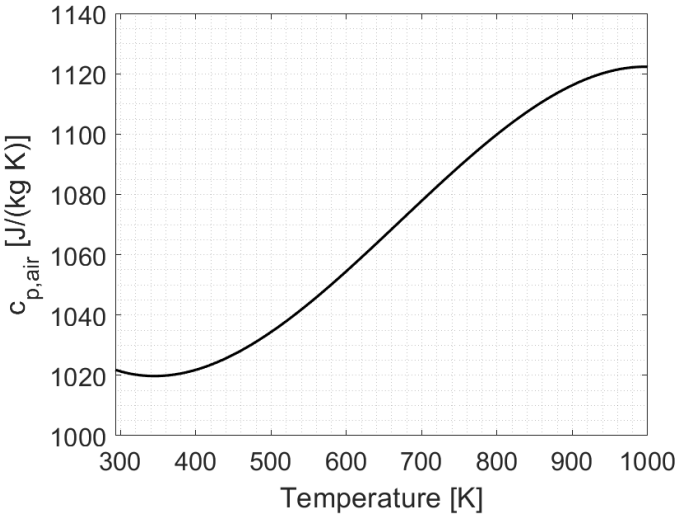

Figure 4.7: Air specific heat capacity as a function of temperature.

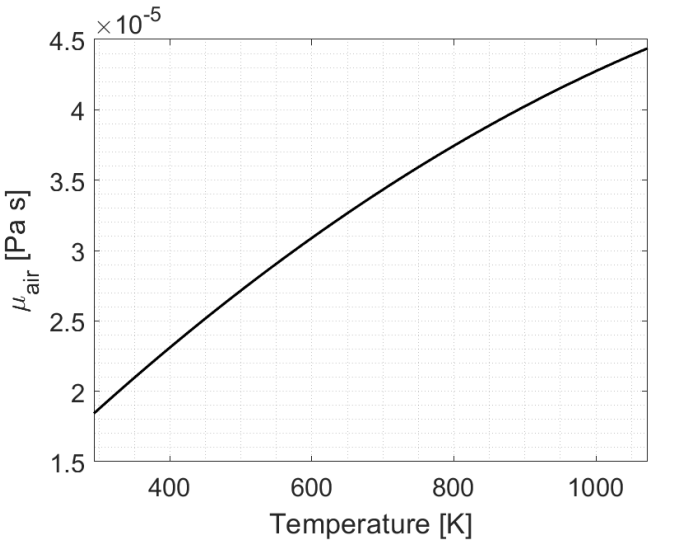

Figure 4.8: Air dynamic viscosity as a function of temperature.

There is no polynomial function shown above for the air density as it is not needed to describe it since an ideal gas model is chosen for the fluid. Therefore, the air density is evaluated according to the pressure and temperature of the fluid itself.

4.1.3 Boundary Conditions

The following boundary conditions have been applied to the simulated tubes:

- Inlet Mass Flow Rate, applied to the inlet area, which is always about 40 l/min;
- Outlet Pressure $p_{out} = 10$ bar, applied to the outlet area;
- Inlet Air Temperature $T_{in} = 300K$;
- Gaussian Solar Heat Flux applied to the irradiated side (see Figure 4.10) of the tube. The adopted Gaussian distribution of the solar heat flux is shown below in Figure 4.10: the peak flux ranged from 50 kW/m^2 up to 300 kW/m^2 depending on the selected test.

- Convective Heat losses for natural convection, applied to every dispersing surface. The convective heat transfer coefficient will be defined model by model;
- Radiative Heat losses with an emissivity distribution that follows the Gaussian heat flux and which will be calibrated for each tube.
- The extremes of the solid part are considered adiabatic;

The domain shown in Figure 4.10 is the one used for the Inconel Smooth model: thanks to its symmetry, both in the geometry and in the thermal driver and boundary conditions, it is possible to reduce the computed domain to half. For the Inconel Helices and AISI 316 Helices solar receivers, the entire domain has to be computed.

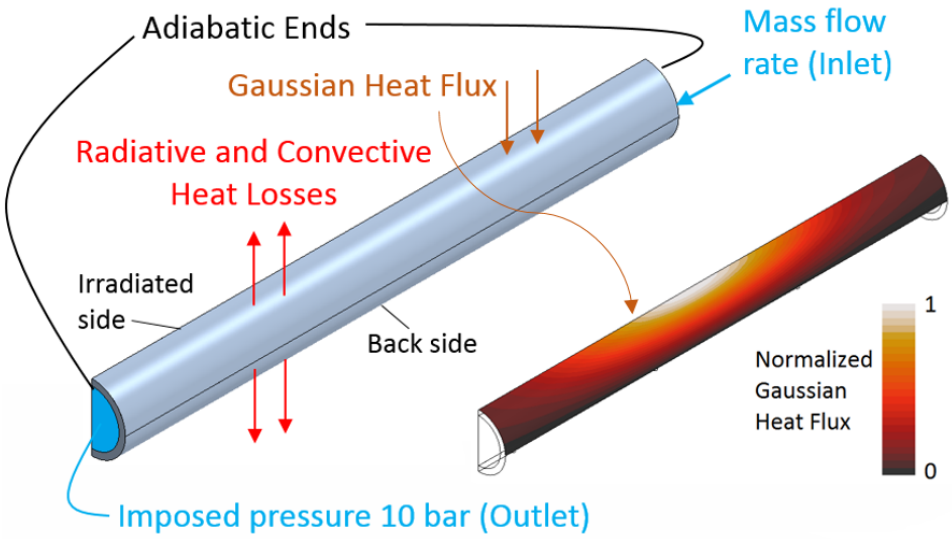

Figure 4.9: Boundary conditions applied and normalized Gaussian heat flux distribution.

The thermal driver of the CFD model is the concentrated solar radiation. The sunlight is focused on the center of the test tube and only one side of the test tube is irradiated (the back side is considered completely shadowed). The Gaussian distribution, defined in [23], is defined by:

$$\varphi = \varphi_{peak} \cdot exp\left[-\frac{1}{2} \cdot \left(\frac{x^2}{\sigma_x^2} + \frac{z^2}{\sigma_z^2}\right)\right] \cdot cos\theta \quad [kW/m^2], \tag{4.11}$$

where σ_x and σ_z are the standard deviations provided by [23]: $\sigma_x = \sigma_z = 0.064$. The resulting heat flux distribution given in Equation 4.11 can be visualized in the following example, where the peak flux is 80 kW/m^2:

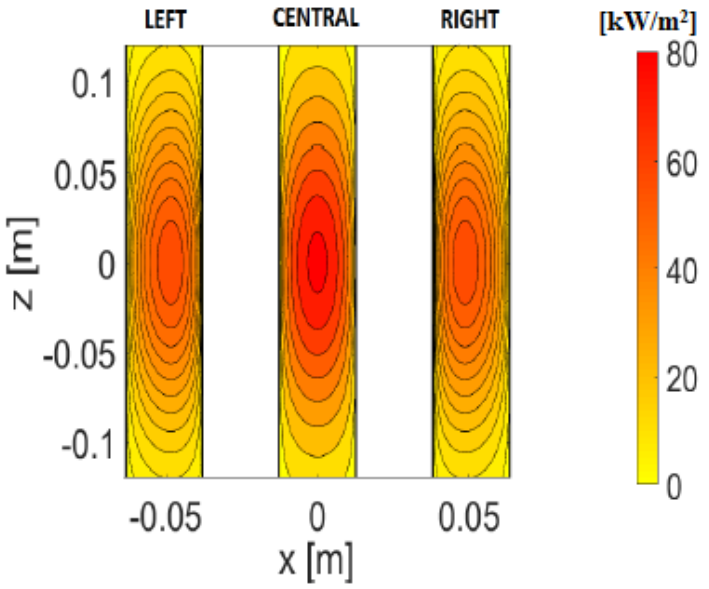

Figure 4.10: Concentrated solar radiation profiles on test tubes at different positions [29].

Then, the heat flux distribution has to be multiplied by the cosine of the local incident angle, to take into account the radial curvature of the tube surface (see Figure 4.11). At the tube extremities ($\theta = \pm\pi/2$) the flux absorbed is null, while on tube irradiated side ($\theta = 0$) the incident flux is maximum.

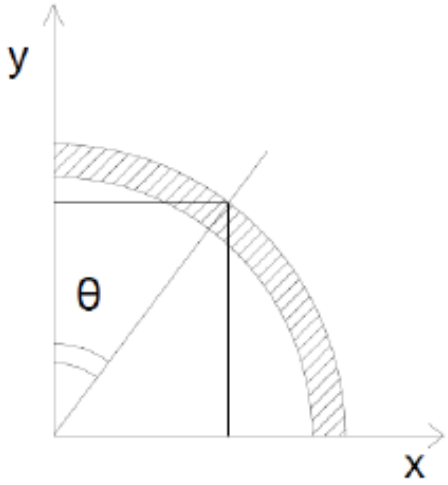

Figure 4.11: Curvature of the pipes [29].

4.1.4 Heat Losses Evaluation

The model computes the convective heat losses from the pipe towards the environment by means of Newton's cooling law, as a function of the wall surface temperature (computed by CFD), of the ambient temperature and of the heat transfer coefficient. The ambient temperature was monitored during the test sessions, while the heat transfer coefficient has been estimated by means of the following

empirical correlation [36]:

$$Nu = \left[0.825 + \frac{0.387 \cdot Ra^{1/6}}{\left[1 + \left(\left(\frac{0.492}{Pr}\right)^{9/16}\right)\right]^{8/27}} \right]^2, \tag{4.12}$$

where Nu, Pr and Ra are the Nusselt, Rayleigh and Prandtl numbers evaluated at ambient temperature, respectively. This correlation is for natural convection (as the test bed is protected from the wind) in laminar flow (Ra < 10^9), as in the cases examined here; however, it was developed for isothermal vertical planes, while our sample is a tube with a non-uniform temperature distribution. The resulting heat transfer coefficient varies case by case, as the Rayleight number depends also on the external surface temperature of the tube:

$$Ra = Gr \cdot Pr \tag{4.13}$$

$$Gr = \frac{gL^3\beta(T_s - T_\infty)}{\nu^2}, \tag{4.14}$$

where g is the standard gravity, L is the characteristic length of the body (length, here), β is thermal expansion factor, ν is the kinematic viscosity, T_∞ is the asymptotic temperature (T_{amb}, here) and T_s is the mean surface temperature of the plate (tube surface). So, it is expected to have relative higher heat transfer coefficient in the case of higher peak fluxes (so, higher temperatures, so higher Nu):

$$h_{nconv} = \frac{Nu \cdot k}{L} \tag{4.15}$$

So, this heat transfer coefficient will be evaluated and defined case by case, but the range is about 5-15 $W/(m^2K)$. Then, the convective heat losses are evaluated by means of Equation 4.18:

$$\Phi_{nconv} = h_{nconv} A(T_s - T_\infty) \quad [W] \tag{4.16}$$

The radiative heat losses that occur from the external surface of the tube are calculated in the model according to the Stefan-Boltzmann's law, based again on the wall surface temperature computed by CFD. The latter requires defining the emissivity of Inconel 718, which may range from about 0.2 to more than 0.9 depending on the oxidation grade [31].
Figure 4.12 shows the emissivity vs surface temperature for the Inconel 718 in "as-received" conditions (this condition means that the component has never been irradiated yet). The results indicate a moderately low emissivity which increases from a value of approximately 0.24 at a surface temperature of 200°C to 0.33 at a temperature of 1000°C. For the temperatures of interest in the current experimental campaign, the lower limit of emissivity can be considered approximately 0.3. In addition, the back wall is considered a not-oxidized surface at almost uniform temperature; thus, the emissivity is set to 0.3, according to the results presented in [31].

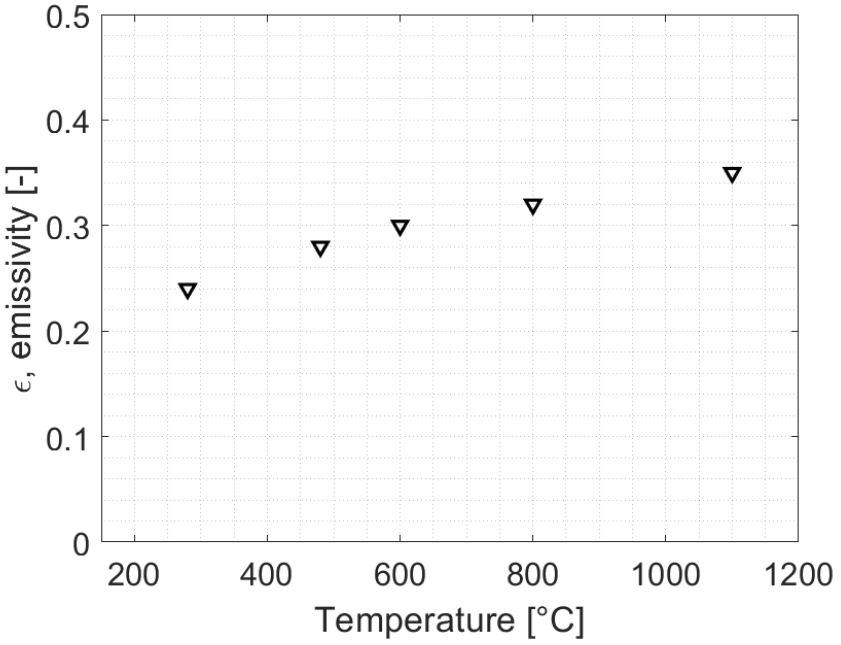

Figure 4.12: Emissivity vs sample temperature for Inconel 718 in "as-received" condition [31].

As no surface coating was applied to the tube surface, oxidation occurred (Figure 4.13) and it is expected to have higher emissivity and absorption factor. In particular, as the emissivity strongly depends on temperature, a first good approximation could be that the distribution of the surface emissivity on the irradiated wall have a Gaussian shape, due to the imposed thermal driver that determines the surface oxidation. So, the exact shape of the Gaussian function is determined iteratively, simulating the smooth tube in the conditions corresponding to a selected test, until the wall thickness temperatures approaches the measured one. Please note that the very correct way to do such a calibration would be comparing the air outlet temperatures, to ensure that the calorimetry is the same between the experiment and the CFD. Unfortunately, due to what is presented in Section 3.2.4, it is not possible to use that experimental data. The resulting Gaussian shapes will be presented case by case.

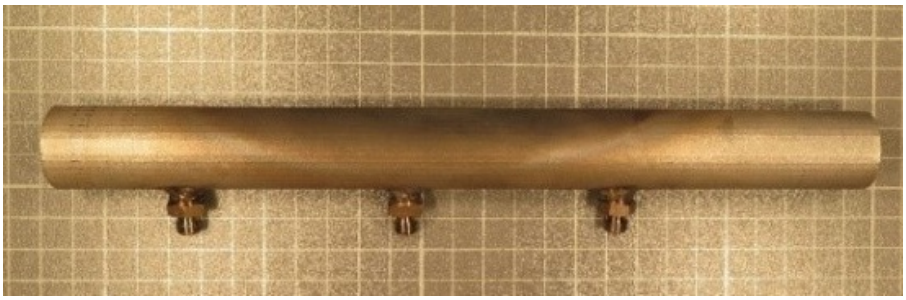

Figure 4.13: An oxidized sample tube after the test.

In [31] the emissivity as a function of temperature is presented also for oxidized samples, but the experimental conditions were 1000 °C - 1100 °C - 1142 °C for 15-30-60 minutes. As the values both of temperature and exposure time are kindly different from current work, it won't be used as a reference for the peak values of emissivity.
For what concerns the absorption factor, it is not temperature dependent, but it increases when oxidation occurs: so, as the samples are clearly oxidized in a certain region, there it is expected to have

an increasing absorptivity. In other words, this coefficient follows, as the emissivity, the Gaussian distribution of the flux.

4.2 Inconel Smooth (IS) receiver

The first model refers to the Inconel Smooth (IS) tube, which is the simplest among the tested tube for two main reasons. First, it is possible to reduce the domain to half, and so the computational cost. Second, the absence of internal turbulence promoters makes it easier both in terms of mesh generation and post processing of hydraulic and thermal fields.
Once the model has been set, as explained in Section 4.1, the roadmap followed to perform the CFD analysis has been the following (see also Figure 4.14):

1. First, the mesh has to be built and its quality has to be checked through more than one specific parameter. In addition, the grid independence study has to be performed to be sure about the robustness of the numerical model;

2. Then, the emissivity and the absorptivity have to be calibrated on a selected test: for the IS tube the two parameters will be considered equal, while for the other 3D CFD models a two-parameters calibration will be preferred. In particular, the calibration ends when the output temperatures from STAR-CCM+ and the ones from the experimental analysis are in good agreement. Please note that the very correct way to do that would be to couple this comparison with a calorimetry, in order to check also the fluid thermal behaviour: as the measured temperature of the outlet air is not reliable, this won't be possible;

3. Once the calibration has been done, all the ranges of solar peak heat flux need to be explored (i.e. all the valid quasi-steady state tests) to compare the CFD model with the experimental results: if the wall temperatures are in good agreement, which means that the two values crosses each other within the error bars, the model in the STAR-CCM+ environment can be considered valid;

4. At this step, the last one, the model represents a powerful tool, which could be used to go into deep in the thermo-hydraulic analysis of the tubes. For example, some considerations could be done, as:

    - As the samples were manufactured by means of additive manufacturing, the internal surface of the wall was not exactly smooth: so, a sort of sensitivity analysis about the roughness of the internal wall could be performed;
    - As it has been explained more than once, the oxidation affects the thermal behaviour of the samples because of the absence of surface coating. So, the absorption factor rises as it increases the amount of energy irradiated on the external surface of the tube. This phenomena generates a mismatch between two tests performed on two different days, but in the same conditions: if the model has been already validated, it can be used to calibrate the peak of the absorption factor to plot its trend as a function of the irradiated energy in [Wh];
    - In literature there no exists studies like the present one: in particular, no other tubes irradiated just on one half of the surface, with non-uniform heat flux applied on (here, a Gaussian distribution) have been compared with the empirical correlations available on books, like the Sieder-Taye one. This kind of analysis will be performed for all the tubes, allowing to deeply understad which solution could be the best one.

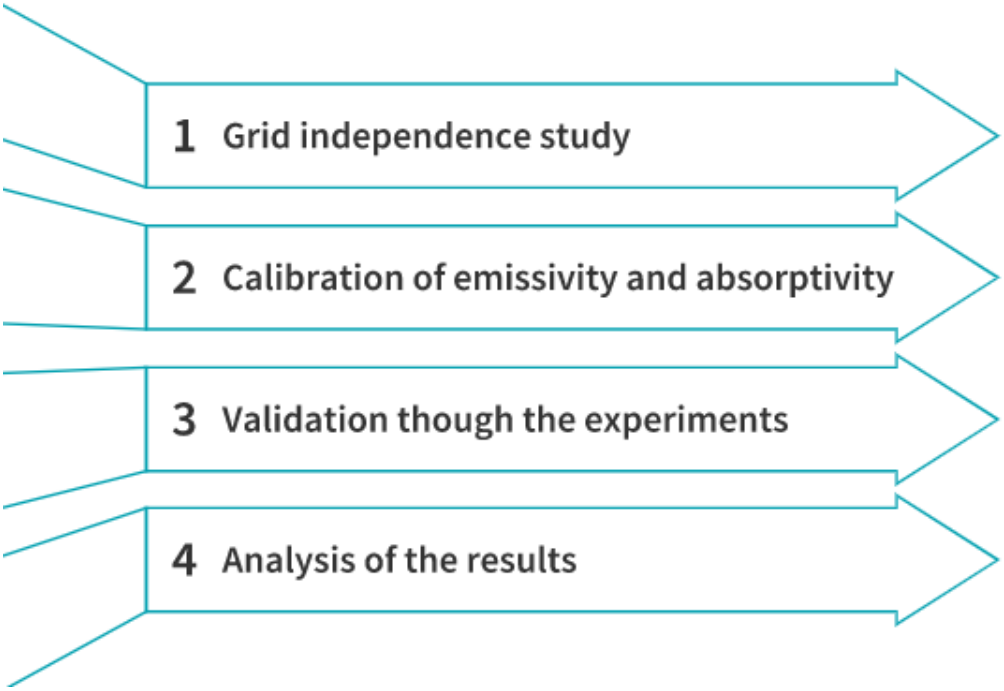

Figure 4.14: CFD analysis roadmap.

The computed domain is presented in Figure 4.15 and Figure 4.16. It includes the following regions:

- Solid region 1 - Inconel 718;
- SOlid region 2 - thermocouples TK1, TK2 and TK3;
- Fluid region - Air.

Please note that the contact thermal resistance between the sensor and the tube wall is assumed to be negligible.

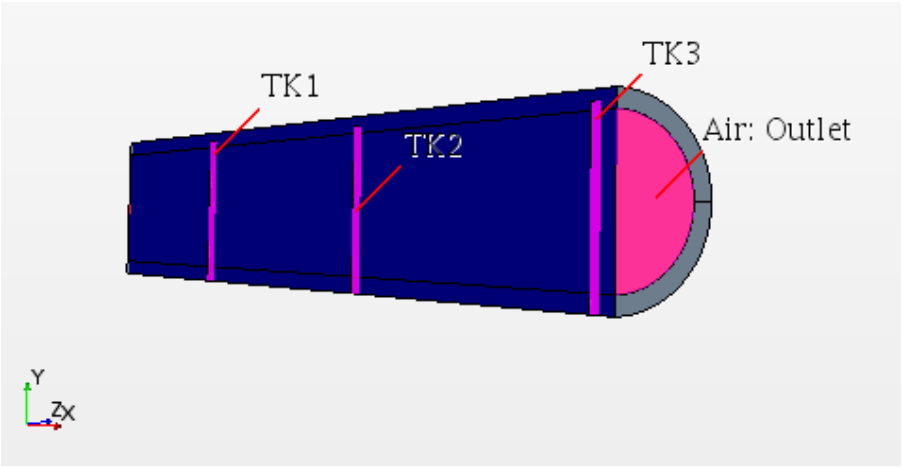

Figure 4.15: Computational domain of the IS tube: thermocouples and air volume.

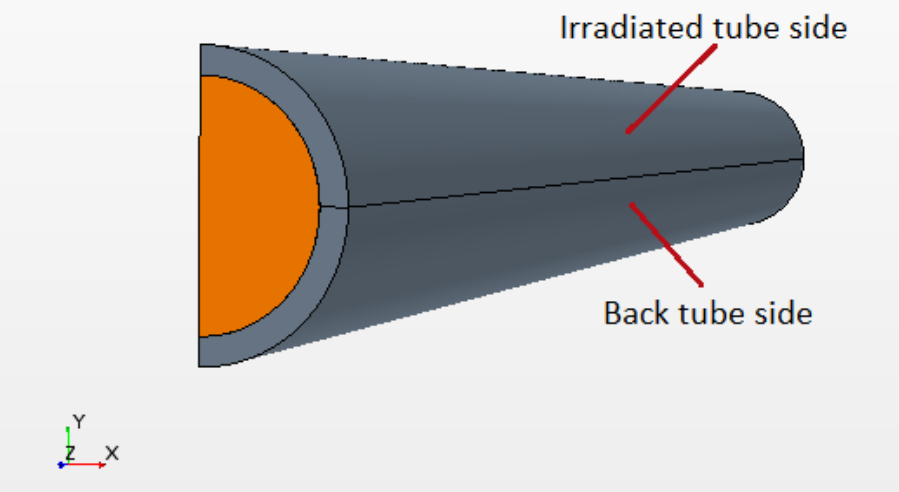

Figure 4.16: Computational domain of the IS tube: solid region

4.2.1 Mesh Generation and Grid Independence

The discretization of the domain has been done according to the main turbulent phenomenon and to ensure a good compromise between computational cost and accuracy of the results. The flow regime is turbulent ($Re = 2.4 \cdot 10^4$ at the inlet section) and the mesh consists of polyhedral cells with 8 prism layers at the solid/fluid interfaces ($y+ \approx 1$, as the Prandtl number for the air is ≈ 1 in all the tested thermal-hydraulic conditions). Through appropriate surface control, the size of the grid has been imposed to decrease as it approaches the walls, as higher and rapid variations of the main physical parameters are expected to occur there. An automated surface repair function is also included to automatically correct errors made by the software while generating the mesh. The selected mesh is shown in Figure 4.17.

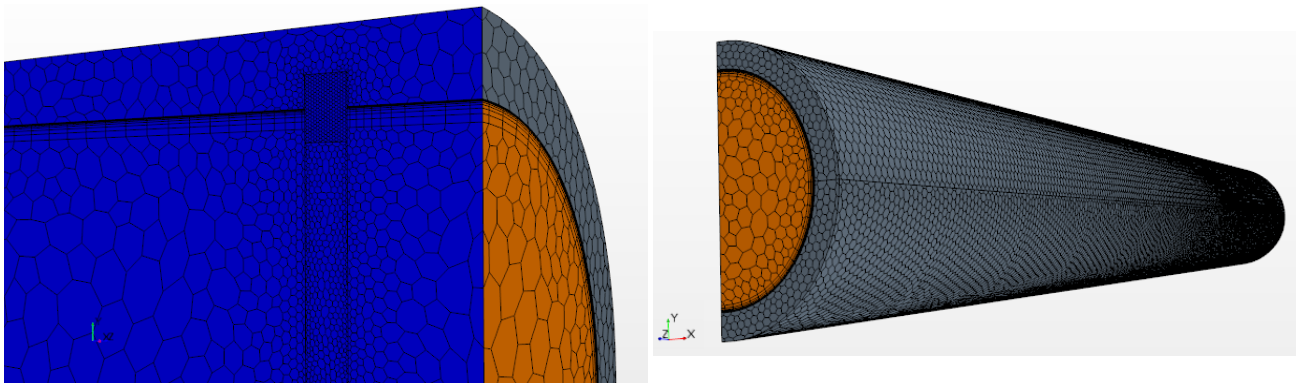

Figure 4.17: Mesh generated for the IS tube..

A structured prism layer is set at the wall, to highlight the behavior of the flow in the viscous sublayer; hence, y+ at the wall is verified to be ≈ 1, as shown in Figure 4.18. The number of prisms selected is 8, as with 10 the wall y+ was everywhere lower than 0.1. Three peaks occurs, as expected, where the thermocouples holes are located.

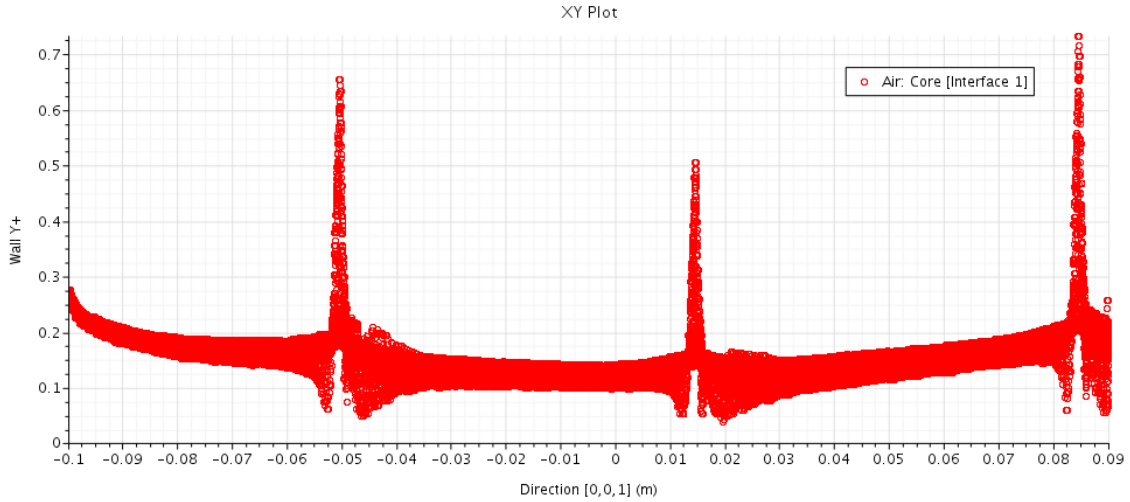

Figure 4.18: Wall y+ $\approx$ 1.

The mesh appeared to be very good: the 99.6 % of the cells has a cell quality between 0.7 and 1, while the worst cell quality was 0.42 (just for 2 cells over 15000). A bad cell quality means that the flat cells has highly non-orthogonal faces, which appears to not occur in the selected mesh. Furthermore, also the skewness angle was checked: it represents the angle between a face normal and the vector that connects two neighboring cell centroids; cells with a skewness angle greater than 85 are considered bad and the ones with 90 angle or greater typically result in convergence issues: here, the result was satisfactory, as shown in the Figure 4.19. Here, the result is satisfactory, as and the same occurs in the other regions of the CAD (and even better).

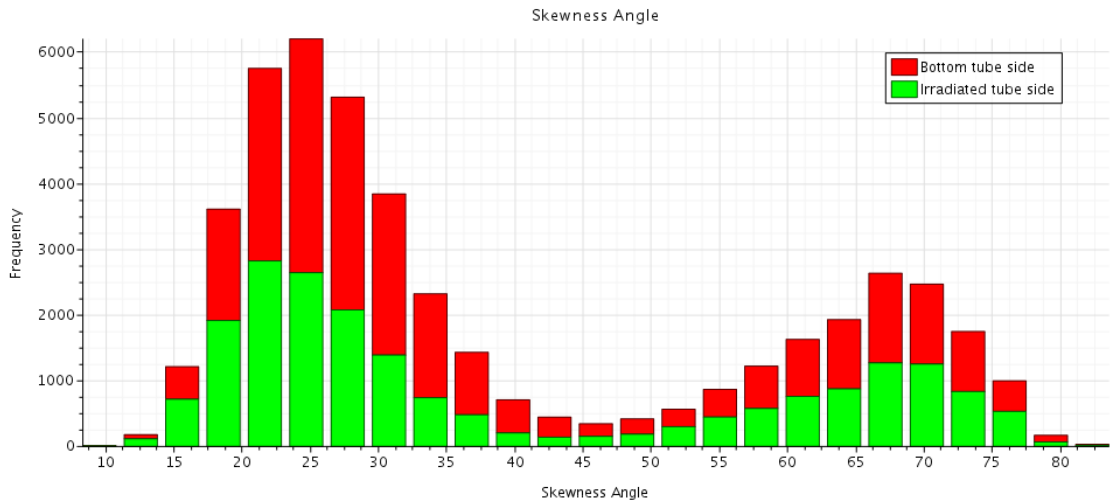

Figure 4.19: Skewness angle in the solid region.

Once the grid was generated, the space convergence study has been carried out to ensure that numerical results were independent of both the polygonal mesh, and the prism layer resolution: the grid independence study, as the calibration, have been performed on the test IS4. Mean outlet velocity, temperature TK3, as well as the total pressure drop have been evaluated, to show that they converge with a monotonic trend, increasing the total number of cells. The grid independence study in the core region has been achieved by changing the base size of the polygonal cells, while keeping the number of prisms fixed, and making sure that the outer prisms had similar dimensions with the above

neighboring cells, to enhance the information exchange between the two regions. The total numbers of cells for the analyzed grids are approximately 100000, 250000, 500000, with 8 prisms (see Figure 4.20).

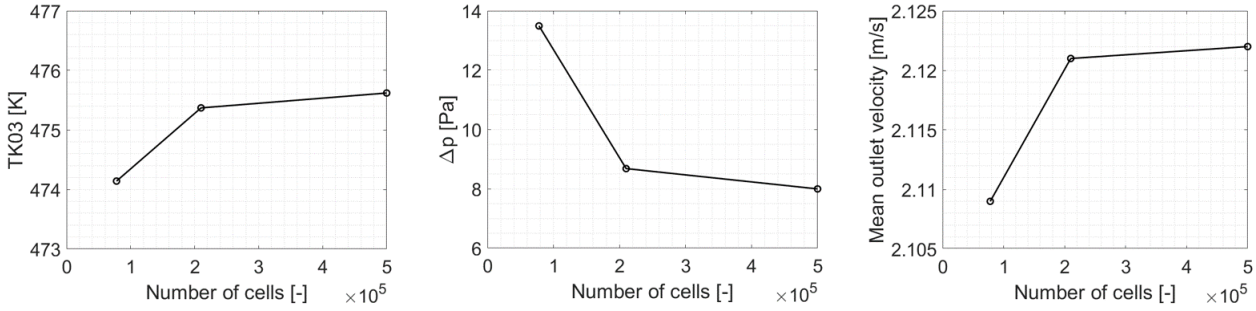

Figure 4.20: Convergence study in terms of total number of cells.

Similar procedure has been done to show the prism layer independence study, as different values of number of prisms are tested, while maintaining the global core refinement constant. Results related to the above described study are reported in Figure 4.43.

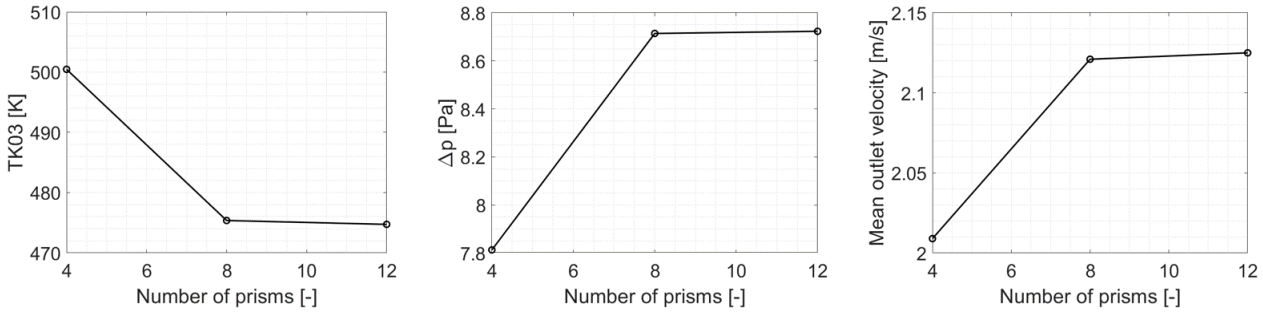

Figure 4.21: Convergence study in terms of number of prism layers.

4.2.2 Calibration

As already explained in Section 4.1.4, the four tubes were not coated. So, the emissivity and absorptivity are not known a priori and it is necessary a first calibration to make possible the validation. The selected test for the calibration is the IS4, which was performed on September 25^{th}. Due to the evidence of the oxidation (Section 3.2.2), the test selected for the calibration and the ones selected for the validation of the model refer to the same operation day. In this way, it possible to assume that the effects of the oxidation over the two coefficients are negligible, as IS3, IS4 and IS5 were performed consequently and without any transient test between them. The resulting emissivity is shown in Figure 4.22. In the case of the IS tube, it was performed a one-parameter calibration, setting the absorptivity equal to the emissivity. Furthermore, the back side surface emissivity is set to 0.3, as it can be considered "as-received".

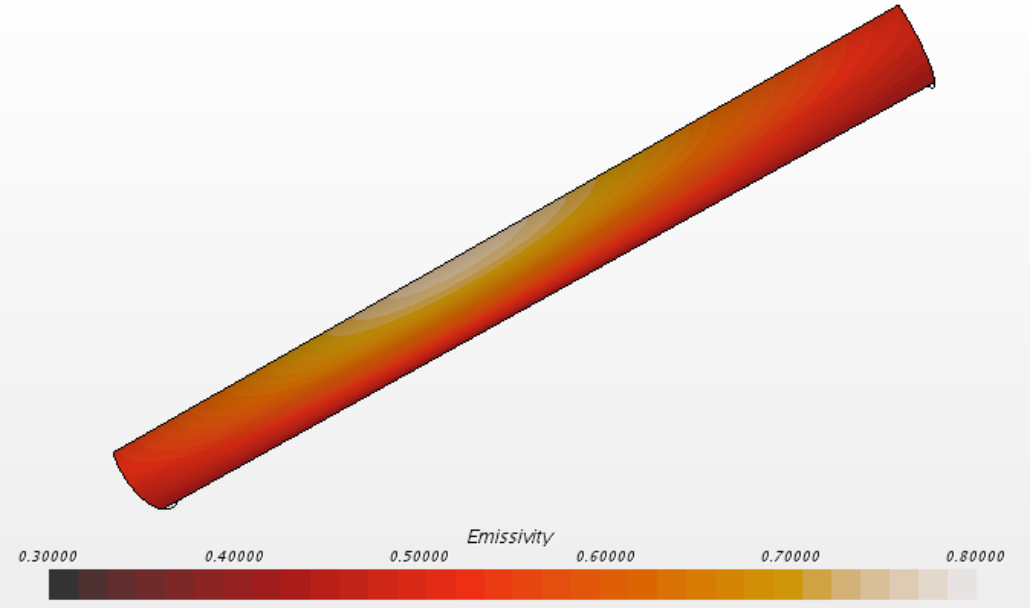

Figure 4.22: Emissivity calibrated on test IS4, irradiated side.

Once the emissivity and the absorptivity were calibrated, it has been "adjusted" the heat transfer coefficient for natural convection losses. First, the average of the temperature measurements of the IS4 tests have been used to estimate a guess to start: the Nu correlation (4.12) for natural convection for vertical isothermal plates can be used to evaluate the heat transfer coefficient h_0. Then, the simulation has been performed and the temperature map of the external surface of the irradiated side has been used to start again the calculation: at this step, it is expected to have an higher heat transfer coefficient h_1 because the external surface is higher with respect to the thermocouple outputs. This iteration ends when h_n and h_{n+1} are close enough. The resulting heat transfer coefficient are reported in Table 4.1. As expected, the higher the peak heat flux level, the higher the heat transfer coefficient from the empirical correlation.

Sample	Heat Flux Level	h [W/m^2/K]	TEST ID
IS	Low	10	IS3
	Medium	15	IS4
	High	18	IS5

Table 4.1: Heat transfer coefficients for natural convection, for each peak flux level.

Definitely, the thermal driver imposed on the irradiated surface on STAR-CCM+ is defined as follows:

$$\alpha \cdot \varphi \cdot A_{irr} - \Phi_{nconv} - \epsilon \cdot \sigma \cdot A_{irr} \cdot (T_s^4 - T_{amb}^4) \quad [W], \tag{4.17}$$

where α is the absorption coefficient, A_{irr} is the surface area of the irradiated side, Φ_{nconv} is defined in 4.18, ϵ is the emissivity, σ is the Stefan-Boltzmann constant and T_s is the local surface temperature computed in STAR-CCM+. The comparison between experimental and numerical results are shown below.

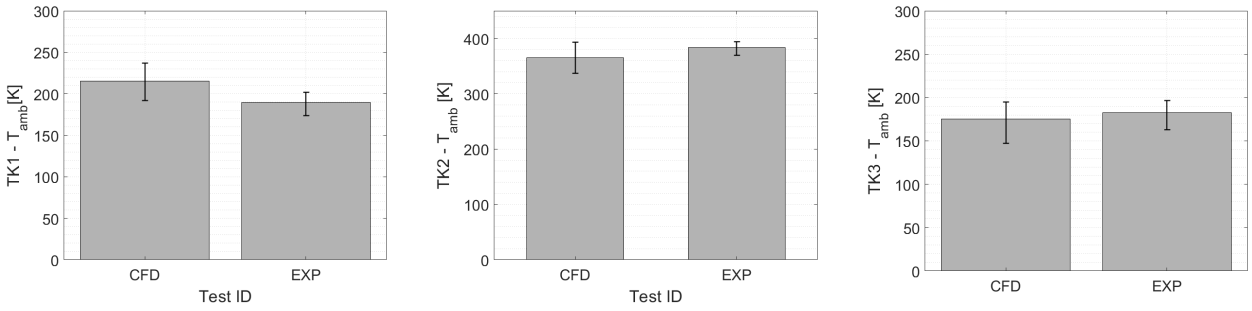

Figure 4.23: Calibration results on IS4 test: temperature comparisons.

4.2.3 Results

Once the CFD model is calibrated, it is possible to validate it with respect to the tests IS3 and IS5. The results are presented below. The value measured by the thermocouple TK2 in the IS3 test is not fully reliable; in fact, it is higher than the TK2 value measured in the IS2 test, which was performed with a reduced mass flow rate and with a higher heat flux, while TK1 and TK3 are correctly lower in the IS3 than in the IS2 test.

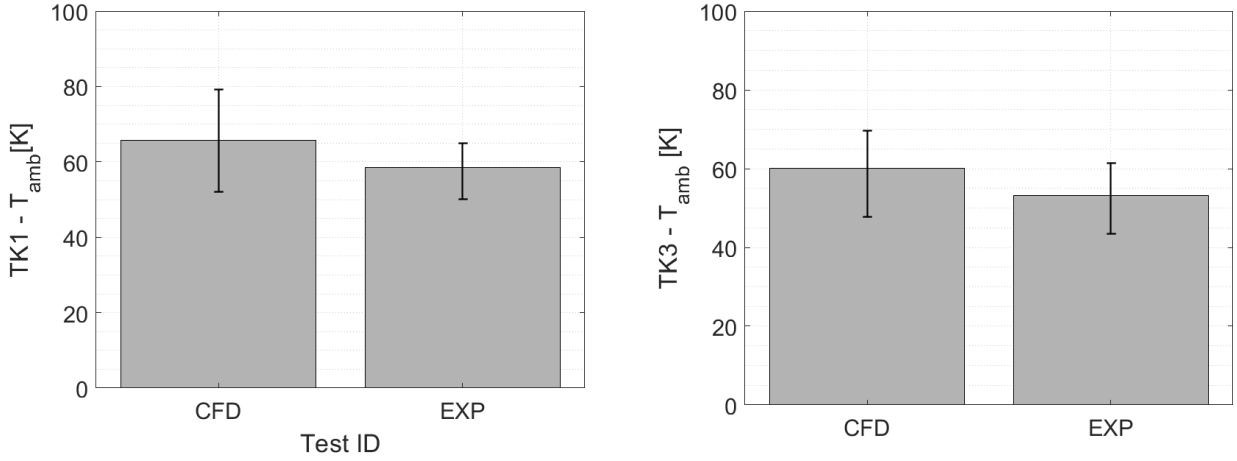

Figure 4.24: Validation on test IS3.

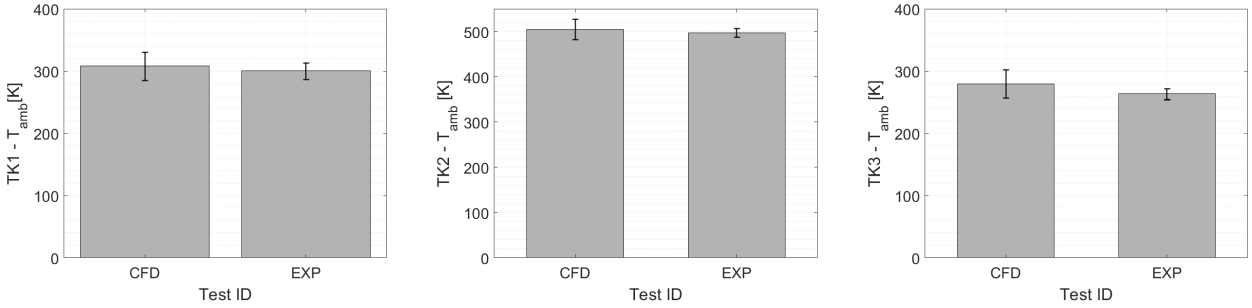

Figure 4.25: Validation on test IS5.

The temperature map of the solid region and, in particular, of the irradiated side is expected to follow the thermal driver. So, the hot spot will be in the region were the peak heat flux is not reduced by curvature or by the Gaussian distribution. An example of the temperature map is proposed in Figure 4.26.

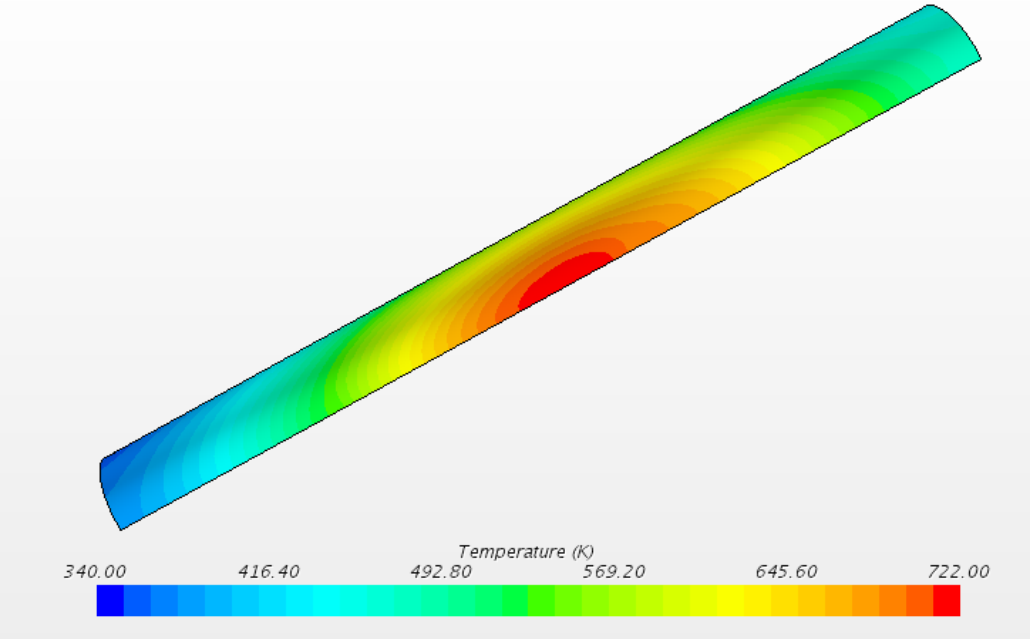

Figure 4.26: Temperature map, irradiated side, IS4.

4.2.4 Error bar analysis

The analysis of the error bars is fundamental both for the experimental and the numerical works. The error bar related to the experimental results includes:

- The error of the thermocouples ($\pm 1.5K$, see Section 2.3.1);
- The error related to the uncertainties about the "quasi" steady state test (see Section 3.1).

For example, taking into account the Figure 2.18, the TK1 is not exactly at steady state, so an interval is taken into account, as shown in Table 4.2.

TEST ID	Heat Flux Level	TK1 mean [K]	TK1 max [K]	TK1 min [K]
AH1	Low	361.3	365.3	354.6

Table 4.2: Example of temperature interval for experimental error bar.

The CFD error bar involves a more expensive reasoning. On the one hand, the computational model has its own error: it can be evaluated as a relative error with respect to the best mesh or, in a more accurate way, through the Richardson extrapolation or the Grid Convergence Index (GCI). Here, the GCI has been evaluated by means of the approach proposed by Celik [37]: the resulting GCI is $\approx 1.5\%$. On the other hand, both the radiometer and the flow meter errors must be taken into account: different simulations were performed, in order to cover all the possible combinations of power and air flow rate. In particular, assuming that the two errors are independent, the maximum of the error bar is obtained through the maximum peak heat flux and minimum air flow rate, while for the minimum is the contrary. In addition, the CFD error bar must include also the maximum and minimum temperature of the sensible part of the thermocouple (in the model).
Please note that, due to the explained differences between the two error bars, it is expected to have higher errors for the CFD results and increasing bars when the heat flux level increases (because of the $\pm 3\%$ of the radiometer, which weights more).

4.2.5 Sensitivity Analysis

The samples were manufactured by means of additive manufacturing, but in the CFD model the internal surface of the tube has been considered to be perfectly smooth (no roughness). Now the question is: how do the results change if a certain surface roughness is set in the CFD model? The Moody diagram [38] has been taken as reference to start looking for relative roughness setting: the lowest values from the chart were simulated, $\epsilon/D = 0.00001$ to $\epsilon/D = 0.001$. The sensitivity analysis has been carried out and no significant variations in the temperatures TK1, TK2 and TK3 have been observed, but just an increasing pressure drop between inlet and outlet sections (as expected, but no pure hydraulic tests were performed at the PSA, so it's not possible to make comparisons). Please note that the maximum roughness height has been selected in order to ensure that it was higher than the first prism layer of the mesh, so that it could have influence on the thermal boundary layer.

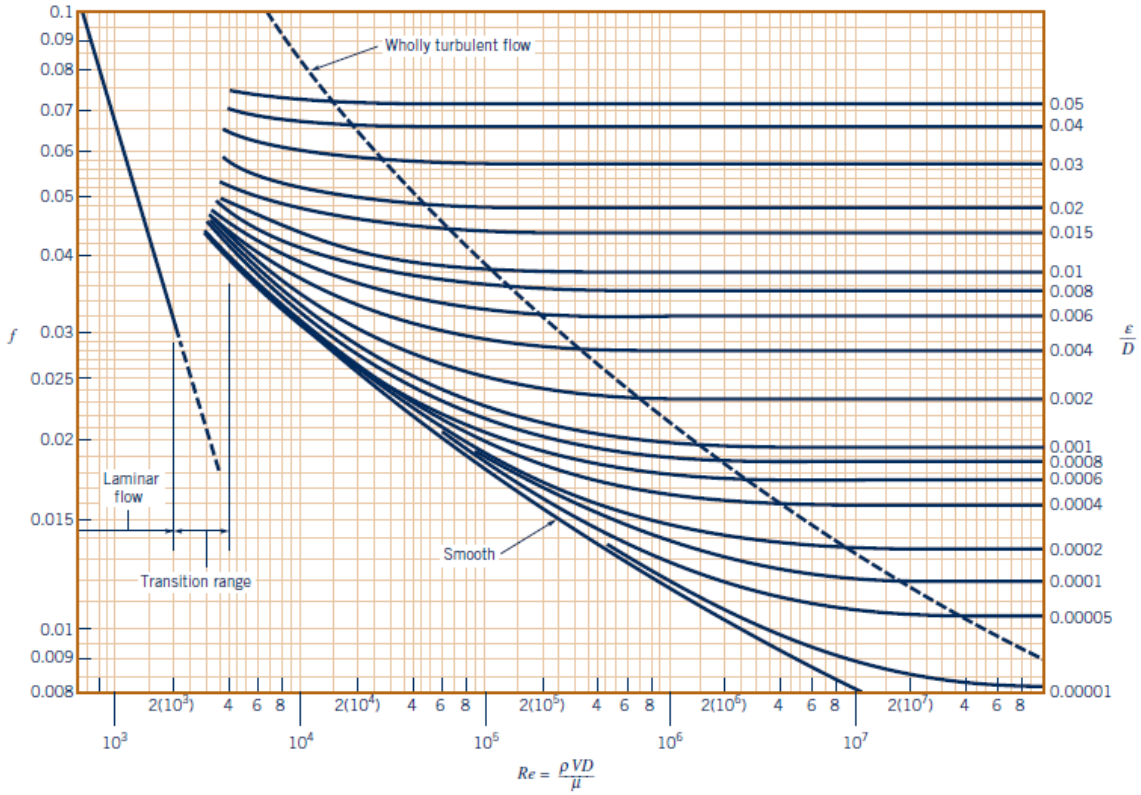

Figure 4.27: Moody chart [38].

4.2.6 Oxidation trend

The samples were manufactured by means of additive manufacturing, but no surface coating was applied to that. This means that high concentrated heat flux can alter the wall surface properties by oxidizing it. So, the question is: is it possible to build up the absorption factor trend through time during the two weeks of experimental campaign? First, it was necessary to collect all the expositions of the tube, i.e. all the tests performed (quasi steady state and transients, good or bad) with their respective times. This result is shown in Table 4.3. Please note that the test ID is highlighted just for the good tests already mentioned in the previous sections and that T stands for transient and SS for steady state. Furthermore, the transient tests have been grouped to make the table more compact: it means that the cycles with the same exposure power have been grouped and the time summed up.

Secondly, the absorptivity has been calibrated for all the tests, from IS1 to IS5 and the peak has been plotted as a function of the irradiated energy (Figure 4.28). As expected, as the exposure time

Test ID	Heat Flux [kW/mq]	Time [s]	Irradiated energy [Wh]	Description
-	52	660	12.8	SS
IS1	180	720	32.9	SS
-	370	480	67.6	T
-	380	450	65	T
-	430	360	58.8	T
-	500	360	68.5	T
-	560	450	95.8	T
-	620	360	84.9	T
-	550	300	62.8	T
IS2	63	660	15.8	SS
-	185	600	42.5	SS
-	330	780	97.9	SS
IS3	55	600	11.7	SS
IS4	178	660	44.1	SS
IS5	267	600	63.9	SS

Table 4.3: Expositions to Sun of the IS tube.

increases, the absorption factor increases due to oxidation. As no similar works exist in literature, the simplest fitting trend was the linear one: the trend line is represented by

$$\alpha_{peak} = 4.0 \cdot 10^{-4} \cdot E + 0.4718 \quad [-], \tag{4.18}$$

where E is the irradiated energy on the x-axis. Please note that this energy in [Wh] has been obtained from the peak heat flux and its Gaussian distribution. Then, it has been multiplied by the irradiated external surface area of the sample (see parameters from Figure 2.1).

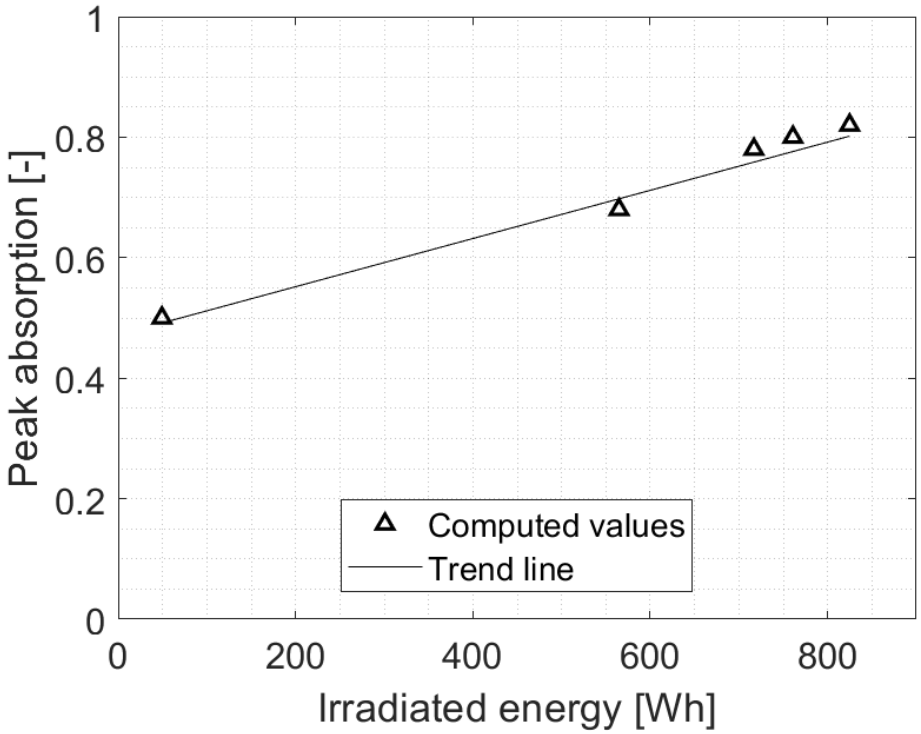

Figure 4.28: IS peak absorptivity trend.

4.2.7 Air temperature profile

In Section 3.2.4 it has been observed that something strange happened in the air outlet temperature measurements and it has been concluded that not only the measured temperature TK5 is a near wall temperature, but in the case of the smooth tube, the thermocouple was positioned closer the wall. This result make invalid or, at least, useless the TK5 outputs.
So, once the model has been validated, it is possible to check what happens to the air outlet temperature in the IS tube. The plot shown in Figure 4.29 represents the radial air outlet temperature profile, starting from the center (so, it is half of the profile): as concluded screening the data collected at the PSA, it is clear that the measured air temperature (in red) is a near wall temperature, which is very far from the bulk temperature, that is the one which can be useful to make energy balances or calorimetry. The temperature profile refers to the IS4 test.

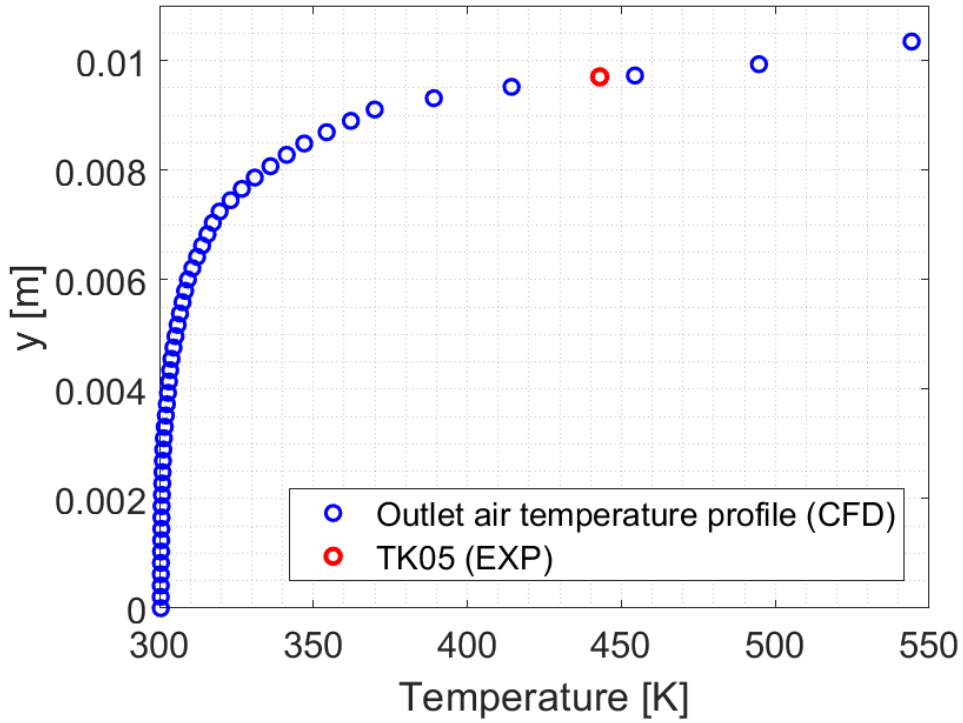

Figure 4.29: Radial air outlet temperature profile, IS4.

4.2.8 Sieder-Tate correlation

Since the analysis of turbulent flow conditions is a good deal more involved, greater emphasis is placed on determining empirical correlations. For fully developed (hydrodynamically and thermally) turbulent flow in a smooth circular tube, the local Nusselt number may be obtained from the *Sieder-Tate* correlation [32]:

$$Nu_D = 0.027 Re_D^{4/5} Pr^{1/3} \left(\frac{\mu}{\mu_s}\right)^{0.14}, \tag{4.19}$$

where

$$Re_D = \frac{\rho v D}{\mu} \approx 2.4 \cdot 10^4 \tag{4.20}$$

$$Pr = \frac{\mu c_p}{k} \approx 0.7 \tag{4.21}$$

This correlation is recommended [32] for flows characterized by large property variations and has some constraints, which are all satisfied: $Re_D \geq 10000, 0.7 \leq Pr \leq 16.700$ and $\frac{L}{D} \geq 10$. The ST correlation is thought for circular tubes subject to uniform heat flux, which is not exactly the current case. In fact, the samples at the PSA were irradiated just on one half of the wall surface and, in addition, the distribution of the heat flux was not uniform but followed a Gaussian distribution. As no similar works have been found in literature, it is the first time that the correlation 4.19 is applied to such a case. The way to perform this comparison is the following: first, the properties of the air at the inlet and at the outlet are used to calculate the average Nusselt number from equation 4.19. Then, the CFD average Nusselt number has been extrapolated from the numerical model on STAR-CCM+, computing the wall temperature, the bulk temperature and the average heat flux applied at different planes along z-axis. So, the heat transfer coefficient is defined as follows [39]:

$$HTC = \frac{WallHeatFlux}{(T_{wall} - T_{bulk})} \quad [\frac{W}{m^2K}] \tag{4.22}$$

The result is presented in Figure 4.30, where CFD and correlation are in agreement. For the numerical evaluation, a plan independence study is performed to ensure that the average Nusselt number does not change with the number of plans taken into account in the STAR-CCM+ ambient.

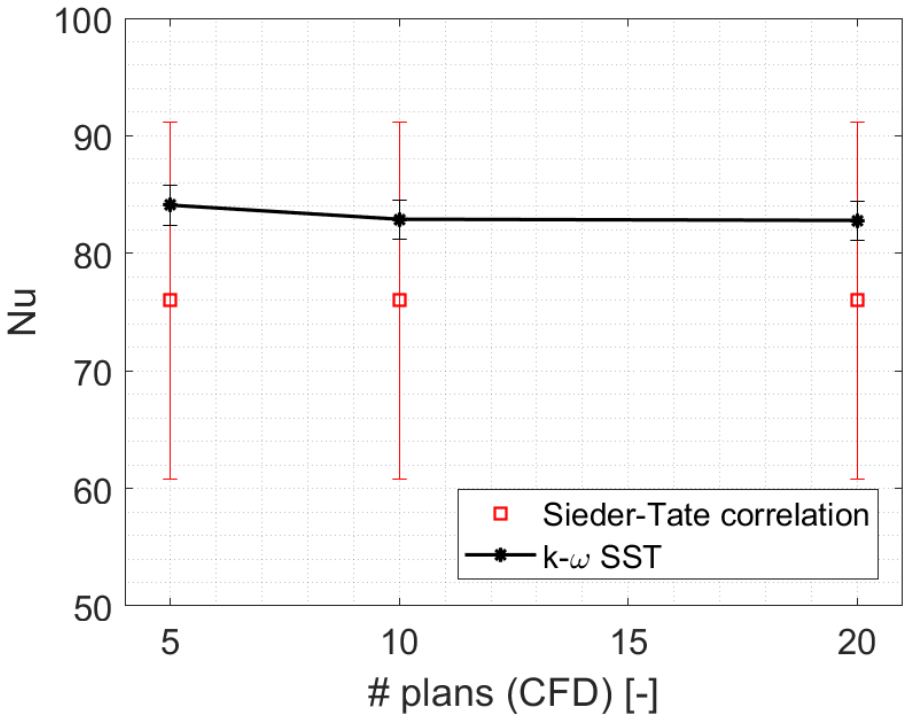

Figure 4.30: Sieder-Tate applied to Inconel Smooth tube.

4.3 Inconel Helices (IH) receiver

The second 3D CFD model refers to the Inconel tube equipped with helical ribs (IH). Instead of the previous case, here the nuts have been included in the CAD to have a more realistic model. The domain is shown in Figure 4.32. The pitch, width and height of the ribs were designed to maximize the heat transfer coefficient on the base of a preliminary CFD study. The helical-ribbed tube consists of three starts with pitch 22.5 mm and height of the ribs 2 mm. The three thermocouples are also inserted in the computational domain (see Figure 4.31).

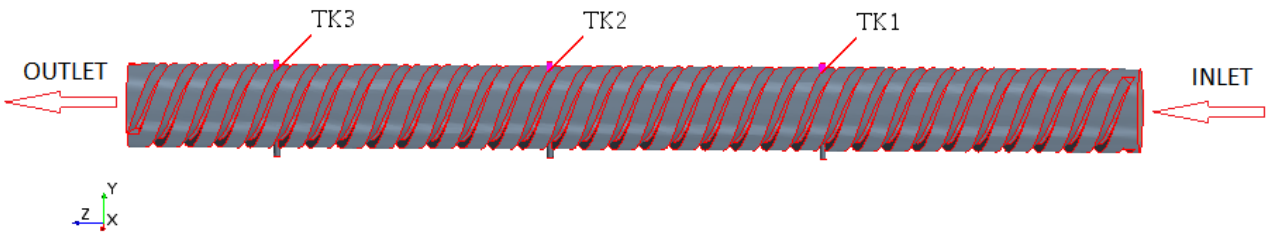

Figure 4.31: IH air volume and thermocouple insertion.

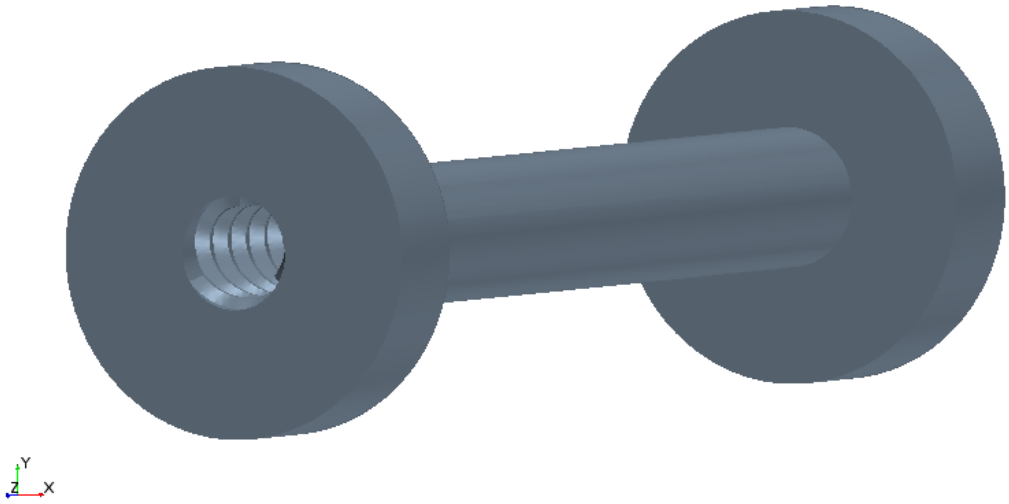

Figure 4.32: IH computational domain.

4.3.1 Mesh Generation and Grid independence

The discretization of the domain has been done according to the main turbulent phenomenon and to ensure a good compromise between computational cost and accuracy of the results. The flow regime is turbulent ($Re = 2.4 \cdot 10^4$ at the inlet section) and the mesh consists of polyhedral cells with 10 prism layers at the solid/fluid interfaces ($y+ \approx 1$, as the Prandtl number for the air is ≈ 1 in all the tested thermal-hydraulic conditions). Through appropriate surface control, the size of the grid has been imposed to decrease as it approaches the walls, as higher and rapid variations of the main physical parameters are expected to occur there. An automated surface repair function is also included to automatically correct errors made by the software while generating the mesh. A structured prism layer is set at the wall, to highlight the behavior of the flow in the viscous sub-layer;hence, y+ at the wall is verified to be ≈ 1, as shown in Figure 4.33.

The quality of the mesh has been ensured both through the Skewness angle and the Bad Cell indicators. In Figure 4.34, the Bad Cell Indicator is shown, as that region represents the most critical one: the quality of that cells is satisfactory, as just 0.005 $\%$ of the cell has a bad quality (BCI = 1) and no warnings or convergence issues appeared. The quality of the mesh was checked also for the solid regions, both the pipe and the thermocouples.

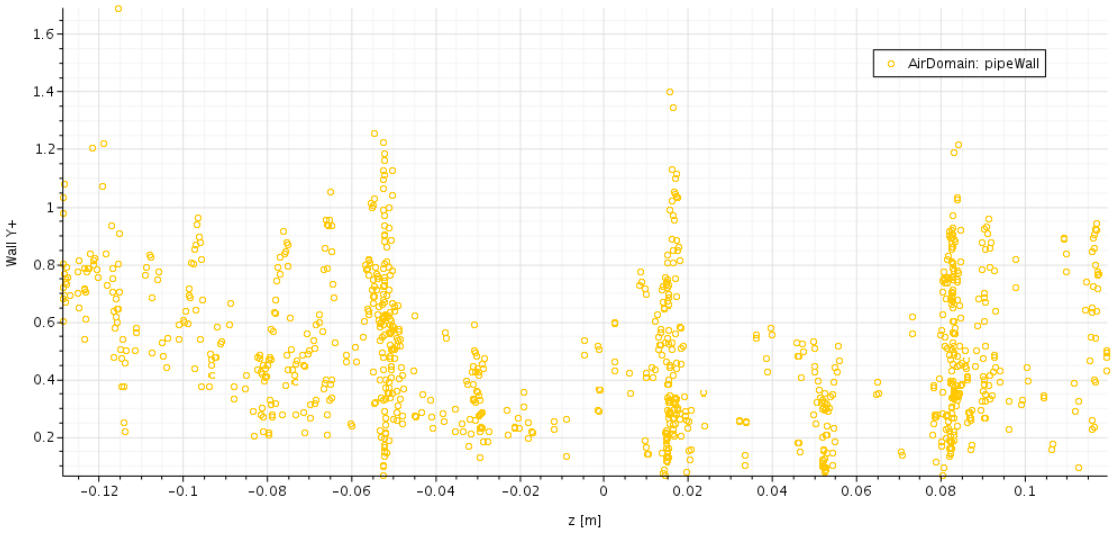

Figure 4.33: Check on the wall y+.

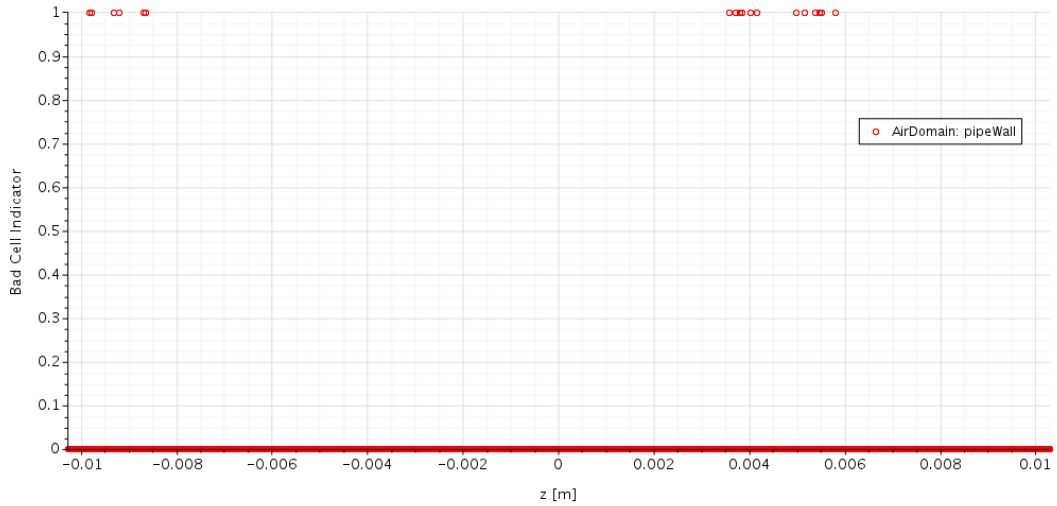

Figure 4.34: Bad Cell Indicator: air domain.

Once the grid was generated, the space convergence study has been carried out to ensure that numerical results were independent of both the polygonal mesh, and the prism layer resolution: the grid independence study, as the calibration, have been performed on the test IH4. Mean outlet velocity,temperature TK3, as well as the total pressure drop have been evaluated, to show that they converge with a monotonic trend, increasing the total number of cells. The grid independence study in the core region has been achieved by changing the base size of the polygonal cells, while keeping the number of prisms fixed, and making sure that the outer prisms had similar dimensions with the above neighboring cells, to enhance the information exchange between the two regions. The total numbers of cells for the analyzed grids are approximately $0.5 \cdot 10^6$, 10^6 and $1.5 \cdot 10^6$, with 10 prisms (see Figure 4.35 and Figure 4.36).

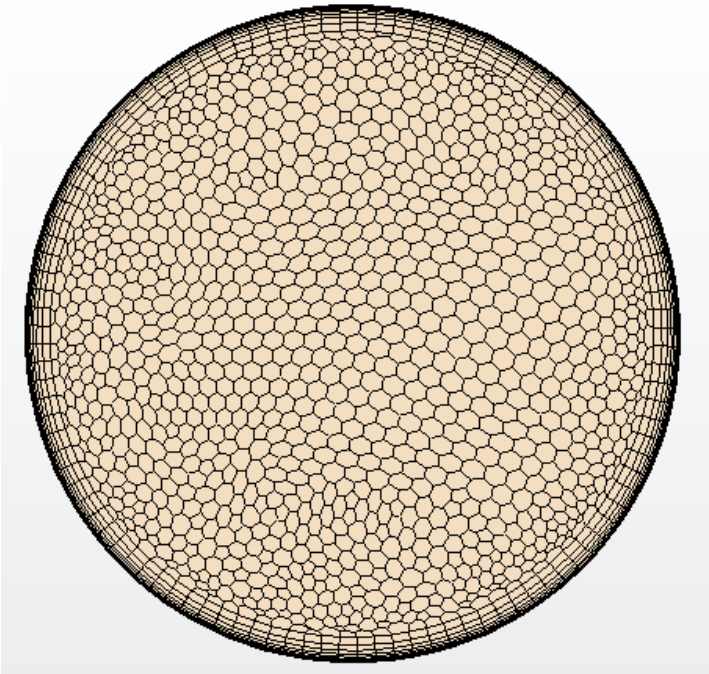

Figure 4.35: Air outlet section: mesh generated.

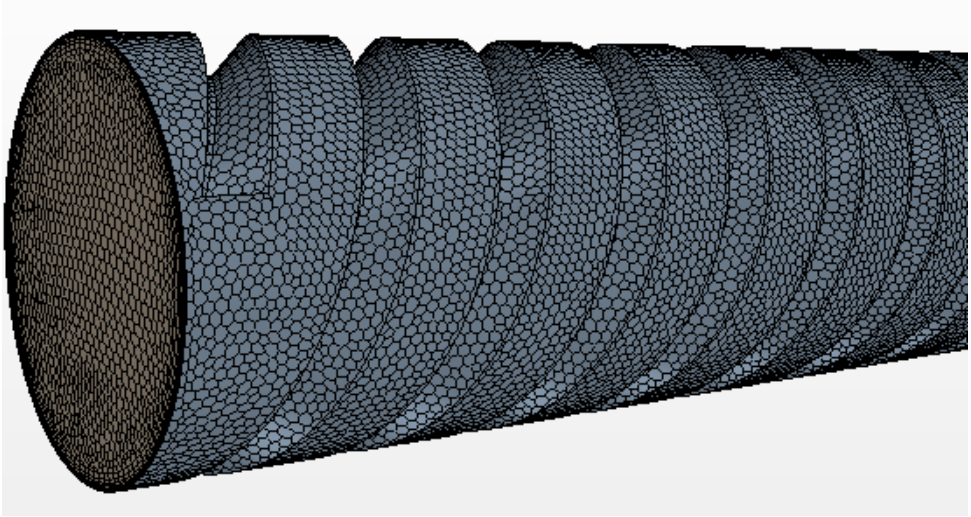

Figure 4.36: Air core flow: mesh generated.

The grid independence study has been performed (Figure 4.38 and Figure) both in terms of number of cells and number of prisms layer and the final selected mesh is made of approximately one million cells and 10 prisms layers.

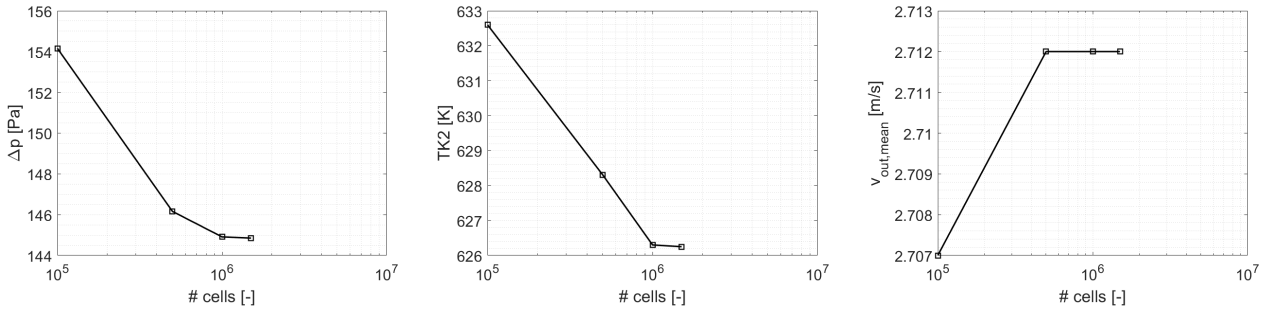

Figure 4.37: Convergence study in terms of total number of cells.

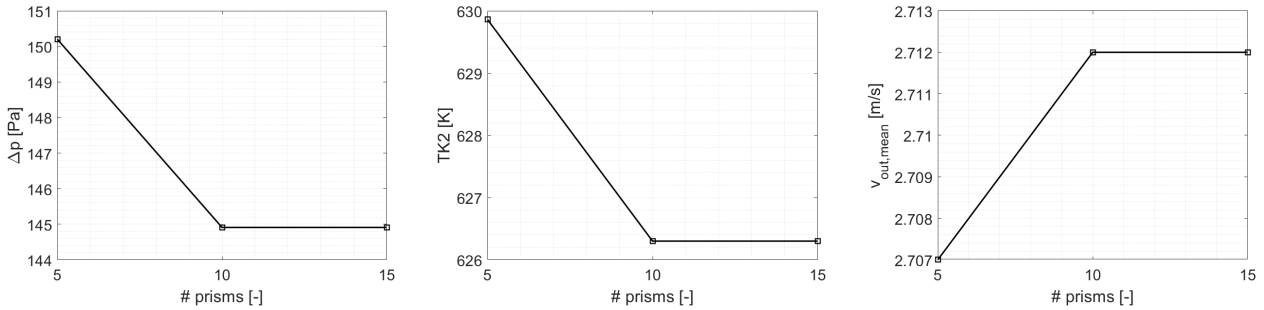

Figure 4.38: Convergence study in terms of total number of prism layers.

4.3.2 Calibration

The emissivity and the absorptivity are not known a priori and it is necessary to calibrate the two to make possible the validation. The procedure is the same explained in Section 4.3.2, but for the IH tube the two parameters have been calibrated independently to have a more accurate solution, even if its computational cost has been higher.
The selected test for the calibration is the IH4, which was performed on September 25^{th}. The resulting emissivity for the irradiated side of the solid region is shown in Figure 4.39. As expected, as the temperature are relatively lower for the IH tube with respect to the IS tube, also the peak emissivity will be smoothed: in fact, its peak is 0.75, against 0.8 of the smooth tube. Please note that the minimum of the irradiated side and the uniform emissivity of the back side are set equal to 0.3, as already explained before.
The calibration is a fundamental step of the CFD analysis because it allows to calibrate the thermo-hydraulic numerical model on the tests collected at the PSA in the SF60. Once the calibration will be completed, it will be possible to change the input parameters, in this case the peak of the Gaussian function of the incident flux, to simulate the CFD model in the same conditions of the other tests which were considered valid for the current purpose.

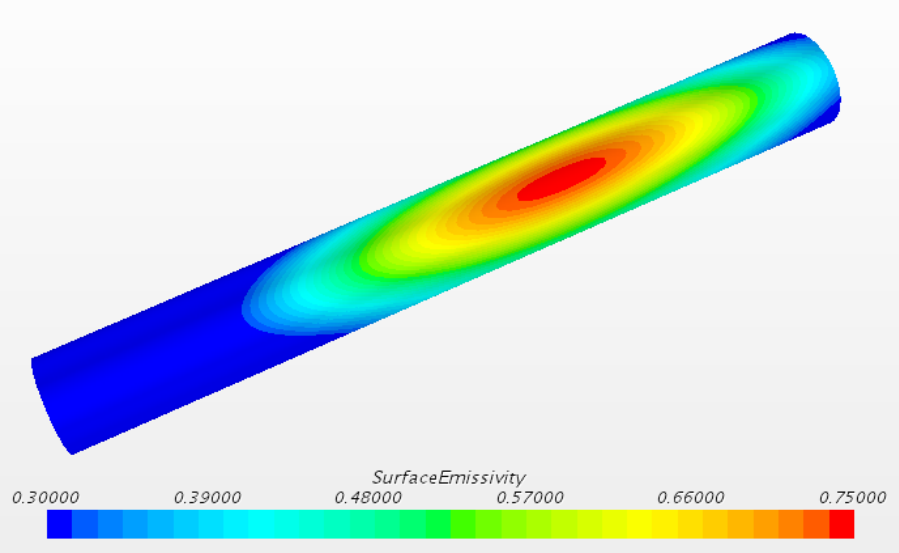

Figure 4.39: Emissivity calibrated on test IH4, irradiated side.

On the other hand, the absorptivity, which has the same Gaussian distribution, is shown in Figure 4.40. For the trend obtained in the plot of Figure 4.28, the minimum has been found to coincide with the very first value of the peak absorptivity, which is 0.5. The back side absorption is not relevant, as no irradiation is imposed on the tube. Note that the position of the peak is different with respect to the IS tube: the samples, still available, are oxidized and it has been possible to reconstruct the position of the focus, which in this case coincide with the position of the thermocouple TK2 (see Figure 4.40).

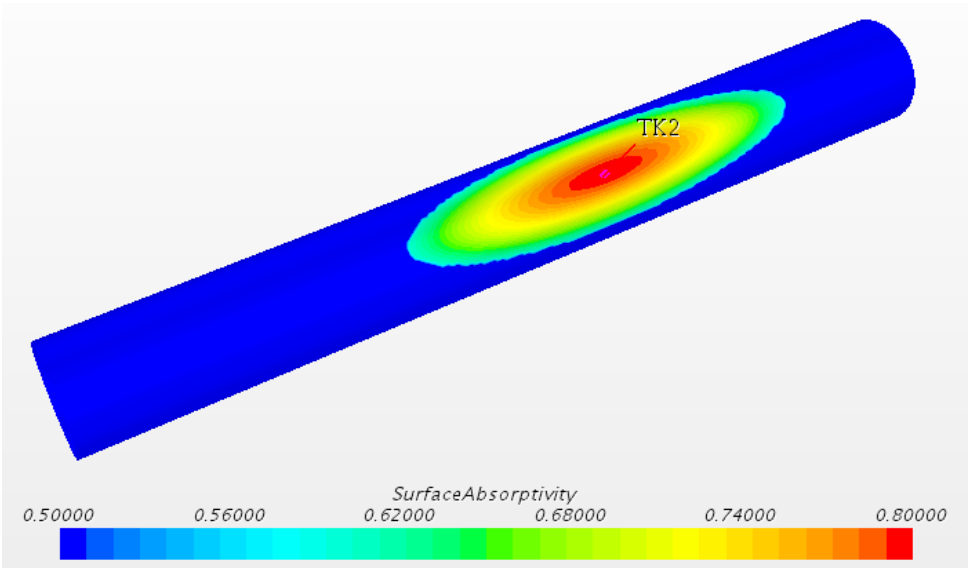

Figure 4.40: Absorptivity calibrated on test IH4, irradiated side.

The very same procedure explained in detail in Section have been performed for the IH CFD model and the resulting heat transfer coefficient for natural convection are presented below:

Definitely, the thermal driver imposed on the irradiated surface on STAR-CCM+ is defined as follows:

$$\alpha \cdot \varphi \cdot A_{irr} - \Phi_{nconv} - \epsilon \cdot \sigma \cdot A_{irr} \cdot (T_s^4 - T_{amb}^4) \quad [W], \tag{4.23}$$

where α is the absorption coefficient, A_{irr} is the surface area of the irradiated side, Φ_{nconv} is defined in 4.18, ϵ is the emissivity, σ is the Stefan-Boltzmann constant and T_s is the local surface temperature

Sample	Heat Flux Level	h [W/m^2/K]	TEST ID
IH	Low	7	IH3
	Medium	10	IH4
	High	12	IH5

Table 4.4: Heat transfer coefficients for natural convection, for each peak flux level.

computed in STAR-CCM+. The comparison between experimental and numerical results are shown below.

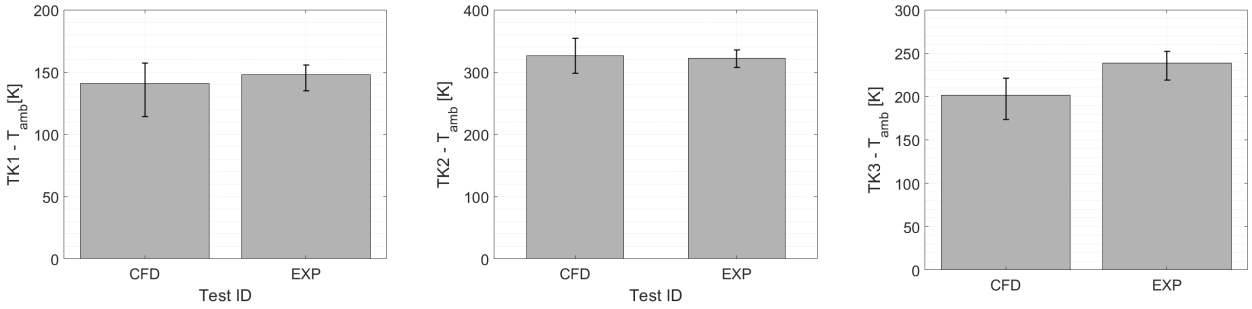

Figure 4.41: Calibration results on test IH4: wall temperatures.

4.3.3 Validation

Once the CFD model is calibrated, it is possible to validate it with respect to the tests IH3 and IH5. The results are presented below.

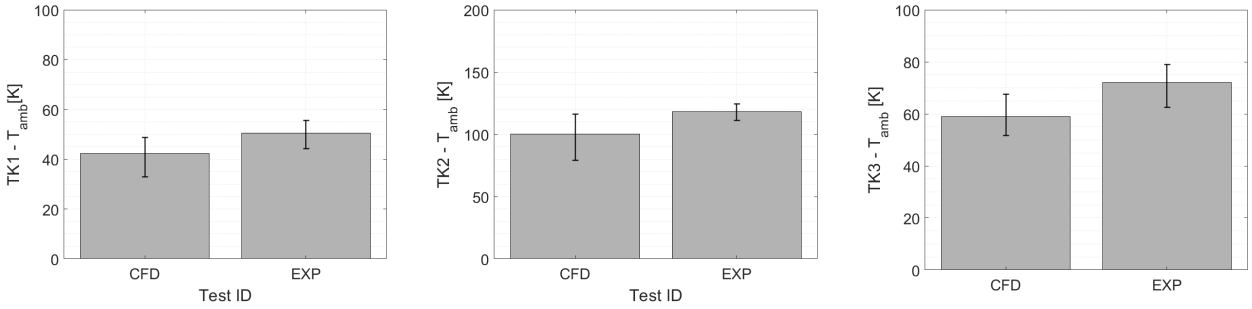

Figure 4.42: Validation on test IH3.

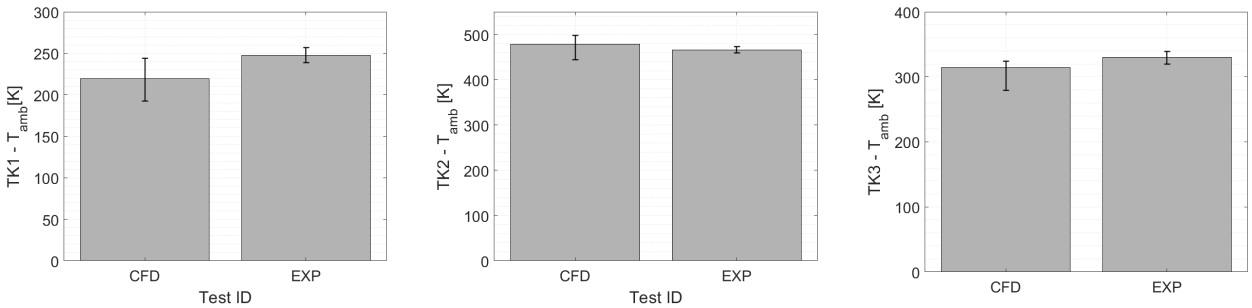

Figure 4.43: Validation on test IH5.

The model appears to be robust in terms of convergence and mesh quality and reliable in terms of thermal-hydraulic behaviour of the component: all the error bar crosses each other, which was in principle the aim of the CFD study.

4.3.4 IH vs IS

The presence of turbulence promoters introduced some additional complexities to both the experimental campaign and the CFD analysis and, furthermore, it requested an higher economic effort to manufacture it. So, it is necessary to deeply investigate its behaviour and to quantify the improvements with respect to the base case, which here is represented by the Inconel Smooth (IS) tube. So, in this section, the most significant results will be presented to justify the choice of turbulence promoters.
In the next tables and plots, the heat flux levels will be described just as low-medium-high, which are the three levels of interest (see Section 3.1) for the current experimental campaign. The reason is that the conditions were almost the same and so all the considerations and the comparisons that will be made will refer to tests performed at the same heat flux level and air mass flow rate.
The very first comparison has been done in Chapter 3 and it has been shown that the inner wall temperatures in the IS tube tests are higher with respect to the IH ones. The CFD analysis, of course, confirms this trend and the temperature maps of the two samples are shown as follows. The temperature maps proposed here refer to the tests IH4 vs IS4 and IH5 vs IS5, which correspond to the medium and high heat flux levels. It is clear that, at equal conditions, the Inconel tube equipped with helices is more efficient from a heat transfer point of view. So, the both the peaks and the average temperatures are blunt. Please note that the lower heat flux level has not been shown as no significant variations can be highlighted, as already seen in the data analysis phase. As expected, as much as the intensity of the thermal driver rises, the differences increases between the two samples.

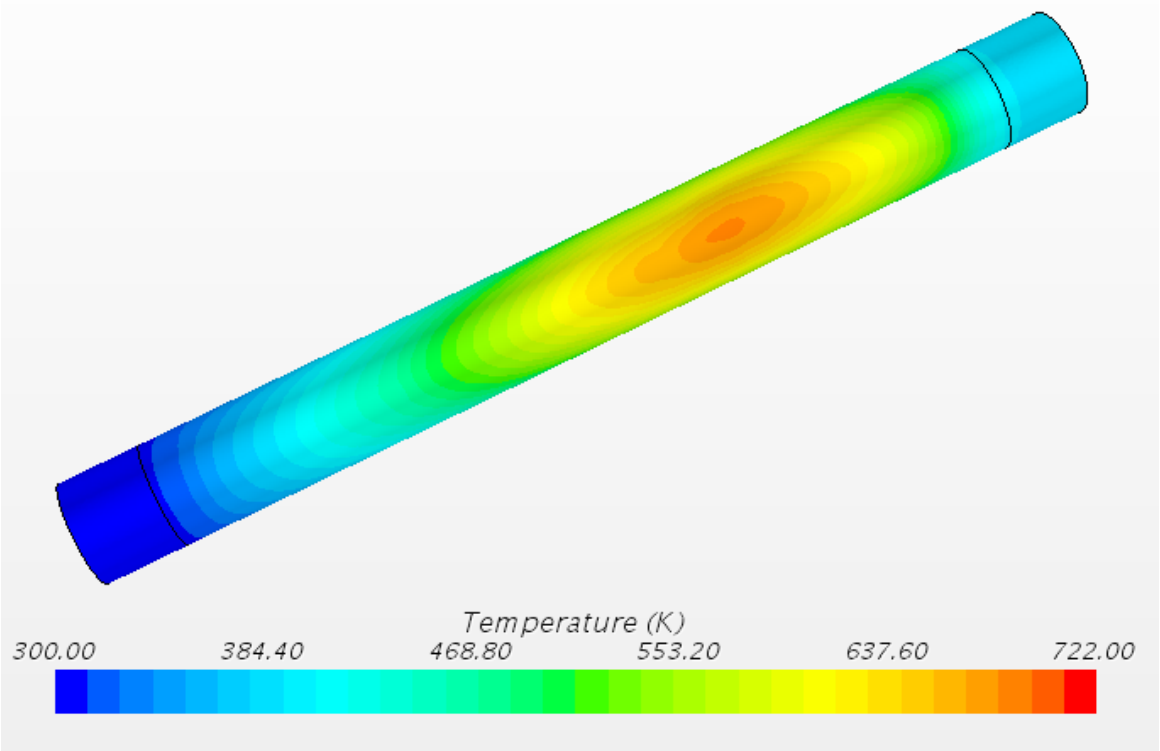

Figure 4.44: Temperature map IH tube, medium flux level (IH4).

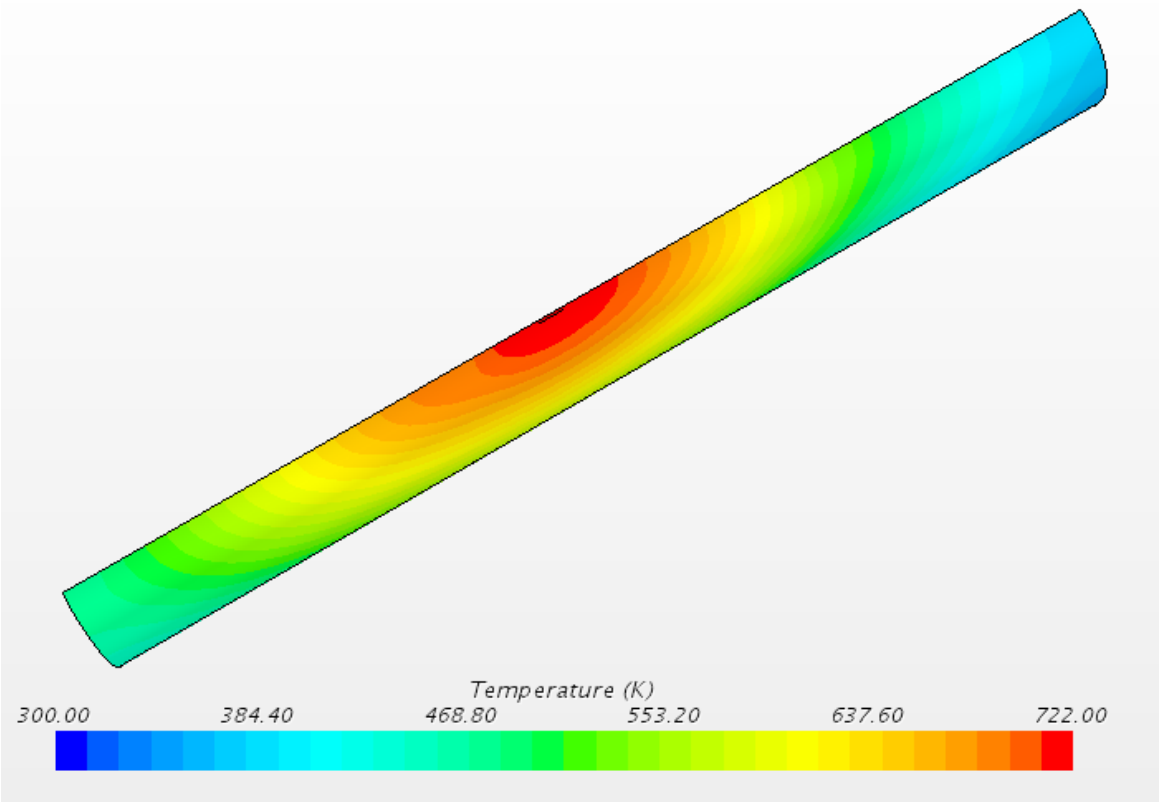

Figure 4.45: Temperature map IS tube, medium flux level (IS4).

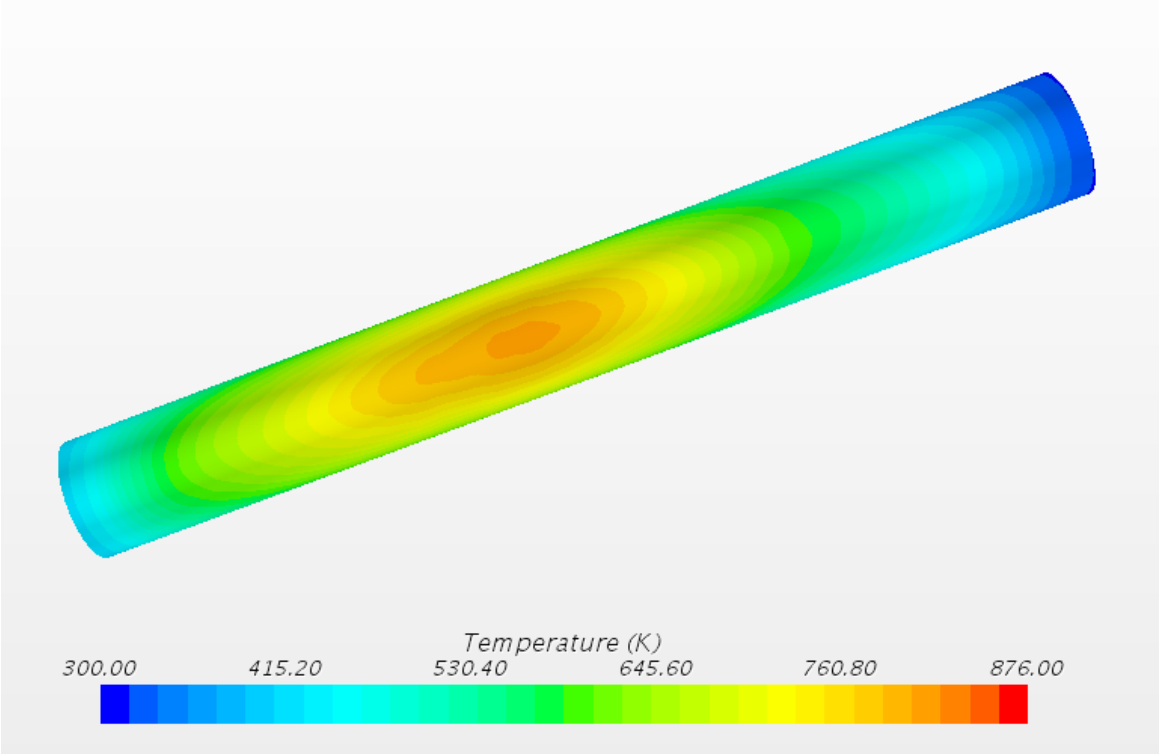

Figure 4.46: Temperature map IH tube, high flux level (IH5).

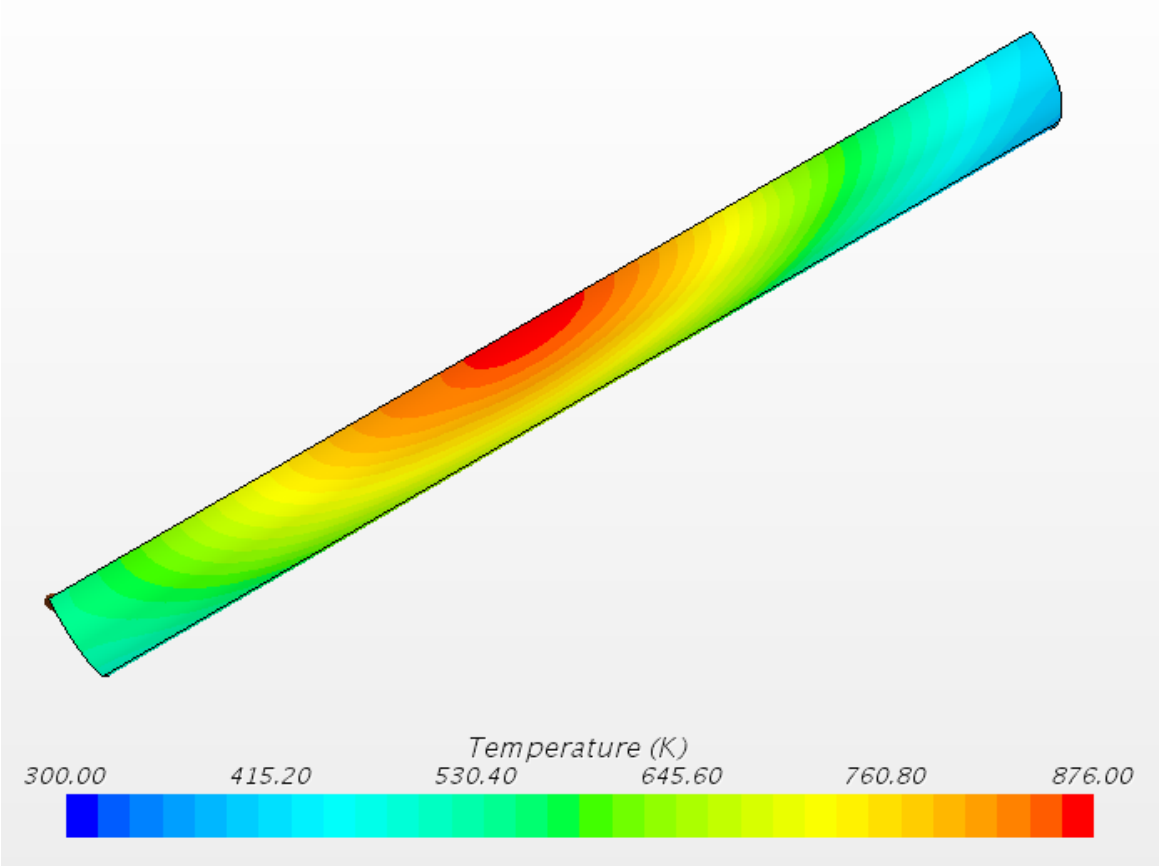

Figure 4.47: Temperature map IS tube, high flux level (IS5).

The following parameters have been also monitored and shown in Table 4.5:

- Tirr is the average temperature of the irradiated side wall;
- Tback is the average temperature of the back side wall, the one which is totally obscured from the solar radiation;
- Tmax is the temperature of the hot spot, so the maximum temperature present in the solid region;
- Convection losses due to natural convection with the ambient temperature;
- Radiation losses due to emissivity at different temperatures.

TUBE	Heat Flux Level	Tirr [K]	Tback [K]	Tmax [K]	Conv loss [%]	Rad loss [%]
IS	Low	381.2	347.8	447.7	17.3	8.0
	Medium	543.2	451.5	722.1	20.4	17.1
	High	641.8	518.1	876.6	23.0	24.2
IH	Low	376.3	348.6	420.3	10.9	7.3
	Medium	525.3	454.3	654.5	12.3	10.6
	High	619.2	529.2	814.8	14.1	15.9

Table 4.5: Resume of the most critical parameters for the thermal characterization of the samples.

The result that comes out is very promising: the average temperature of the irradiated side is lower in the case of the IH tube, while the temperature of the back side is higher in the case of the IH tube. This means that the average temperature difference between the two sides has been smoothed thanks to the equipment of turbulence promoters, which directly imply reducing the thermomechanical stresses. Furthermore, the thermal losses due to convectionradiation are kindly reduced as both depends on the temperature of the solid region (in particular the second ones): this imply a better thermal efficiency for the IH tube, which means that the air bulk temperature is higher, as then the potential output power.
In Figures 4.48, 4.49 and 4.50, the thermal losses and the useful power exchanged to the fluid are reported in terms of power [W] to have an idea of the order of magnitude of the different heat flux levels. As already said, the higher the concentrated solar power, the higher the differences between the two tubes: in Figure 4.50 it is clear the different amount of thermal power gained by the air flow, which is particularly more consistent for the IH sample. The current energy balance neglect the thermal resistance of the wall thickness.

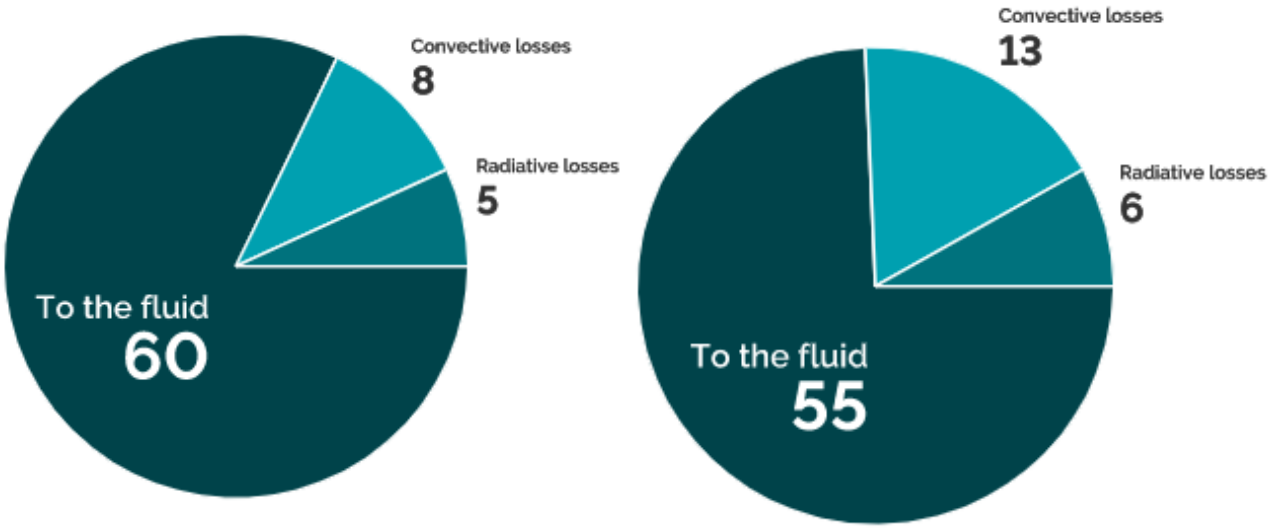

Figure 4.48: IH (left) vs IS (right). Low level heat flux. Values in [W].

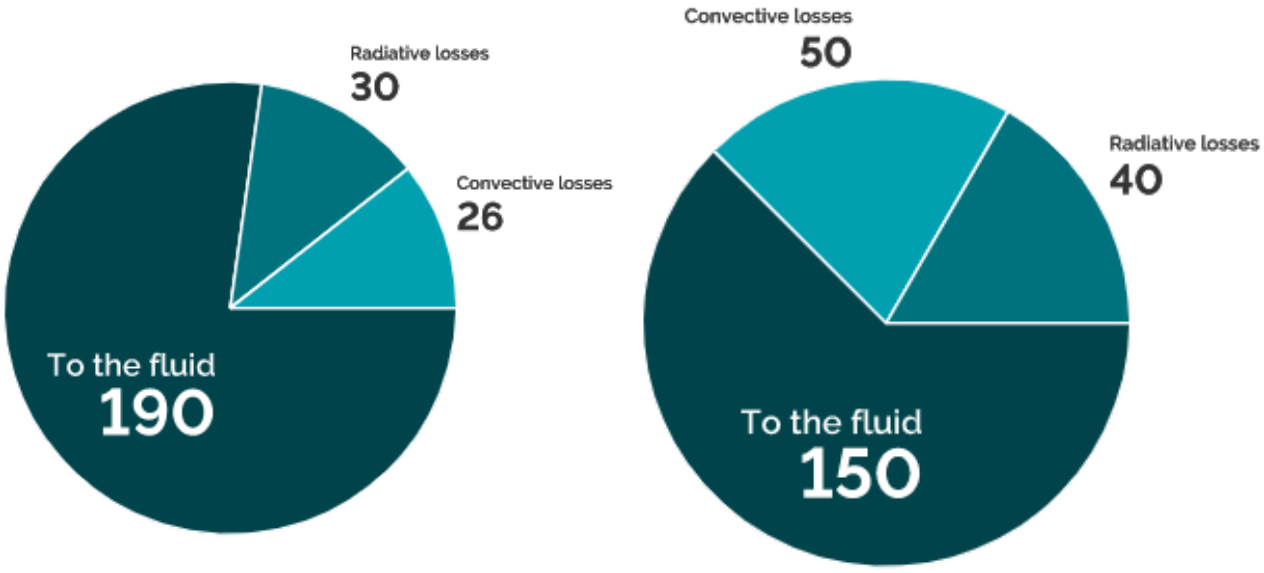

Figure 4.49: IH (left) vs IS (right). Medium level heat flux. Values in [W].

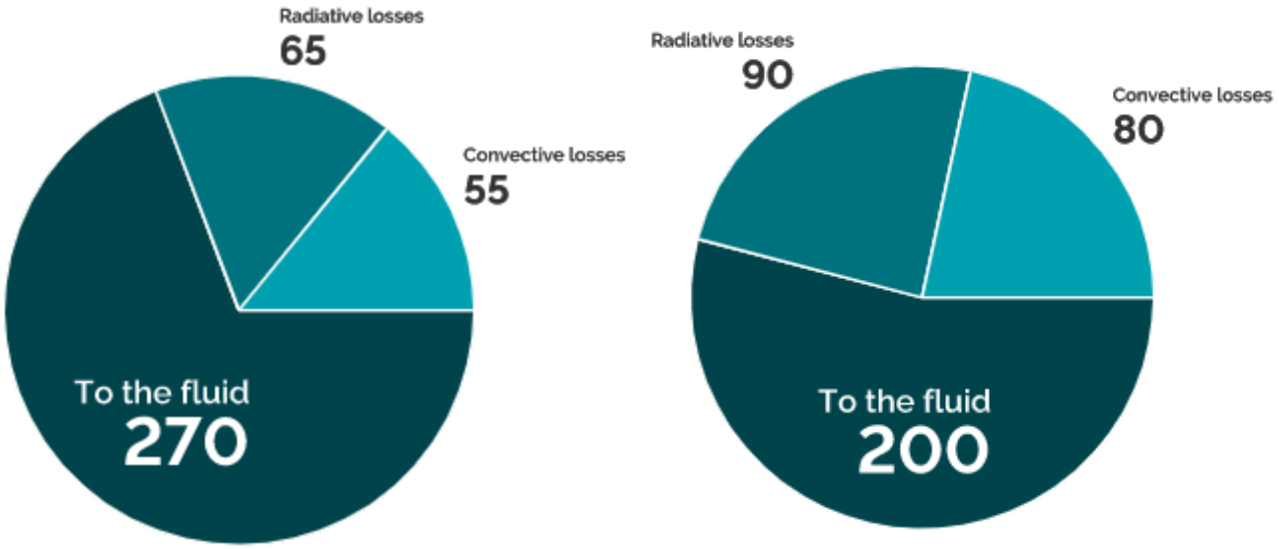

Figure 4.50: IH (left) vs IS (right). High level heat flux. Values in [W].

The aim of the turbulence promoters is to enhance the heat transfer: as the heat losses are lower, it is expected to have a greater bulk temperature of the air at the outlet section. In addition, the flow pattern forced by the helices allows to have a more homogeneous temperature distribution, as shown in Figure 4.51. In Figure 4.52 it is shown the air temperature profile of the IS tube at the outlet section: in opposition with the IH tube, the thermal gradient along the radial is very strong and the core of the air flow appears to be at the inlet temperature. So, the two profiles differ for:

- Radial thermal gradients;
- Maximum and minimum of the range: the temperature distribution is more homogeneous in the IH tube.

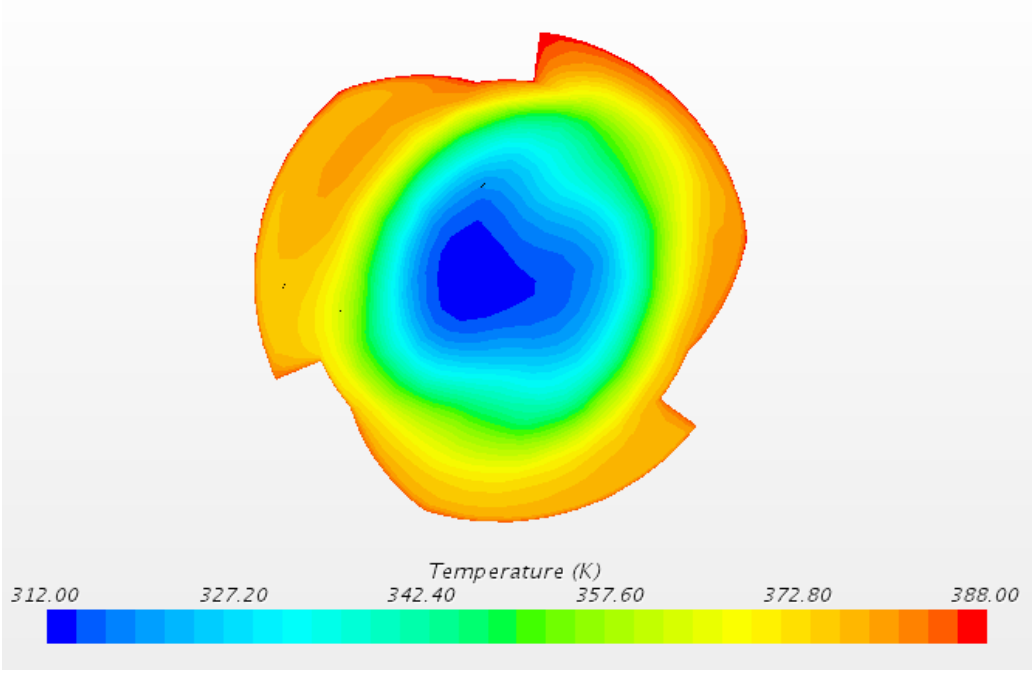

Figure 4.51: Air temperature profile at the outlet section, test IH4.

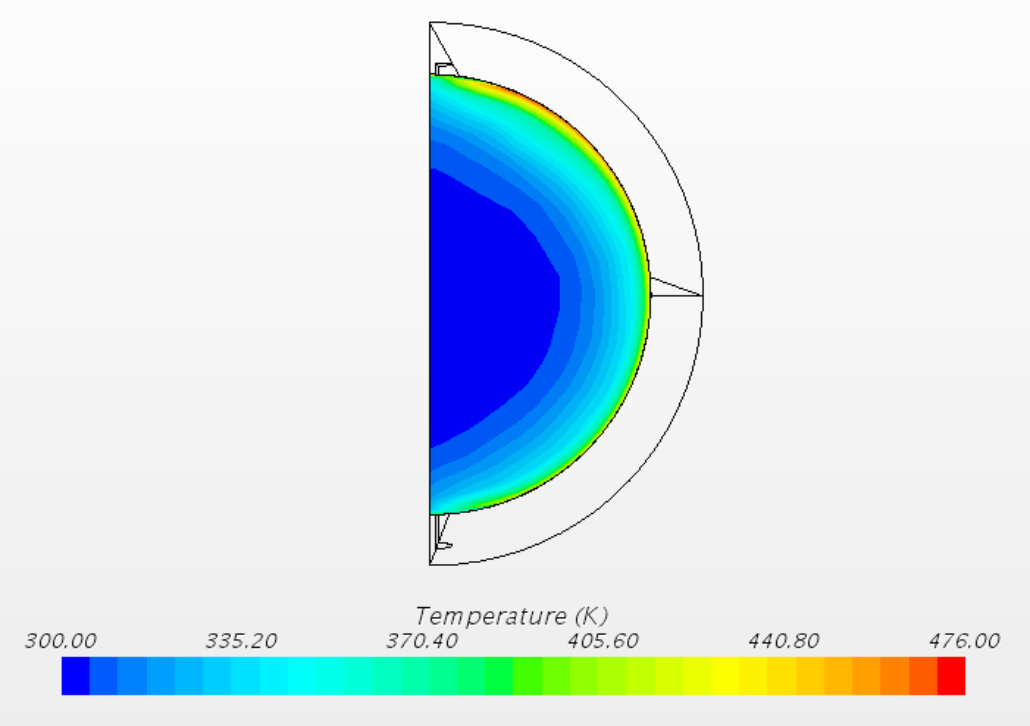

Figure 4.52: Air temperature profile at the outlet section, test IS4.

The main improvements highlighted by now are the following:

1. The temperature difference between the irradiated and the back sides of the is lower in the case of the IH tube It implies the reduction of the thermal stresses;

2. The thermal losses are more significant in the IS tube model: this implies that the thermal power transferred to the fluid is lower. So, the outler air temperature is higher when the turbulence promoters are present.

The two above-mentioned achievements can be both explained looking at the streamlines of the IH numerical model on STAR-CCM+. The streamlines are a family of curves that are instantaneously tangent to the velocity vector of the flow, showing the direction in which a mass-less fluid element will travel at any point in time. First, the flow is clearly turbulent and it can be observed that the path of the fluid follows the geometry and the design of the internal helices. In particular, as it is shown in Figure 4.53, where the streamlines are associated to the temperature scalar field, the fluid particles attached to the internal wall round along the circumference promoting the mixing of the fluid: so, the heat removed from the irradiated side is distributed down, enhancing the heat transfer to the back side of the tube wall. A zoom of the region close to the outlet section is shown in Figure 4.54 to better visualize the streamlines whose temperature rises up in the upper region (where the thermal driver is applied), to then release heat to the lower solid region.

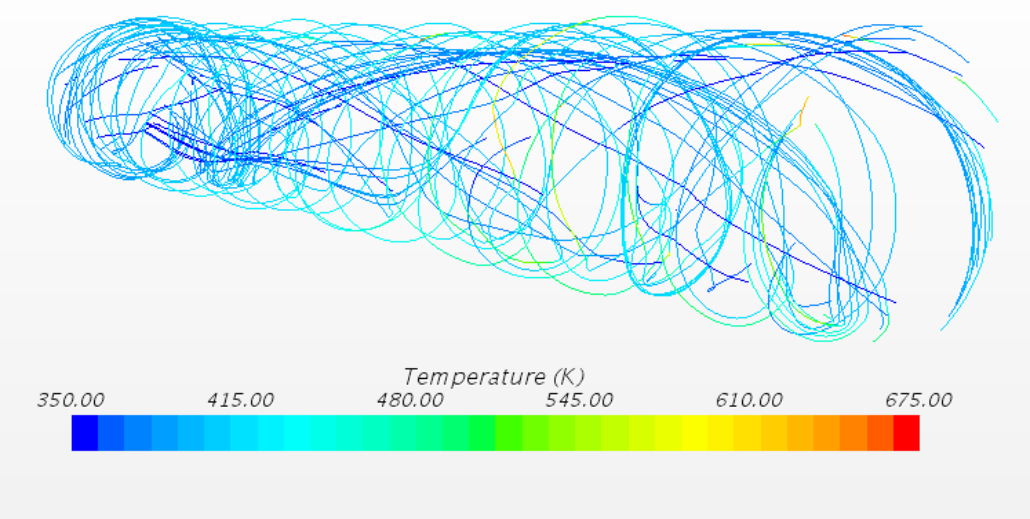

Figure 4.53: Streamlines associated to the temperature field, IH tube.

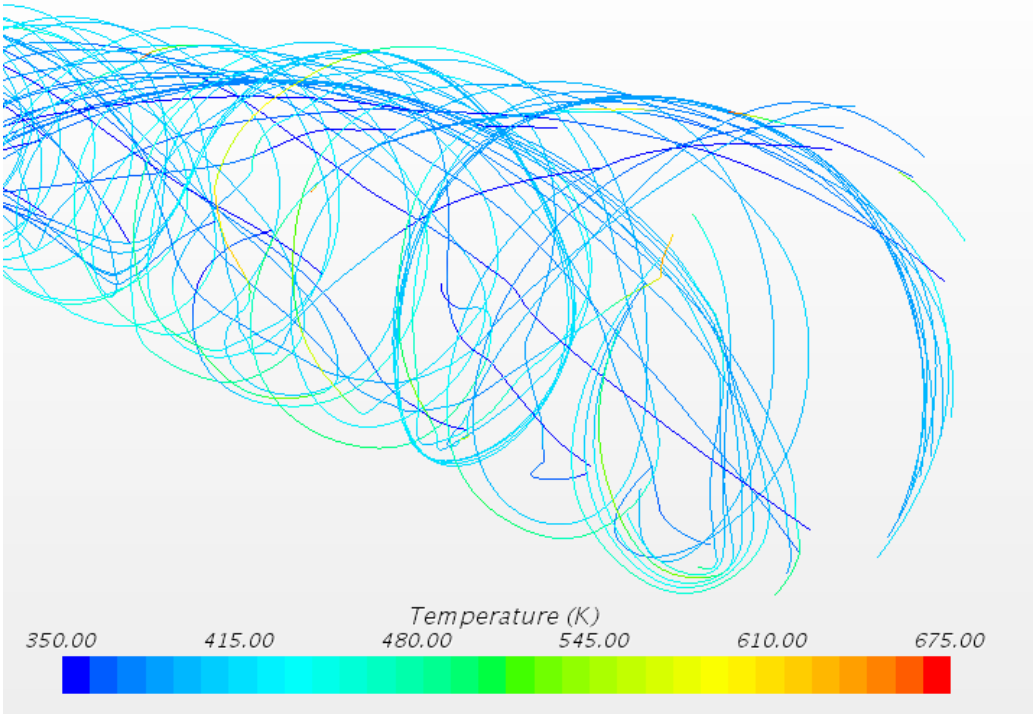

Figure 4.54: Streamlines associated to the temperature field, IH tube.

One of the most interesting aspect of the current project is that in literature no similar works are present. So, to deeply characterize the IH tube from a thermal and hydraulic point of view, some additional considerations have been carried out. First, as already done for the smooth Inconel tube, it has been compared the CFD model Nusselt number with the one forecast by the Sieder-Tate empirical correlation (equation 4.19). It is not expected to have a good match as in the current case the heat flux is not uniform, nor applied to all the external surface and, in addition, the pipe is not smooth. So, the aim of this analysis is to carry out a correction factor that can be useful in the design phase [39]. The result is shown in Figure 4.55: as expected, the Nusselt number that comes out from the Sieder-Tate correlation underestimates the value and a correction factor of approximately 1.3 should be necessary.

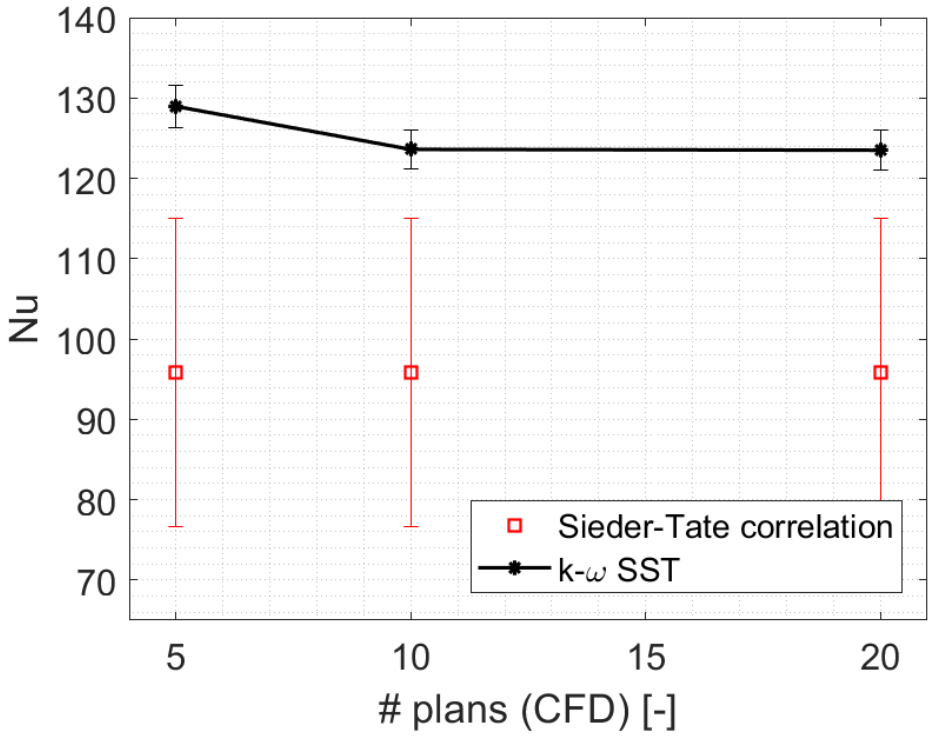

Figure 4.55: Sieder-Tate applied to Inconel Smooth tube equipped with helices.

The thermal behaviour of the IH tube has been evidenced to be kindly better with respect to the IS one. By the way, it is necessary to consider a second aspect which could be critical: the pressure losses. As expected and as it can be noticed from the mesh independence studies, the pressure drop increases with the equipment of turbulators. The difference is about one order of magnitude due to, for example, the higher velocities that can be observed in he IH tube (2.7 m/s vs 2.1 m/s): this higher velocity lead to a higher friction factor and so higher pressure losses. In general friction factor ratio tends to increase with the rise of Reynolds number for all cases and the use of a turbulence leads to a considerable increase of friction factor in comparison with the use of a smooth pipe. The Thermal Enhancement Factor can be introduced to summarize the results and to weight the two main phenomena [40, 41, 42, 43]:

- The increase of the heat transfer coefficient due to the turbulence promoters;
- The increase of pressure drop (for the same reason) which determines a higher pumping cost.

The TEF is defined as follows :

$$TEF = \frac{Nu/Nu_s}{(f/f_s)^{1/3}}, \tag{4.24}$$

where Nu and Nu_s have been evaluated through CFD and Sieder-Tate correlation and

$$f = \frac{2}{L/D}\frac{\Delta p}{\rho u_m^2}, \tag{4.25}$$

$$f_s = 0.184 Re_D^{-0.2}, \tag{4.26}$$

that is the McAdams correlation valid for turbulent flows in conditions good for the current case. The TEF tends to decrease as the Re number increase, as then the friction factor becomes more and more significant. By the way, in the current work, it has been evaluated just for one Re number and it has been observed a TEF 20 $\%$ higher in the case of the IH tube: now it is possible to conclude that the choice of turbulence promoters is well justified by its increasing thermal performances.

4.4 AISI 316 Helices (AH) receiver

The AISI 316 tube equipped with helical ribs (AH) has the very same geometry of the IH tube. So, as the two CADs are equal, it makes easier to perform the CFD analysis of this third sample: in fact, the numerical model changes just in the definition of the material physical properties. In particular, as it can be used the very same mesh, the grid independence study has not to be checked anymore.
The calibration has been performed on test AH2 and the resulting distributions of emissivity and absorptivity are shown in Figure 4.56 and Figure 4.57, respectively.

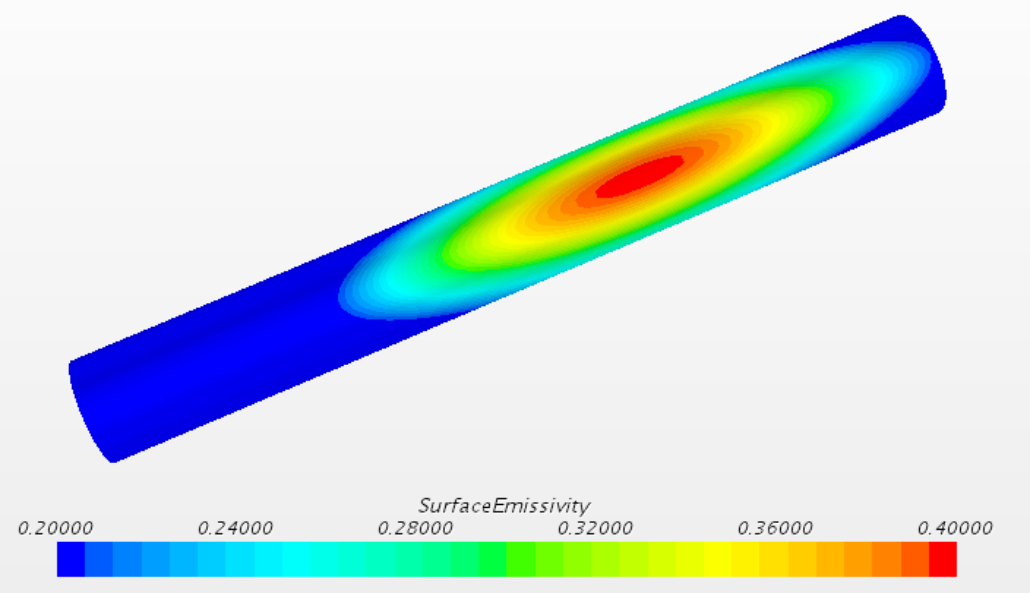

Figure 4.56: Emissivity calibrated on test AH2, irradiated side.

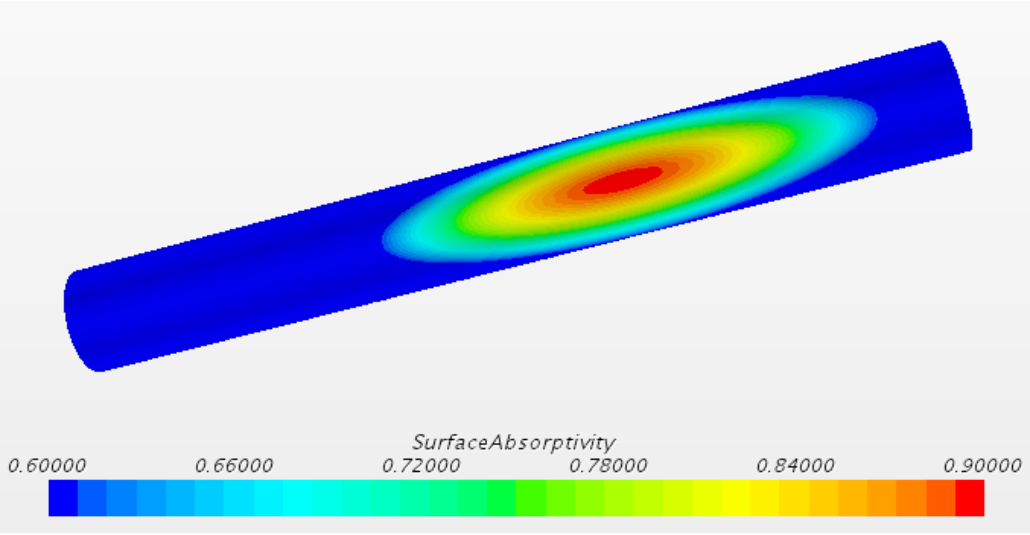

Figure 4.57: Absorptivity calibrated on test AH2, irradiated side.

The comparison between experimental and numerical results are shown below, in Figure 4.58.

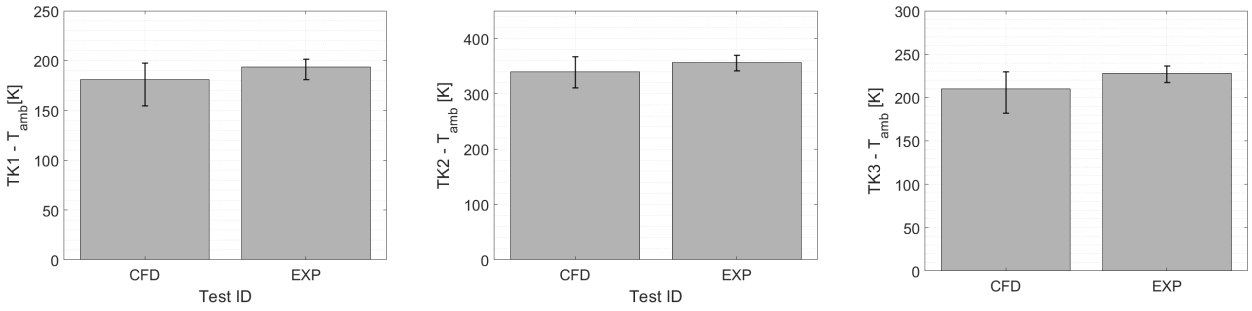

Figure 4.58: Calibration results on test AH2: wall temperatures.

The CFD analysis of the AH tube has been carried out as in the Sections 4.2 and 4.3. By the way, the results won't be presented as this analysis appears to be inconsistent and not so interesting for the present work, for the following reasons:

- The AISI 316 tube equipped with helical turbulence promoters is worse than all the other configurations. As no good preliminary results have been observed from the collected data, no better results will be expected from the CFD analysis;
- The AH sample was tested just for couple of hours and no many tests have been selected. It means that it would be difficult to perform a characterization of the material, as done for the IS tube in Section 4.2.6;
- As no references in literature has been found about emissivity and absorptivity of AISI 316, the calibration of the two parameters appears to be very arbitrary and inconsistent.

5. Conclusions and Perspectives

This work presents an experimental campaign where four air-cooled absorber tube configurations have been tested at the PSA SF60, with the aim of evaluating their thermal behavior under realistic conditions (one-sided heating) and providing data to calibrate and validate the numerical CFD models of the tubes tested. The use of turbulence promoters has been experimentally demonstrated to reduce the wall temperature with respect to the case of a smooth tube, as expected.
Two different complex CFD models have been developed for the smooth tube and for the helically ribbed configurations (IH and AH) and both have been validated against the experimental results: the numerical and experimental results are in good agreement. The temperature maps of the solid and fluid regions have been presented to show the differences between two of the four designs (IS and IH). Some additional analysis have been carried out to demonstrate the better thermal efficiency of the IH tube: the Sieder-Tate correlation has been used to extrapolate a correction factor for the design of the helices with respect to a smooth tube and also to evaluate the TEF. The results justify the choice of turbulence promoters.
The numerical analysis will be extended to the remaining tube configuration, the tube equipped with annular rings. In addition, it would be interesting to carry out an optimization of the geometric parameters of the helices, to maximize the increasing efficiency with respect to the smooth configuration.
In perspective, the validated CFD models will become useful tools to optimize the geometry with the aim of reducing the thermal gradients on the tube wall and increasing the life time of the component against thermal fatigue. This analysis will require a detailed and dedicated work.

References

[1] COP21. Adoption of the paris agreement, 2015.

[2] Generaldirektion Energie und Verkehr Europäische Kommission and Generaldirektion Forschung Europäische Kommission. *Concentrating solar power: from research to implementation*. Office for Official Publications of the Europ. Communities, 2007.

[3] IEA. World energy outlook 2018. *International Energy Agency*, 2018.

[4] M Günther, N Janotte, A Mezrhab, K Pottler, C Schillings, S Wilbert, and F Wolferstätter. Advanced csp teaching materials chapter 1 introduction. *Advanced CSP Teaching Materials Enermena*, 2011.

[5] JF Servert, Eduardo Cerrajero, D López, S Yagüe, F Gutierrez, M Lasheras, and G San Miguel. Base case analysis of a hysol power plant. *Energy Procedia*, 69:1152–1159, 2015.

[6] Md Tasbirul Islam, Nazmul Huda, AB Abdullah, and R Saidur. A comprehensive review of state-of-the-art concentrating solar power (csp) technologies: current status and research trends. *Renewable and Sustainable Energy Reviews*, 91:987–1018, 2018.

[7] David Barlev, Ruxandra Vidu, and Pieter Stroeve. Innovation in concentrated solar power. *Solar Energy Materials and Solar Cells*, 95(10):2703–2725, 2011.

[8] Najla El Gharbi, Halima Derbal, Sofiane Bouaichaoui, and Noureddine Said. A comparative study between parabolic trough collector and linear fresnel reflector technologies. *Energy Procedia*, 6:565–572, 2011.

[9] Tomislav M Pavlović, Ivana S Radonjić, Dragana D Milosavljević, and Lana S Pantić. A review of concentrating solar power plants in the world and their potential use in serbia. *Renewable and Sustainable Energy Reviews*, 16(6):3891–3902, 2012.

[10] Amita Ummadisingu and MS Soni. Concentrating solar power–technology, potential and policy in india. *Renewable and sustainable energy reviews*, 15(9):5169–5175, 2011.

[11] First Green. Comparison of csp technologies. 2012.

[12] Sarada Kuravi, Jamie Trahan, D Yogi Goswami, Muhammad M Rahman, and Elias K Stefanakos. Thermal energy storage technologies and systems for concentrating solar power plants. *Progress in Energy and Combustion Science*, 39(4):285–319, 2013.

[13] Ming Liu, NH Steven Tay, Stuart Bell, Martin Belusko, Rhys Jacob, Geoffrey Will, Wasim Saman, and Frank Bruno. Review on concentrating solar power plants and new developments in high temperature thermal energy storage technologies. *Renewable and Sustainable Energy Reviews*, 53:1411–1432, 2016.

[14] Franz Trieb, Christoph Schillings, Marlene O'sullivan, Thomas Pregger, and Carsten Hoyer-Klick. Global potential of concentrating solar power. In *SolarPACES Conference*, pages 15–18, 2009.

[15] REN21, 2019.

[16] Lifeng Li, Joe Coventry, Roman Bader, John Pye, and Wojciech Lipiński. Optics of solar central receiver systems: a review. *Optics express*, 24(14):A985–A1007, 2016.

[17] Clifford K Ho and Brian D Iverson. Review of high-temperature central receiver designs for concentrating solar power. *Renewable and Sustainable Energy Reviews*, 29:835–846, 2014.

[18] Manfred Becker and M Böhmer. *Gast: The Gas Cooled Solar Tower Technology Program: Proceedings of the Final Presentation May 30-31, Lahnstein, Federal Republic of Germany*. Springer Verlag, 1989.

[19] DLR. Solhyco final public report - ses6-ct-2005-019830. 2011.

[20] M Quero, R Korzynietz, M Ebert, AA Jiménez, A Del Río, and JA Brioso. Solugas–operation experience of the first solar hybrid gas turbine system at mw scale. *Energy Procedia*, 49:1820–1830, 2014.

[21] Psa website, http://www.psa.es/es/index.php.

[22] Diego Martínez-Plaza. General information plataforma solar de almerÍa.

[23] MI Roldán and R Monterreal. Heat flux and temperature prediction on a volumetric receiver installed in a solar furnace. *Applied energy*, 120:65–74, 2014.

[24] J Ballestrın, S Ulmer, A Morales, A Barnes, LW Langley, and M Rodrıguez. Systematic error in the measurement of very high solar irradiance. *Solar energy materials and solar cells*, 80(3):375–381, 2003.

[25] Omega. Thermocouples probes.

[26] DOLSAT Consult. Principiile senzorilor de temperatură, 2019.

[27] R Osuna, R Morillo, JM Jiménez, and V Fernández-Quero. Control and operation strategies in ps10 solar plant. *Proceedings 13th Solar PACES, Sevilla, Spain, Jun*, pages 20–23, 2006.

[28] J Ballestrín, M Casanova, R Monterreal, J Fernández-Reche, E Setien, J Rodríguez, J Galindo, FJ Barbero, and FJ Batlles. Simplifying the measurement of high solar irradiance on receivers. application to solar tower plants. *Renewable energy*, 138:551–561, 2019.

[29] Federica Tarasco. Numerical evaluation of thermal fatigue lifetime of air-cooled tubular receivers for csp plants. 2016.

[30] Bronkhorst high tech. Datasheet f-203av. mass flow controller for gases.

[31] GA GREENE. Dependence of total hemispherical emissivity of inconel-718 on surface oxidation and temperature. Technical report, Brookhaven National Lab., Upton, NY (US), 1999.

[32] Frank Incropera and David DeWitt. Introduction to heat transfer. 1985.

[33] W Malalasekera and HK Versteeg. An introduction to computational fluid dynamics. *The finite volume method, Harlow: Prentice Hall*, page 1995, 2007.

[34] S CD-adapco. *STAR CCM+ User Guide Version 13.02*, 2018.

[35] O. Mohammadi B., Pironneau. *Analysis of the k-esp turbulence model*. Wiley, 1994.

[36] E Abbasi-Shavazi, GO Hughes, and JD Pye. Investigation of heat loss from a solar cavity receiver. *Energy Procedia*, 69:269–278, 2015.

[37] Ishmail B Celik, Urmila Ghia, Patrick J Roache, and Christopher J Freitas. Procedure for estimation and reporting of uncertainty due to discretization in cfd applications. *Journal of fluids Engineering-Transactions of the ASME*, 130(7), 2008.

[38] Donald F Young, Bruce R Munson, Theodore H Okiishi, and Wade W Huebsch. *A brief introduction to fluid mechanics*. John Wiley & Sons, 2010.

[39] R Zanino, R Bonifetto, F Cau, A Portone, and L Savoldi Richard. Cfd analysis of the iter first wall 06 panel. part ii: Thermal-hydraulics. *Fusion Engineering and Design*, 89(4):431–441, 2014.

[40] Khwanchit Wongcharee, Wayo Changcharoen, and Smith Eiamsa-ard. Numerical investigation of flow friction and heat transfer in a channel with various shaped ribs mounted on two opposite ribbed walls. *International Journal of Chemical Reactor Engineering*, 9(1), 2011.

[41] Oronzio Manca, Sergio Nardini, and Daniele Ricci. Numerical analysis of water forced convection in channels with differently shaped transverse ribs. *Journal of Applied Mathematics*, 2011, 2011.

[42] Mi-Ae Moon, Min-Jung Park, and Kwang-Yong Kim. Evaluation of heat transfer performances of various rib shapes. *International Journal of Heat and Mass Transfer*, 71:275–284, 2014.

[43] Pongjet Promvonge and Chinaruk Thianpong. Thermal performance assessment of turbulent channel flows over different shaped ribs. *International Communications in Heat and Mass Transfer*, 35(10):1327–1334, 2008.